Molecular Dynamics Studies of ZrO2 and CeO2 based Solid Oxide Fuel Cell (SOFC) Materials

by

Sudeshna Madhual

Roll No. 186121028

A thesis submitted

in Partial Fulfillment of the Requirements

for the Degree of

Doctor of Philosophy.

Department of Physics

Indian Institute of Technology Guwahati

Guwahati 781039, India

Certificate

This is to certify that the thesis entitled "**Molecular Dynamics Studies of ZrO2 and CeO2 based Solid Oxide Fuel Cell (SOFC) Materials**", submitted by Sudeshna Madhual (186121028), a research scholar in the *Department of Physics*, *Indian Institute of Technology Guwahati*, for the award of the degree of PhD, is a record of an original research work carried out by her under my supervision and guidance. The thesis has fulfilled all requirements as per the regulations of the institute and in my opinion has reached the standard needed for submission. The results embodied in this thesis have not been submitted to any other University or Institute for the award of any degree or diploma.

Signed:

Supervisor: Prof. Padma Kumar Padmanabhan
Department of Physics,
Indian Institute of Technology Guwahati,
Guwahati-781039, Assam, India.

Date:

Acknowledgement

I want to convey my heartfelt gratitude to Prof. Padma Kumar Padmanabhan, my Ph.D. advisor, for unwavering support, patience, and motivation throughout my doctoral journey. His profound knowledge of the field has enhanced my understanding, and his unwavering belief in my capabilities has been a constant source of inspiration, encouraging me to strive diligently. I extend my gratitude to the members of my doctoral committee: Prof. Subhradip Ghosh, Prof. U. N. Maity, and Prof. Aditya Narayan Panda, for their valuable comments, encouragement, and thought-provoking questions. Their insights have prompted me to delve deeper into the conceptual background of my research.

I would like to express my sincere appreciation to Prof. S. Ghosh and Prof. A. Perumal, the former and current Heads of the Department of Physics, for facilitating the resources essential for my research. My heartfelt gratitude extends to all the faculty members of the department who offered various forms of support during my tenure. Special thanks also go to the technical staff, support personnel, and office members whose assistance was invaluable. Their collective support was crucial in enabling the successful execution of my research. I extend my gratitude to the Center for Advanced Computing (CDAC) Pune, Param Ishan IIT Guwahati, and particularly the Newton Cluster of the Department of Physics, IIT Guwahati, for generously providing the necessary CPU hours to conduct the research presented in this thesis.

I want to convey my gratefulness to Krishnanjan bhai, with whom I have not only collaborated extensively and gained valuable insights but also received consistent support to navigate through every situation during my Ph.D. journey. I extend my gratitude to my seniors Kartik bhai and Sangkha bhai, whose valuable suggestions significantly enriched my work. A special acknowledgment goes to my lab-mates, Sunil, Sanjib, Likun, and Pujarini; teaming with you throughout these Ph.D. years has been truly memorable. Your support, both personally and in research, has been truly impactful.

I want to express my heartfelt thanks to my entire family, including my parents, brother, and uncles, for their tireless support. Their trust in me has been a constant source of motivation, propelling me forward.

I express my heartfelt gratitude to my best companions, Soubhagya Laxmi, Dharashree, and the friend cum elder sister, Swarupa Subhadarshini, for their unwavering support and encouragement throughout my Ph.D. journey, from its inception to its completion. It is thanks to their steadfast support that I have been able to successfully navigate both my professional and personal life with equilibrium. I appreciate the wonderful companionship of my 2018-batchmates. A special thanks goes to Tadasha for her immense care and support. Lastly, I would like to thank Mrinal, for always being there for me and for his unwavering patience, support, and encouragement.

Abstract

Solid oxide fuel cells (SOFCs) are a class of portable primary energy devices, that stand the potential as a green and sustainable alternative to fossil fuels. However, widespread commercial adoption of these electrochemical devices demands significant advancements in their design and efficiency as well as the development of infrastructural ecosystem. The electrolyte, that is sandwiched between the electrodes, is a crucial component of an SOFC device, having a critical impact on its performance. For the efficiency, operational safety, and lifespan of SOFC devices, the electrolyte material has to meet several criteria, such as high ionic conductivity, high chemical and mechanical stability, compatibility with potential electrodes, etc. As argued in the Introduction of this thesis, zirconia (ZrO_2) and ceria (CeO_2) based ceramic solids are among the most promising choices for practical applications, though their commercial viability demands further improvements. A thorough understanding of the microscopic nature of ion transport and the factors governing it is crucial to the necessary advancement of SOFC devices.

The thesis attempts to bring out fresh insights into the microscopic mechanism of ion transport in yttria doped ceria and zirconia employing molecular dynamics (MD) simulations. The theoretical foundations and computational algorithms of MD simulations are discussed in Chapter 2 of the thesis. Chapter 3 of the thesis discusses the nature of oxide ion transport in yttria-doped ceria, in terms of the microscopic energy barriers, local environments and residence times of oxygen ions at their tetrahedral sites, and other pertinent details. Chapter 4 explores oxide ion migration in yttria- stabilized zirconia (YSZ) with a focus on the energetic aspects of different pathways linking oxygen sites as well as of the saddle points due to the specific cationic edges. The study suggests a significant degree of oxide ion correlations in YSZ matrix. In Chapter 5, the impact of cationic distribution (Zr^{4+}/Y^{3+}) on oxide ion transport in the YSZ matrix is examined. The study finds that certain cationic ordering can enhance the ionic conductivity up to four orders of magnitude relative to the randomly ordered structures. The findings of the studies are summarized in Chapter 6, along with a glimpse at possible future directions.

Contents

Chapter 1

Introduction

The world's reliance on fossil fuels to meet its energy demands has created a plethora of challenges, including climate change and escalating global warming. One prominent example of this was the extensive use of coal in industry during the 19th century, which resulted in soil degradation, greenhouse gas emissions, and the contamination of air and water resources. The utilization of fossil fuels including coal, petroleum, and natural gas not only leads to severe ecological implications but also poses social and economic challenges such as improper land utilization, displacement of indigenous communities, and reliance on limited resources for economic growth [1–4]. In its 2001 Third Assessment Report, the Intergovernmental Panel on Climate Change (IPCC) affirmed that the indisputable warming of the planet was primarily driven by human activity, specifically the combustion of fossil fuels. In light of the alarming statistics regarding accidents and fatalities in the energy sector, it has become evident that relying on fossil fuels for energy production poses significant risks to human safety [5].

In recent times, there has been a growing emphasis on programs aimed at promoting the use of renewable energy, and ultimately eliminating the use of fossil fuels. Here are some examples of programs that promote clean energy and sustainable transportation across the globe: the Energiewende policy in Germany, the Clean Energy Programs in the US which include initiatives such as the Investment Tax Credit (ITC) and the Production Tax Credit (PTC), China's Green Energy Initiatives, India's National Solar Mission, Norway's promotion of electric vehicles, France's focus on sustainable transportation, and Australia's Renewable Energy Target. India is encouraging the use of electric vehicles and other clean energy technologies with the aim of reaching 450 gigawatts of renewable energy capacity by 2030 [6–12]. The primary objective of these programs is to increase the adop-

tion of renewable energy sources, create cleaner methods for generating hydrogen energy, produce sustainable materials for batteries and fuel cells, and promote the development and implementation of hybrid systems. Fuel cells and batteries are considered as the most important portable green energy devices as they provide a safe and efficient alternative for converting energy from various sources into electrical power [13–20].

Fuel cells play a vital part in the shift to renewable energy sources by providing a clean and efficient energy solution for transportation, stationary power generation, and backup power [15, 21–23]. Batteries have been the go-to energy storage technology for a while now. However, they are not a primary source of energy, and suffer from certain limitations such as limited storage capacity and a short lifespan. Due to the need for more efficient and eco-friendly energy sources, fuel cells are being considered as a suitable replacement for batteries in various applications [24–27]. In the transportation sector, fuel-cell cars are being researched and developed as an alternative to battery-electric vehicles. Fuel cell cars are better suited for heavy-duty and long-distance driving applications as they offer longer driving ranges and faster refueling periods. Fuel cells are also being used in stationary power applications to produce energy from renewable sources like bio-gas and hydrogen while also serving as a standby power source for vital infrastructure. Moreover, fuel cell devices are also being employed in rural areas that lack access to conventional power sources. Although the transition to fuel cells from traditional energy sources is still in its early stages, it has enormous potential for the future when energy is generated more sustainably and effectively [21, 28–33]. The data acquired from multiple sources depict the estimated financial investments that various government agencies and private sectors are expected to make towards the development of sustainable eco-system of fuel cell technology in the coming years through various programs [34–38].

Sir William Grove, who proposed the concept of a fuel cell in 1839, is widely regarded as its inventor. In the 1930s, Francis Bacon created the first ceramic electrolyte-based solid oxide fuel cell. In the 1950s, General Electric developed the first functional fuel cell to be used in spacecraft. In the 1970s and 1980s, fuel cell technology was further developed and commercialized for use in stationary power applications, including backup power for buildings. Since the 1990s, many major automakers started developing fuel cell prototypes to be used in vehicles [39, 40]. Fuel cell efficiency and cost reduction were greatly improved during the 2000s and 2010s. Advances in materials science and engineering led to the development of new and more effective and reliable fuel cell designs, such as proton exchange membrane

fuel cells and solid oxide fuel cells [41, 42]. In recent years, fuel cells have been used for backup power for data centers, fuel cell automobiles, and stationary power for homes and companies. Government incentives and the emergence of new markets, increase in hydrogen fuelling infrastructure, etc., are encouraging the advancement of fuel cell technology [43–46].

1.1 Fuel Cells

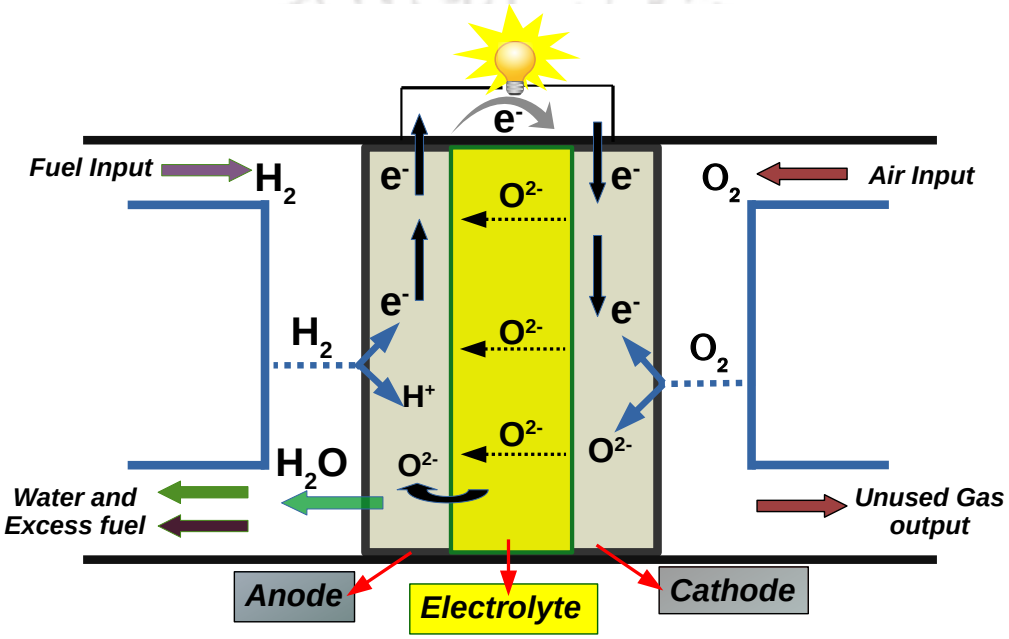

Figure 1.1: Schematic diagram demonstrating the functioning of a fuel cell.

Fuel cells are strategically engineered with several components that function as a unit to efficiently convert the chemical energy of the fuel into electrical power. The fuel cell is composed mainly of three components: the anode, cathode, and electrolyte [39, 47, 48]. The anode, which is typically made of a porous material coated with platinum or other catalysts, is the negative electrode of the fuel cell. Its primary function is to break down the fuel molecules into protons and electrons, allowing electrons to flow through the circuit and protons to combine with oxygen ions from the electrolyte. This process produces water or other byproducts. On the other hand, the cathode, made of a porous material coated with a catalyst (often a combination of platinum and other metals), facilitates the reaction between electrons and oxygen from the air to produce oxygen ions. The electrolyte is ideally a superionic conductor, that acts as an insulator for electronic current. Gas diffusion

layers enable fuel and air to reach the anode and cathode, respectively, and remove waste products such as heat and water. Finally, bipolar plates transfer reactant gases to the anode and cathode, providing electrical contact between the fuel cell stack cells [40, 49–51]. The operating concept of a fuel cell is straightforward which is depicted in Figure 1.1. Hydrogen, the 'simplest' of fuels, is oxidized at the anode releasing its electrons, which generate electrical current in the external circuit. Being an oxidant, oxygen at the cathode accepts these electrons from the external circuit and gets reduced. The electrolyte conducts ionic species between the cathode and anode, completing the process. The byproducts of the process are of significantly lower carbon footprint.

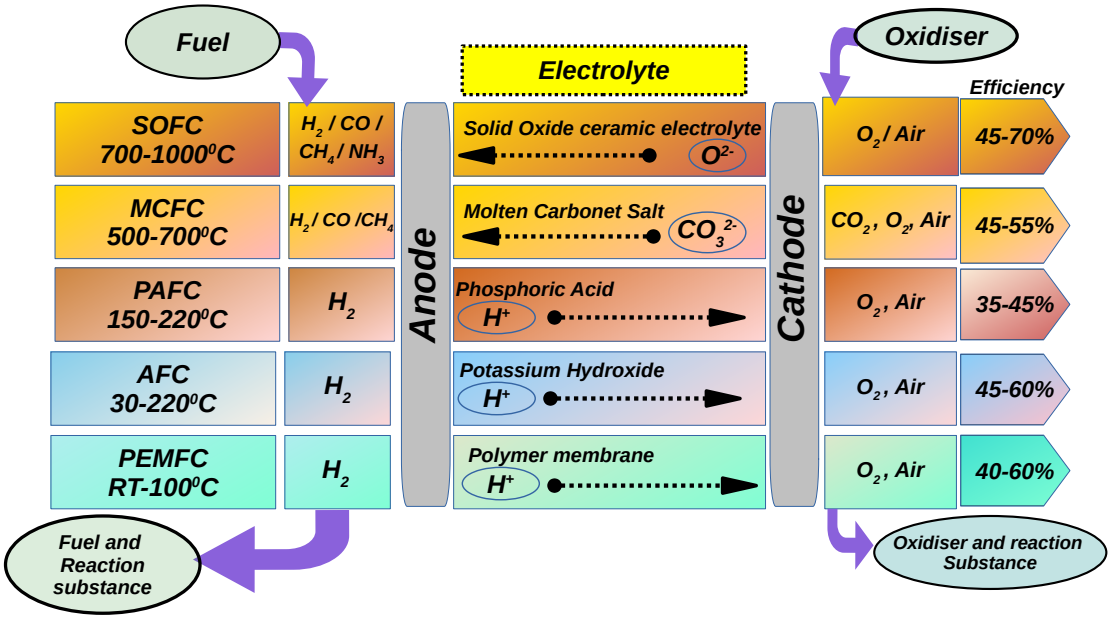

Figure 1.2: Summary of the various types of fuel cells, including the electrolyte used and operating temperatures.

There are five main types of fuel cells, each named after the nature of the electrolyte material. These are alkaline fuel cells (AFC), polymer exchange membrane fuel cells (PEMFC), phosphoric acid fuel cells (PAFC), molten carbonate fuel cells (MCFC), and solid oxide fuel cells (SOFC). PEMFCs, for instance, use a solid polymer electrolyte membrane that allows positively charged hydrogen ions (protons) to pass through while restricting negatively charged electrons from doing so. PAFCs, on the other hand, use phosphoric acid as their electrolyte. MCFCs use an electrolyte made of molten carbonate salt, while AFCs use an alkaline electrolyte such as potassium hydroxide. SOFCs typically employ ceramic solids as the electrolyte. Each fuel cell has different requirements concerning its operating temperature, elec-

Fuel Cell	Electrolyte Type	Fuel	Operating Temp (^{0}C)	Efficiency(%)
PEMFC	Polymer	Pure H_2	60-130	40-60
AFC	KOH	Pure H_2	60-220	45-60
PAFC	H^+	H_2	150-220	35-45
MCFC	Li_2CO_3 + K_2CO_3	H_2, CO, CH_4	650	45-55
SOFC	$ZrO_2 + Y_2O_3$	H_2, CO, CH_4, NH_3	700-1000	45-70

Table 1.1: Classification of fuel cell systems based on the type of electrolyte, fuel used, operating temperature, and electrical efficiency.

trical efficiency, fuel composition, and the type of electrolyte used [22, 52–54]. Fuel cells are again classified based on their operating temperature: low-temperature fuel cells (LTFCs), intermediate-temperature fuel cells (ITFCs), and high-temperature fuel cells (HTFCs) [55].

Low-temperature fuel cells (LTFCs) are ideal for low-power applications since they operate at temperatures under $100°C$. Examples of LTFCs include AFCs and PEMFCs. AFCs are used for specialized applications like spacecraft and submarines, and operate at relatively low temperatures of 70 to $100°C$. PEMFCs are appropriate for low-temperature applications such as automobiles and compact portable electronics [56, 57]. Intermediate-temperature fuel cells are best suited for medium-power applications, with their operating range between $100°C$ and $500°C$. PAFCs are a type of ITFC that operate at temperatures between $150°C$ and $250°C$, which is higher than PEMFCs [58, 59]. They are commonly used in medium-scale applications, such as combined heat and power systems in buildings. High-temperature fuel cells, on the other hand, are more suitable for high-power applications as they can operate at temperatures above $500°C$. There are two types of HTFCs: MCFCs and SOFCs. MCFCs are used in large-scale applications, such as power plants, and usually operate at temperatures around $600°C$, while SOFCs typically operate between 800 to $1000°C$ and are used to power ships and industries [60–63].

The operating temperature of fuel cells can affect their effectiveness, affordability, and durability. Higher-temperature fuel cells are generally more efficient and cost-effective but require more substantial materials and advanced thermal management systems. Lower-temperature fuel cells can have simpler designs and be more flexible, but they are generally more expensive and less efficient. Table 1.1 and figure 1.2 provide the summary of the scenario.

1.2 Solid Oxide Fuel cells (SOFC)

Solid oxide fuel cells (SOFCs) are considered one of the most advantageous types of fuel cells for various reasons. They outperform most other fuel cell types in terms of efficiency, reaching up to 70%. They can operate on various fuels, including hydrogen, hydrocarbons, carbon monoxide, and others, making them fuel-flexible and suitable for a wide range of applications. The solid-state design of SOFCs also contributes to their durability. Moreover, they can generate power more efficiently due to their high operating temperatures, and with lower emission levels [64–69]. Despite their many benefits, SOFCs have some drawbacks, such as high operational temperatures, delayed starts, high costs, and intolerance to sulfur content [70, 71].

Gaugain [43, 72] discovered solid electrolytes in 1853, which ultimately led to the development of SOFCs. Nernst [43, 73] demonstrated that 15 mol% Yttria (Y_2O_3) doped with Zirconia (ZrO_2) exhibits strong conductivity at extreme temperatures, which makes it a suitable material for use as a burning filament in lamps. In 1935, Schottky [43] proposed that YSZ could serve as a promising choice for a solid electrolyte. Wagner [74] subsequently revealed that oxide-solid solutions could facilitate ion conduction through oxygen vacancies induced by acceptor doping in the host lattice. Afterward, Baur and Presis [74] demonstrated the application of YSZ in solid ceramic oxide fuel cells functioning at a temperature of 1000°C. In the 1960s and 1970s, several patents were filed for using thin layers of solid ceramic oxides as electrolyte material and designing single SOFCs with planar and tubular designs to boost performance [65, 75, 76]. NASA launched SOFC research in the 1960s for space applications. SOFCs were used for stationary power generation in the 1970s [63, 77]. However, their high operating temperatures, expensive materials, and slow startup rendered commercialization challenging. In the 1980s and 1990s, studies focused on reducing the operating temperatures of SOFCs and using less expensive materials. Since the early 2000s, the efficiency and cost-effectiveness of SOFC technology have increased steadily due to recent developments in material science and engineering [67, 78, 79].

SOFCs can further be classified into different types based on the current carrier (mobile ion) of the electrolyte. Thus there are predominantly, O-SOFC where the electrolyte is O^{2-} conducting [80–82] and H-SOFC which employs protonic (H^+) conductors [83–85]. Each type of SOFC has its own strengths and weaknesses, depending on the specific application. For instance, O-SOFCs operate at high temperatures and have a high power density, but they require careful thermal management

and are prone to material degradation. On the other hand, H-SOFCs have a lower operating temperature range and modest efficiency, but they have a lower power density and require high purity of the fuel. Out of all the SOFC types, O-SOFCs have received better scientific attention due to their high power production and stability.

For the rest of the discussions, we shall restrict to O-SOFCs for their immediate relevance in the context of the present thesis, which deals with the investigation of oxide ion conducting electrolytes. For the sake of completeness, we shall briefly review typical solids that find applications as anode and cathode materials in SOFCs, before moving on to oxide ion conducting electrolytes. Detailed discussions on materials for the different cell components, their synthesis, characterization and performance analysis may be found elsewhere [86–91].

1.3 SOFC Materials

1.3.1 Anode materials

Anodes are critical components of SOFCs as they facilitate the electrochemical reaction of fuel, typically hydrogen or a hydrocarbon, at the interface. At the anode, interfaces called triple-phase boundaries (TPBs) (exist between the electrode, electrolyte, and gas) enable the preferential electrochemical oxidation of fuels. For the complete oxidation of fuel, anode materials must satisfy several requirements. They need to have strong electronic conductivity and sufficient electrocatalytic activity. In addition, they must have adequate mechanical strength to withstand weight and mechanical pressure, good chemical and thermal stability, and minimal thermal expansion mismatch with other adjacent cell components. Moreover, an ideal anode material should be able to tolerate carbon deposition, sulfur poisoning, and reoxidation. It should also be able to handle the fuel flexibility and not be reactive to commonly used fuel gases, such as hydrogen, CO, natural gas, and other hydrocarbons.

Traditionally, metals like graphite, platinum, iron, cobalt, and nickel have been used as catalysts in both cathode and anode. For several years, nickel has been used in anodes of SOFC, because of its low cost, exceptional chemical stability, and excellent catalytic activity for hydrogen oxidation and hydrocarbon fuel reforming. The search for potential anode materials has led to the intensive study and development of various materials, such as perovskite-structured anodes, ceramic composites, py-

Anode	Fuel	Ref.
Ni-Cu-YSZ	CH_4	[103]
Ni-Co-YSZ	CH_4	[104]
Ni-Sn-YSZ	Biogas	[105, 106]
Ni-Ag-YSZ	CH_4	[107, 108]
Co-Cu/Fe-MgO/CeO2-YSZ	CH_4	[109, 110]

Table 1.2: Metal-YSZ ceramic materials developed as anodes for SOFCs.

rochlores, and fluorite-structured anodes [92–96]. The most widely used material for anodes in SOFCs is nickel-yttria stabilized zirconia (Ni-YSZ), which has a fluorite crystal structure. This substance has high electrical conductivity, good electrolyte compatibility, and high catalytic activity towards fuel oxidation. The YSZ phase provides excellent ionic conductivity for transferring ions from the anode to the electrolyte. This, coupled with the high catalytic activity of Ni-YSZ, leads to improved fuel utilization and lower operating temperatures [97–99]. Moreover, the YSZ phase of the anode material is stable in the presence of the YSZ electrolyte, which prevents the creation of a separate interfacial layer between the anode and the electrolyte. Table 1.2 illustrates some of the metal-based YSZ anodes used in SOFCs. However, Ni-YSZ is prone to coking and sulfur poisoning, which can eventually hinder its performance [98, 100–102].

To address the aforementioned issues, researchers have developed Nickel-gadolinium-doped ceria (Ni-GDC). Compared to Ni-YSZ, Ni-GDC has higher catalytic activity towards fuel oxidation and is less prone to coking. However, it is more expensive and has poorer electrolyte compatibility. It is worth noting that the electronic conductivity of this material is higher than that of Ni-YSZ. Furthermore, the addition of acceptor dopant oxides such as CaO, Y_2O_3, Gd_2O_3, and Sm_2O_3 can be employed to modify their ionic conductivity. Recent studies have shown that Ni-GDC degrades significantly less in current density performance for hydrogen oxidation in H_2S containing H_2 fuel than Ni-YSZ.

Besides the materials mentioned above, Cu-CeO_2 and Co-CeO_2-based anode materials exhibit strong catalytic activity for oxidizing hydrocarbon fuels such as methane and propane used in SOFCs. The strong conductivity of Cu-CeO_2 facilitates the easy flow of electrons from the anode to the external circuit. However, Cu-CeO_2/Co-CeO_2 is less stable at high temperatures. Carbon deposition on Cu/Co-CeO_2 also reduces its catalytic activity. Table 1.3 lists some of the ceria-

Anode	Fuel	ref.
Ni-Co-GDC	CH4	[111, 112]
Ni-Fe-GDC	CH4	[109]
Rh-SDC	CH4	[113]
Au/Cu-SDC	n-butane	[114]
Cu-ZDC	CH4	[115]

Table 1.3: Metal-CeO_2 based ceramic materials developed as anodes for SOFCs.

based anodes currently under focus.

Efforts have been made to develop sulfur-tolerant anode materials that do not rely on nickel-fluorite-based structures. Some of these materials are nickel-free conductive metal oxide-based perovskites (ABO_3), which include Y-doped $SrTiO_3$, $La_{1-x}Sr_xVO_3$ (LSV; $x = 0.5$), $Sr_{1-x}La_xTiO_3$ (LST; $x = 0.3$–0.4), $Ce_{0.9}Sr_{0.1}VO_x$ ($x = 3$) and its doped variations, $La_{1-x}Sr_xCr_{1-y}Mn_yO_3$ (LSCM; $x = 0.25$, $y = 0.5$), double perovskite structured materials such as $Sr_2Mg_{2-x}MoO_6$ (SMMO; $x = 1$), $Sr_2Fe_{4/3}Mo_{2/3}O_6$, and pyrochlore structured $Gd_2Ti_{2-x}Mo_xO_7$ ($x = 0.6$). It has been observed that all of the anode materials exhibit excellent compatibility with YSZ electrolytes. These conductive oxides have better sulfur tolerance than Ni-fluorite structured oxide, but their poorer electrical conductivity makes them less effective as anodes [116, 117, 117–123]. Although perovskite anodes exhibit good oxide ion conductivity, the stability of perovskites tends to decrease as their oxide ion conductivity and oxygen permeability increase. Thus scientists are now developing composite of perovskite and fluorite-structured (e.g., $La_xSr_{1-x}TiO_{3-d}/Ce_{1-y}Gd_yO_{2-\delta}$) anode materials for SOFC applications [124–127].

Strontium-doped ceramics, such as $LaSrFeO_3$ (LSF) and its variants, are perovskite-structured anode materials for SOFCs. They exhibit unique characteristics, such as high catalytic activity for fuel oxidation (e.g., hydrogen and carbon monoxide). It also works well with YSZ electrolytes and is stable at high temperatures, enhancing the durability of SOFCs [128–130]. However, $LaSrCoO_3$ (LSC) and LSF have poorer electrical conductivity, which can slow electron transport from the anode to the external circuit. Additionally, reactions with cathode materials can degrade LSC and LSF at the cathode-anode interface, reducing their catalytic activity and SOFC performance [131–137]. However, in order to make them commercially viable, the catalytic activity for fuel oxidation of these materials need be enhanced.

1.3.2 Cathode Materials

The cathode of an SOFC assumes a crucial function in the electrochemical reduction of oxygen. For efficiency, the cathode needs to possess several essential characteristics, such as thermal and chemical compatibility with the electrolyte, high catalytic activity for the oxygen reduction reaction (ORR), etc. Further, the cathode must exhibit sufficient porosity to facilitate the easy diffusion of gaseous oxygen to the cathode/electrolyte interface. The cathode material must also demonstrate stability in oxidizing atmospheres during the cell operations [69, 138–140]. Oxygen anions generated on the surface of the cathode during the oxygen reduction reaction need to diffuse through the bulk of the cathode material to reach the electrolyte. Consequently, the cathode material needs to exhibit both electrical and ionic conductivity.

In SOFCs, cathode materials such as $La_{1-x}Sr_xMnO_3$ (LSM) and $La_{1-x}Co_xMnO_3$ (LSC) have been widely explored. LSM, in particular, has been extensively studied due to its effective performance at elevated temperatures (around $1000°C$). This is attributed to the substitution of Sr^{2+} for the La^{3+} site, resulting in high oxygen ion vacancies and serving as an efficient ionic conductor. The introduction of Sr^{2+} induces charge compensation in LSM, leading to a transition of Mn from Mn^{3+} to Mn^{4+} and an associated increase in electronic conductivity. However, despite these electronic conductivity enhancements, LSM exhibits low ionic conductivity (approximately 10^{-7} S/cm at low temperatures) due to the charge compensation of Mn in the absence of oxygen vacancies [141–144]. To enhance the functionality of dense or porous LSM films on YSZ electrolytes, it is necessary to employ a two-layer cathode consisting of a porous layer on one side and a dense YSZ film on the other.

In order to enhance the performance and prevent issues with the production of the insulating phases at the LSM/YSZ interface, various authors have looked at different rare-earths in the lanthanide position, such as Nd, Pr or Sm [145–150]. In terms of thermal expansion coefficient, reactivity, and conductivity, $Pr_{1-x}Sr_xMnO_{3-d}$ and $Nd_{1-x}Sr_xMnO_3$ are the most promising electrode materials. Despite extended high-temperature treatments, the performance of $Nd_{1-x}Sr_xMnO_{3-d}$ with gadolinium doped ceria (GDC) electrolyte (which is best suited for IT-SOFC application) showed no reaction between the components at the interface. In terms of chemical compatibility and electrical conductivity, however, using calcium as a dopant can lead to very positive results. For example, $Pr_{1-x}Ca_xMnO_{3-d}$ (x=0.3) doesn't react with the electrolyte and has an ideal conductivity [150–154]. To make use of the favorable features of cobaltites, these materials are doped with Fe. Even though adding Fe makes the orthoferrites less conductive, it also causes the TEC num-

bers to go down. The $Ba_{1-x}Sr_xCo_{1-y}Fe_yO_3$ (x=0.5, y=0.2) material stands out for SOFC cathode applications among these cobalto-ferrites. $La_{1-x}Sr_xFe_{1-y}Co_yO_3$ has also received much attention as cathode materials. These cobalt-based oxides perform more electro-catalytically than traditional LSM cathodes[155, 156]. Unfortunately, they have a high cobalt cost, and easy cobalt evaporation and reduction. Pr-doped orthoferrites have shown promising potential as cathode materials for high-temperature solid oxide fuel cells due to their combined electronic and ionic conductivity. Among these materials, $Pr_{1-x}Sr_xFe_{1-y}Ni_yO_{3-d}$ (x =0.2, y =0.2) stands out for its good oxygen ion conductivity and low electrical resistivity [157–163]. Double perovskite materials such as $GdBaCo_2O_{5+x}$, $PrBaCo_2O_{5+x}$, $SmBaCo_2O_{5+d}$, or $NdBaCo_2O_{5+d}$ have also been studied for IT-SOFC applications. Compared to many single perovskites, they exhibit higher ORR activity. However, due to their high thermal expansion coefficients, they are currently incompatible with the electrolytes developed so far [164–166].

Another approach to improve cathodic performance is to create composite cathodes, which consist of a solid electrolyte and an electronic conducting electrocatalytic material. For example, $La_{1-x}Ca_xFe_{1-y}Ni_yO_{3-d}$ (x=0.4, y=0.2)/$Sm_{0.2}Ce_{0.8}O_{1.9}$ symmetrical cells have been previously reported to have good performance. Other composite cathodes that are currently being investigated include $Sm_{1-x}Sr_xCoO_3$ /$Ce_{1-x}Sm_xO_{1.9}$ (SSC/SDC), $La_{1-x}Sr_xCo_y\ Fe_{1-y}O_3$/SDC (LSCF/SDC), LSCF/$Ce_{1-x}$ Gd_xO_2 (LSCF/GDC), and $Ba_{1-x}Sr_xCo_y\ Fe_{1-y}O_3$/SDC (BSCF/SDC) [167–173].

1.4 SOFC Electrolytes

In SOFC, the electrolyte facilitates the oxide ion transport between the cathode and anode, thereby completing the electrical circuit, whose efficiency is pivotal to the performance of the cell. Hence, the electrolyte should have high oxide-ion conductivity with negligible electronic conductivity. Additionally, it should demonstrate high chemical and mechanical stability and compatibility with the paired electrodes at the operating temperatures of the cell. Typically, the high ionic conductivity is associated with materials having a crystal structure with a higher number of accessible sites and a low migration enthalpy of less than 1 eV. Further, because diffusion of ions is a thermally activated process, a fair amount of oxygen vacancies in the matrix generally promote ion transport. Several oxide-ion-conducting materials with potential applications as solid electrolytes in SOFCs have been identified in the past. Some of the notable examples of structural families are $LaGaO_3$ with

perovskite (ABO_3) structure, $Gd_2Zr_2O_7$ with pyrochlore ($A_2B_2O_7$) structure, and $Ba_2In_2O_5$ with brownmillerite ($A_2B_2O_5$) structure, doped ZrO_2, CeO_2 and Bi_2O_3 materials with fluorite (MO_2) structure [82, 174–186]. Below, we shall review the experimental and theoretical investigations on these structural families of oxides.

1.4.1 Perovskite -family

The ABO_3-type perovskite materials belong to the new generation of materials and are known for their exceptional flexibility. In the perovskite compound (ABO_3), A is a larger cation with a coordination number of 12, and B is a smaller one with a coordination number of 6. By selecting appropriate A and B site cations and adding dopants, it is possible to create a wide range of materials that possess diverse properties and applications [176, 187–189]. Various transition metals can occupy the smaller B sites, while the larger A cation sites may be occupied by alkaline earth and rare earth metals. It is possible to achieve high ionic conductivity by allowing cations with various ionic radii and valences to access one or more sites in the perovskite structure and obtaining high concentrations of oxygen vacancies [81, 177, 180, 189]. Catlow and his group [181, 190, 191] proposed that the diffusion of ions in perovskite-type $LaGaO_3$ lattices occurs when oxide ions move to the nearest vacant site along the edges of a BO_6 octahedron. They suggested that the ionic conductivity in perovskite materials is significantly influenced by the tolerance factor t, which is related to the ionic radii ratio of both the A and B-site cations. They also demonstrated that solid solutions of $(La,\ Sr)(Ga,\ Mg)O_{3-d}$ exhibit strong electrical conductivity at $t = 0.96$ and high electrical conductivity can be achieved in most perovskites at $t < 1$. Maximum ionic transport has been observed in the LSGM ($La_{1-x}Sr_xGa_{1-y}Mg_yO_{3-d}$) series for compositions where ($0.10 < x < 0.20$), ($0.10 < y < 0.20$) respectively. Goodenough and co-workers [180, 192, 192] suggested that the incorporation of Sr^{2+} and Mg^{2+} into $LaGaO_3$ results in a significant improvement in the oxide ion conduction properties of the material. Further experimental studies have been conducted, which have consistently confirmed these observations [193–196].

At temperatures below 800^0C, two groups of perovskite-like materials, gallates and cerates, have been synthesized to offer enhanced characteristics. Most of the research has been focused on Sr-doped $LaGaO_3$, but Ba and other dopants have also been studied. $LaBO_3$ oxides can benefit from the addition of acceptor dopant cations such as Mg^{2+}, Ba^{2+}, Sr^{2+}, In^{3+}, or Ca^{2+} at La^{3+} sites to enhance the ionic

conductivity [188, 194, 197, 198]. The molecular dynamics investigations on Ba-doped $LaInO_3$ indicate that oxygen conduction is influenced by both the quantity of oxide ion vacancies and the distribution of dopant (Ba^{2+}) ions [199, 200]. Perovskite aluminates, such as $LaAlO_3$, have been extensively researched since the 1970s [201–204]. Perovskites made of $LnBO_3$ (B = Y^{3+}, In^{3+}, Sc^{3+}, and Al^{3+}) are more stable and less volatile than $LaGaO_{3-d}$ and CeO_2 based electrolyte material. These materials are mechanically compatible and have moderate thermal expansion values, making them suitable for manufacturing SOFCs [205, 205–207, 207–210].

1.4.2 Brownmillerite-like phases

The chemical composition of brownmillerite oxides is represented by the formula $A_2B_2O_5$. Comprising alternating layers of perovskite, these oxides exhibit a structural arrangement where perovskite shares corners with BO_6 octahedra and BO_4 tetrahedra [161, 177, 211–214]. Commonly known as oxygen-deficient perovskites, they feature a notable presence of organized oxygen vacancies aligning along (010) planes. With increasing temperature, these materials undergo phase transitions, such as from the orthorhombic phase at room temperature to the tetragonal phase at 925–930°C, and further to the disordered cubic phase at 1040°C [215–218]. The disordered cubic phase, characterized by a significant number of oxygen vacancies, facilitates rapid oxide ion conduction. However, these materials are not suitable for use in humid environments. The theoretical studies on $A_2B_2O_5$ compounds (where A^{2+} includes Ba, Sr, Ca, and B^{3+} comprises Al, Fe, In) suggest that for maximum stability, the ionic radius of the A-site cation (r_A) should be greater than that of the B-site cation (r_B), with the ratio (r_A/r_B) falling between 1.6 and 2.1 [219–221]. Experimentally, it is reported that the conductivity of $Ba_2In_2O_5$ is of mixed type, with oxide ion conductivity being the predominant one. Introducing cations of higher valence, such as Zr^{4+}, Ce^{4+}, Sn^{4+}, or Hf^{4+} in place of In-sites, enhances ionic conduction at intermediate temperatures and stabilizes the disordered cubic perovskite phase [180, 222–224].

1.4.3 Pyrochlore Structure

Pyrochlores, having general formula $A_2B_2O_7$, represent a class of complex oxides where A-site cations are typically trivalent rare earths (e.g., Gd^{3+}, Y^{3+}, Dy^{3+}, La^{3+}), and B-site cations are tetravalent transition metals (e.g., Zr^{4+}, Ti^{4+}, Sn^{4+}, Ce^{4+}) [225–227]. Pyrochlores are the superstructure of the fluorite structure (XO_2),

featuring ordered A- and B-site cations with one-eighth of the anions are absent to create vacant sites. The coordination number of the larger-sized A^{3+} cations is 8, whereas the coordination number of B^{4+} is 6 [228]. The study by Tuller and his group [229, 230] on oxygen diffusion in $Gd_2(Zr_yTi_{1-y})_2O_7$ demonstrated that the addition of zirconium remarkably increased diffusivity by up to four orders of magnitude. Yamamura and co-workers [231] investigated various zirconate pyrochlore compounds $(Ln_{1-x}Ln'_x)_2Zr_2O_7$ ($Ln = Gd^{3+}, Sm^{3+}, Nd^{3+}; Ln' = Y^{3+}, Yb^{3+}, Gd^{3+}$) and observed that the ratio of ionic radii (r_{Ln}/r_{Zr}) plays a critical role in influencing the ionic diffusivity of these compounds. The MD study by Wilde and Catlow [232, 233] demonstrated an improvement in ionic conductivity through the introduction of cation disorder, marked by the exchange of A and B-site cations. This above statement is further supported by other studies [228, 234, 235]. The computational study by Dholabhai and co-workers [236, 237] demonstrated the complexity of various surfaces in pyrochlore oxides, including $Gd_2Ti_2O_7$ (GTO), $Gd_2Zr_2O_7$ (GZO), $La_2Zr_2O_7$ (LaZO), and $Lu_2Ti_2O_7$ (LuTO), where the (110) facet exhibits the highest energy stability. Additionally, their findings proposed a correlation between surface energy and disordering energy, and both were influenced by the B cation in $A_2B_2O_7$ compounds.

1.4.4 LAMOX -family

LAMOX, or $La_2Mo_2O_9$, based compound was first introduced by Lacorre et al. in the year 2000 [238]. Lacorre proposed that, the oxide ion conductivity of LAMOX is 6×10^{-2} S/cm, which is comparable to stabilized ZrO_2 at 800^0C. These materials transform from their room temperature monoclinic phase into a cubic around 580^0C. Due to this phase transition, their conductivity suddenly increases up to two orders of magnitude, which is similar to what happens with Bi_2O_3 and $Ba_2In_2O_5$ ion conducting oxides[239]. Subasri et al. [240] investigated the temperature-dependent ionic and electronic conductivity of $La_2Mo_2O_9$. Their findings indicated that the observed phase transition in $La_2Mo_2O_9$, has no noticeable impact on its conductivity. Notably, the total conductivity was approximately three orders of magnitude lower compared to the values reported by Lacorre et al. [239]. The MD simulation studies revealed that the long-range conduction in $La_2Mo_2O_9$ is driven by the varying coordination number of Mo and the movement of oxide ions within the MoO_x coordination sphere [241, 242].

1.4.5 Zirconia and Ceria Based Fluorites

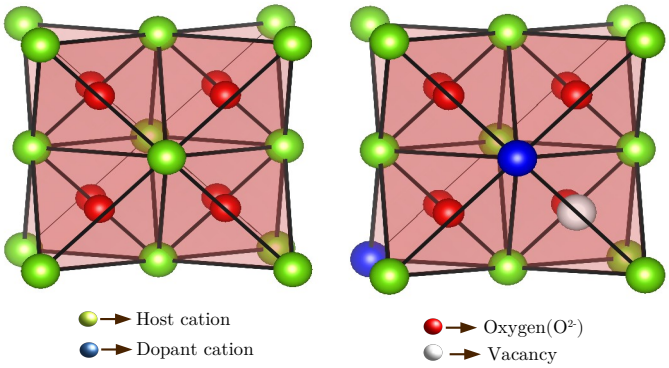

Figure 1.3: Schematic representation of cubic fluorite crystal structure.

Fluorite-structured electrolytes have tetrahedral sites where anions are located, while cations are organized in face-centered cubic positions, as illustrated in Figure 1.3. Only a few oxides (XO_2), such as CeO_2, ZrO_2, HfO_2, ThO_2, and UO_2, have a fluorite structure. Other oxides, like Bi_2O_3, have a defect-fluorite structure, in which two of the tetrahedral sites remain vacant [243–246]. Only a limited number of materials have been extensively examined as potential SOFC-electrolytes, specifically zirconia (ZrO_2), ceria (CeO_2), and bismuth oxide (Bi_2O_3). These materials use a vacancy diffusion mechanism for ion conduction. However, pure XO_2 (where $X = Zr$ or Ce) lacks a sufficient number of oxygen vacancies to demonstrate significant ionic conductivity. To enhance ionic conductivity, lower valence dopant cations such as Gd^{3+}, Sm^{3+}, Y^{3+}, Sc^{3+}, Yb^{3+}, and La^{3+} are introduced in place of the hosts X ($M = Zr^{4+}$ or Ce^{4+}) cations. This process induces oxygen vacancies into the structure, facilitating the diffusion of oxygen ions from their tetrahedral location to the oxygen-vacant site through a process called discrete hopping. Ionic conductivity increases with higher dopant or vacancy content and reaches its maximum at dopant concentrations of 10–20 mol% (depending on the dopant), and decreases thereafter. Remarkably, all these oxides, including ZrO_2, CeO_2, and Bi_2O_3, display this non-monotonic behavior of conductivity variation with dopant concentration. [247–254].

Unlike CeO_2, ZrO_2 occurs in three different polymorphs: monoclinic, tetragonal, and cubic fluorite. The monoclinic phase is stable at ambient temperature, the tetragonal phase is stable above 1170°C, and the cubic fluorite phase is stable above 2370°C, up to its melting point of 2680°C [255, 256]. But by substituting a small

number of acceptor dopant cations at Zr^{4+} position, it is possible to stabilize the high-temperature tetragonal and the cubic phase of ZrO_2 at ambient temperature. For instance, adding 8 mol% Y_2O_3 completely stabilizes the cubic phase in ZrO_2 and makes it stable up to $2500°C$, preventing it from changing into another phase. Adding acceptor dopant cations produces oxygen vacancies and enhances oxide ion conductivity. As a SOFC electrolyte, the exceptional ionic conductivity of YSZ facilitates effective ion transport between the anode and cathode, leading to higher power output. Additionally, YSZ's chemical stability and resistance to corrosion from fuel oxidants contribute to its long-term performance and reliability. YSZ is suitable for high-temperature applications due to its mechanical strength and ability to withstand at extreme temperatures. It also works with various electrode materials, including Ni-YSZ, Ni-$Sc_{0.1}Ce_{0.01}Zr_{0.89}O_{1.95}$, $Fe_{0.1}Ni_{0.9}$-YSZ, allowing for flexibility in design and material selection [249, 250, 250, 257–262].

Kilner and Brook [263] proposed that the ionic conductivity of ZrO_2-based materials is notably affected by the ionic radius of the dopant. Later, Arachi et. al. [264] demonstrated that the maximum conductivity of ZrO_2–Ln_2O_3 system at its operating temperature is influenced by both the dopant composition and the ionic radius of the dopant cations (the conductivity decreases as the ionic radius of dopants increases). Additionally, the migration enthalpy increases and the association enthalpy decreases with an increase in dopant ion radius. The aforementioned concept is further supported by a number of relevant experimental and theoretical studies [265–270]. Catlow et al. [271] using extended X-ray absorption fine structure and neutron scattering, proposed that oxygen vacancies are situated in proximity to the smaller zirconium (Zr^{4+}) ions, whereas Welberry et al., [272] through experimental methods, such as optical and mechanical spectroscopy, suggested that oxygen vacancies are located in proximity to larger stabilizer ions (dopant).

Based on molecular dynamics studies on ZrO_2-based materials, Islam and his group [273] proposed that cation dopants with larger ionic radii than the host Zr^{4+} facilitate the positioning of oxygen vacancies at next-nearest-neighbor (NNN) sites. Conversely, 'undersized' dopants assist in situating the vacancies at nearest-neighbor (NN) positions. Shimojo and Okazaki [274, 275] performed molecular dynamics study on YSZ and demonstrated that $Y_xZr_{1-x}O_{2-x/2}$ with $x = 8$ mol% exhibits maximum oxygen ion conductivity. They also stated that there is no specific arrangement of oxygen vacancies within this composition. Meyer et al. [276] employed Monte Carlo (MC) simulations to explore the impact of vacancy-dopant interactions on oxygen migration behavior. Their findings align with both the experimental re-

sults and the MD simulation results conducted by Shimojo and Okazaki. Krishnamurthy and co-workers [277] carried out density functional theory (DFT) studies to create a database of oxygen ion migration energy barriers for different nearest-neighbor configurations. Following this, they utilized kinetic Monte Carlo (KMC) simulations based on the DFT data to explore the temperature-dependent behavior of oxygen-ion diffusion. Tarancon and coworkers [278] performed MD simulations on YSZ and GDC to elucidate the local effects of dopants on ionic diffusion in doped fluorites. The investigation comprehensively addresses conduction models, energy landscapes, oxygen diffusion, dopant-oxygen distances, migration pathways for vacancies, and the assessment of jump efficiency. Chatterjee and co-workers [279] recently emphasized the importance of oxygen ion-vacancy pairs in determining the ionic conductivity of YSZ. Using MD trajectories for YSZ, they have calculated the free energy of oxygen ion-vacancy pairs, hopping rates, and the corresponding Arrhenius parameters in various cation environments.

Although ZrO_2 based materials are popular for SOFC electrolytes, they have certain drawbacks as well. YSZ material achieves reasonable conductivity only at very high operating temperatures (often exceeding 1000°C), which can lead to increased system complexity, cost, and difficulties with system design and material choice. YSZ also has comparatively poor fuel oxidation electrochemical activity, which can reduce SOFC performance [262, 280–284]. Scandia-stabilized zirconia (ScSZ) has been found to have the higher ionic conductivity than YSZ, as the ionic size of Sc^{3+} is smaller than Y^{3+} and close to that of Zr^{4+}. The material ScSZ has the ability to lower the operating temperature of SOFCs to intermediate values due to its high ionic conductance and low electronic conductivity. Although ScSZ has a high ionic conductivity, it poses certain challenges that include temperature-dependent phase transitions, high market price and poor accessibility [285–289]. Although YSZ is the most commonly used material for the electrolyte in SOFCs, researchers continue to explore alternative materials that could be used as substitutes for YSZ in SOFCs to improve their performance, lower their costs, and reduce their environmental impact.

Cerium oxide (CeO_2) exhibits promising potential as an alternative to YSZ electrolyte material for SOFC. In contrast to ZrO_2, CeO_2 preferred to remain in its cubic phase without the addition of any dopants or stabilizers. Although pure CeO_2 is a poor ionic conductor, it can be improved by doping it with lower valent oxides such as rare-earth oxides (Gd_2O_2, Y_2O_3, Sm_2O_3, La_2O_3, Nd_2O_3) [245, 246, 253, 290, 291]. For example, gadolinium (Gd_2O_3) is commonly used as a dopant in CeO_2-based elec-

trolytes, having higher ionic conductivity compared to YSZ [69, 80, 87, 292, 293, 293, 294]. In general, ceria doped with Gd^{3+}, Sm^{3+}, Nd^{3+}, and Y^{3+} demonstrates higher ionic conductivity than other rare earth cations at low temperatures. However, the cost of Sm_2O_3 and Gd_2O_3 is relatively high. Another material explored as a viable electrolyte for SOFCs is yttria-doped ceria (YDC), known for its reliable chemical stability and resistance to sintering [295–300]. The choice of dopant for CeO_2 depends on the specific application and desired performance characteristics. For low-temperature SOFCs, YDC may be preferred, while GDC and SDC may be more suitable for intermediate-temperature applications. The concentration of dopant used can also impact the performance of the electrolyte [301–306].

The ionic conductivity of rare earth doped ceria ($Ce_{1-x}RE_xO_2$) continuously increases with increasing dopant (RE) concentration up to an optimal value (10-20 mol% depending on the dopant) and then drops thereafter. Faber et. al. [307] proposed that conductivity variation is related to the vacancy-dopant interaction and there is an optimal dopant ($RE = Y^{3+}$, Gd^{3+}, Nd^{3+}, La^{3+}, Yb^{3+}) size for enhanced ionic conductivity. The experimental study by Koettgen and Martin [308, 309] demonstrated that Sm^{3+} doped ceria has higher amounts of both bulk and total conductivity than Gd^{3+}-doped ceria. Burbano et. al. [310] proposed that the drop in ionic conductivity with increasing dopant concentration in fluorite-structured materials like YDC is ultimately determined by the vacancy-vacancy interactions. Omar et al. [311] established a correlation between ionic conductivity and lattice elastic strain in 10 mol% trivalent cations doped CeO_2 at high temperatures. Their experiments demonstrated that at a concentration of 10 mol%, the ionic conductivity rises up as the size of the dopant increases, with Nd^{3+} displaying the highest grain ionic conductivity.

Butler et. al. [303] used the generalized Mott-Littleton method to do lattice simulations on doped CeO_2. Their results suggested that the ionic radius of the dopants has the most significant effect on the interaction between vacancies and dopants. Minervini et al. [312] found that the interaction was least effective when the size of the dopant was closely comparable to the size of the host cation (Ce^{4+}), and Gd^{3+} is chosen as the best dopant for improved ionic conductivity in CeO_2-based materials. Molecular Dynamics study by Inaba et. al. [313] on $Ce_{1-x}Gd_xO_{3-\delta}$ suggested that Gd^{3+} has a lower oxygen coordination number than Ce^{4+}. They also found that Ce^{4+} ions are not next to vacancies, where Gd^{3+} ions form a Gd^{3+}–vacancy-Gd^{3+} cluster. Dholabhai et al. [314] performed a theoretical investigation on SDC (samarium doped ceria) and demonstrated the trends in the variation of oxygen ion

conductivity with temperature and dopant content. There, the activation energies for the migration of oxygen vacancies along different migration pathways in SDC are calculated, which facilitates the analysis of vacancy-mediated diffusion. Additionally, they showed that the conductivity rises initially due to an increase in vacancy concentration, but decreases later due to reduced vacancy mobility caused by vacancy-dopant association, which can lead to vacancy ordering. Through the MD analysis, Adler and Smith [315] demonstrated that in Y_2O_3-doped CeO_2, the dopant is linked to oxygen vacancies. They provided an explanation for the non-linearity in electrical conductivity, attributing it to the influence of long-range Coulomb effects. As per Hayashi et al. [316] the increased diffusion coefficient observed in doped-CeO_2 can be attributed to the optimal size of the dopant, leading to minimal local expansion or contraction around the dopant site.

CeO_2 and its derivatives tend to reduce to Ce^{3+} ions at high temperatures and low oxygen partial pressures (often happens at the anode side of SOFC operations), which are the main issues limiting their use as electrolytes [150, 317–319]. Some researchers have employed co-doping YSZ, GDC, YDC, etc. to address these problems. Another strategy used is to synthesize bi-or tri-layers of sandwiched CeO_2 and ZrO_2 layers, doped with a trivalent cation. The latter technique causes the solid electrolyte phases to generate an interfacial reaction, which might reduce the total ionic conductivity. Also, the different thermal expansion (TE) and the thermal stress that builds up between the phases make the layers prone to microcrack [320–323].

Herle et al. [324] observed that co-doping ceria with alkaline earth and rare earth ions, resulted in considerably higher conductivity when compared to the best-performing singly doped ceria materials with equivalent oxygen concentration. According to the computational investigation led by Dholabhai and co-workers [325], GPDC (gadolinium-praseodymium doubly doped ceria) demonstrates higher ionic conductivity compared to PDC (praseodymium-doped ceria) or GDC. Zheng et al. [326] found that co-doping ceria ($Ce_{1-x}La_{x-y}Ca_yO_{2-d}$) with an appropriate amount of La^{3+} and Ca^{2+} resulted to much enhanced ionic conductivities and lower activation energies than singly doped ceria. Introducing a small quantity of 2 mol% yttria (Y_2O_3) into ScSZ stabilizes its cubic phase and induces a slight reduction in the electrical conductivity of ScSZ. However, this decrease can be counteracted by introducing additional ceria, leading to an enhancement in conductivity [327]. The MD investigation on Sc^{3+} co-doped YSZ revealed that the ionic transport performance of YSZ improves as the concentration of Sc^{3+} increases. This improvement is attributed to the augmented free space and reduced structural expansion resulting

from the addition of Sc^{3+}, characterized by its smaller cation radius [328]. The MD study by Kilic and Soon [329] showed that the ionic conductivity of yttria-doped ScSZ is lower than that of both YSZ and ScSZ due to the structural instability of the system. A summary of the materials discussed in this chapter covering the anode, cathode, and electrolyte components of SOFC is presented in table 1.4.

Anode	Electrolyte	Cathode	Operating Temperature (°C)	ref.
NiO-YSZ	YSZ	LSM-YSZ	1000	[330]
Ni-SDC	YSZ	LSM-YSZ	800	[331]
Ni-YSZ	YDC	LSCF	550	[332]
Ni-YSZ/YDC	YSZ	LSM-YDC	650	[333]
Cu-CeO2-YSZ	YSZ	YSZ-LSM	800	[334]
LSCM-YSZ	YSZ	LSM	850	[135]
Cu-CeO2-YSZ	ScSZ	$Pr_{1-x}Ca_xMnO_3$	800	[335]
Ni-GDC-ScSZ	ScSZ	$Pr_{1-x}Ca_xMnO_3$	800	[336]
Ni-YDC	YDC	LSCF	700	[332]
Ni-GDC	GDC	LSCF-GDC	600	[337]
NiO-SDC	SDC	$Sm_{0.5}Sr_{0.5}CoO_3$	500	[338]
Cu-Ni-GDC	GDC	LSCF	600	[339]
Ni-YDC	LSGM	LSC	700	[338]

Table 1.4: Performance of specific anode, electrolyte, and cathode materials in fuel cells, together with their operating temperature.

1.5 Summary

A survey of experimental and computational studies on a range of electrolyte materials of diverse structural families, such as perovskite, brownmillerite, fluorite, etc, has been presented. Arguably, materials based on ZrO_2 and CeO_2 are among the most promising electrolytes for accelerating the electrochemical process in high- and intermediate-temperature SOFCs, while ensuring good compatibility and chemical stability with other electrode materials.

The ionic conductivity observed in electrolytes based on ZrO_2 and CeO_2 is a result of oxide ion migration through vacancies. These vacancies are introduced into the matrices through the doping of divalent or trivalent cations, such as Y^{3+}, Sc^{3+}, Gd^{3+}, Sm^{3+}, Ca^{2+}, Mg^{2+}, and La^{3+}. Previous experimental and theoreti-

cal studies have concluded that the trend of increasing conductivity with increasing dopant concentration follows up to the range of 8–20 mol%, after which the conductivity decreases. The lattice parameter, ionic conductivity, and activation energy of electrolyte materials based on CeO_2 and ZrO_2 are affected by multiple factors, including the dopant type, valence charge of dopant, and doping level, as well as the ionic radius of the dopant. Doping ZrO_2 with a certain mol% of lower-valent cations leads to a decrease in ionic conductivity as the size of the dopant ion increases. Proposedly, this reduction is linked to a simultaneous decrease in the pre-exponential factor and a rise in activation energy, both of which are related to the increasing size of the ionic radius. Theoretical and experimental observations consistently indicate that among various dopants, yttria (Y^{3+}) exhibits superior performance in terms of conductivity, stability, and compatibility when introduced into both ZrO_2 and CeO_2. The non-monotonic changes in ionic conductivity with dopant concentration has been ascribed to various factors, including the trapping of vacancies, the strong binding of vacancies with dopant ions, the elevated activation energy, the influence of cationic edges, and the local environment. Despite experimental and computational efforts, the mechanism that governs oxygen ion conductivity and its correlation with the optimal dopant concentration remains unclear.

1.6 Objective of the thesis

The survey above highlights that concerted efforts, with computational and experimental techniques mutually complementing, will be necessary for the advancement of viable fuel cell technology. Molecular dynamics (MD) makes a powerful atomistic computer simulation approach, that is a very effective tool for studying material properties at the atomic length and time scales. These methods have been effectively applied in the past four decades in the study of a variety of complex phenomena relating to the condensed states of matter. Numerous significant microscopic insights into ion transport in materials, including the mechanism of ion mobility, microscopic energetics, and migration channels, are within the scope of MD simulations. The thesis presents MD simulation studies on yttria-doped ZrO_2 and CeO_2-based SOFC electrolytes, with the objective of bringing out microscopic insights into the various factors controlling oxygen ion transport in these systems. The remaining chapters of the thesis are organized as follows:

- In Chapter 2, the thesis highlights the theoretical framework underpinning the computational methods employed in the studies.

- Chapter 3 discusses investigations into oxide ion transport in yttria-doped ceria. The findings offer valuable insights, including details on microscopic energy barriers, local environments of oxygen ions, residence times of oxygen ions at their tetrahedral sites, etc.

- In Chapter 4, NPT ensemble-molecular dynamics simulations are used to investigate the structural and dynamic properties of yttria-stabilized zirconia (YSZ), over a wide range of dopant concentrations and temperatures. The analysis specifically delves into the energetics of various pathways connecting oxygen sites, further resolving these pathways along distinct cationic edges such as Zr-Zr, Zr-Y, and Y-Y, which forms the saddle point for ion migration.

- In Chapter 5, the influence of cationic distribution (Zr^{4+}/Y^{3+}) in the YSZ matrix on oxide ion transport is investigated. The mobility of oxide ions is compared across five distinct Zr/Y-ordered structures at a yttria doping of 12.5 mol%. The study finds that certain cationic ordering can enhance the ionic conductivity up to four orders of magnitude with respect to the randomly ordered structure. Further, useful insights on how the cationic ordering facilitates enhanced oxygen migration in the system are discussed.

- The findings of the study are summarized in Chapter 6, along with a glimpse at possible future directions.

Chapter 2

Theoretical Background

2.1 Introduction

Except for a limited class of "exactly solvable" problems in science and engineering, "closed-form" analytical solutions are beyond hope. Thus, in many "real-life" scenarios, computational techniques need to be called in. For instance, condensed matter physics involves a large number of mutually interacting particles, which makes it a very complex system necessitating the use of numerical techniques. Computational techniques employ suitable algorithms to achieve the goal, with the help of programming languages or already available software tools. These techniques are variably referred to as numerical analysis, modeling and simulation, machine learning, and data visualization, depending on the nature of the algorithm used. Over the years, in concurrence with the rapid growth of computational power numerical algorithms have also evolved into more efficient and robust techniques.

The earliest instance of computer simulation for scientific research is done by N. Metropolis et al., [340] who employed the Monte Carlo (MC) simulations in 1953 to study the nature of fluids. Since its introduction, the Monte Carlo method has been used to solve a broad variety of physics, chemistry, and engineering problems. In the 1960s and 1970s, computer simulation became more widespread, and researchers created novel techniques such as finite element analysis and molecular dynamics (MD) simulations. With the aid of these methods, scientists were able to simulate the behavior of complex systems in an unprecedented level of detail [341–348]. These computational techniques have contributed to advancements in several disciplines ranging from materials sciences to drug discovery [349–363].

2.2 Molecular Dynamics

Molecular dynamics (MD) simulation is a computational method for studying the structure and dynamics of systems composed of atoms or molecules at finite temperatures. Compared to other computational methods, they have benefits like realistic emulation of systems, adaptability in modeling and high accuracy in predicting structural and dynamical properties. The technique thus provides a microscopic understanding of physico-chemical processes and yields best when employed complementary with experimental studies[364, 365]. Alder and Wainwright first introduced the method in the late 1950s[366]. The method was originally developed in order to better understand how gases act in extreme environments, such as high-temperature plasmas. The present-day structure of the MD algorithm owes much to the work "Correlations in the Motion of Atoms in Liquid Argon" by Aneesur Rahman on Lennard-Jones fluids in 1964 [367]. The fundamental concept behind MD is to model the interactions between individual atoms or molecules using classical physics. To do so, the forces operating on atoms and molecules must first be defined in terms of their positions. Then, using numerical techniques, one must solve the equation of motion of the system[364, 365]. Early MD simulations studied basic liquids like argon and water, and calculated thermodynamic properties like the equation of state and transport coefficients[367, 368]. In the 1970s and 1980s, faster computers permitted the handling of more realistic models, albeit more complex, expanding the scope of MD simulations. Thus, MD simulation became a popular tool in the study of proteins and other biological macromolecules in the 1990s and 2000s. In recent years, researchers have used MD simulations to investigate more complex systems like cell membranes, nanoparticles, and organic compounds. The development of graphics processing units (GPUs) and specialized MD software packages, among other developments in computer hardware and software, has made it possible to simulate bigger systems for longer times, enabling researchers to study more complex phenomena [369–371].

MD algorithm can be primarily classified as classical[366] and *ab initio*[372], based on the use of empirical force-field against "on-the-fly" estimation of interaction using density functional theory (DFT)[373]. Classical MD studies are sometimes used in conjunction with "coarse-grained" models or with "replica exchange" techniques for speed-up or efficiency of simulations. Coarse-grained molecular dynamics (CGMD) reduces the effective number of particles in a molecular system by grouping atoms into larger particles, or "beads", for speeding up the simulations. Replica

exchange molecular dynamics (REMD) simulates a system at different temperatures or thermodynamic conditions, and the results are then 'stitched' together using statistical principles for better statistical efficiency. These techniques are commonly employed in the study of systems containing long-chain molecules, such as proteins and polymers. Since *ab initio* molecular dynamics (AIMD) technique[372] performs on-the-fly estimation of atomic interactions (that is, in tandem with the evolution of the nuclear coordinates, solving the electronic structure problem within DFT formalism[373]), they can be employed in the study of chemical reactions [374–377]. Despite their higher accuracy, AIMD simulations are computationally several orders of magnitude expensive compared to classical MD. Hence, AIMD techniques pose severe limitations on the system size and timescales of simulations.

2.3 Classical Molecular Dynamics

The structural and transport characteristics of a classical many-body system can be efficiently computed using classical molecular dynamics simulation techniques. "Classical" alludes to the nuclear motion of constituent particles that comply with the laws of classical (Newtonian) mechanics. The forces between atoms are directly calculated in molecular dynamics, and the motion of the atoms is computed using an appropriate numerical integration technique to solve Newton's equation of motion,

$$\boldsymbol{F} = m\boldsymbol{a} = m\frac{d\boldsymbol{v}}{dt} = m\frac{d^2\boldsymbol{r}}{dt^2} = \frac{d\boldsymbol{p}}{dt} \tag{2.1}$$

where m is the mass of the atom, a is the acceleration and p is the momentum. [364, 365]. The forces are calculated from the interatomic potential, $U_{ij}(r_{ij})$,

$$\boldsymbol{F_{ij}}(r_{ij}) = -\boldsymbol{\nabla} U_{ij}(r_{ij}) \tag{2.2}$$

where r_{ij} denotes the interatomic distance between two atoms labeled i and j. N denotes the total number of atoms in the system. The total force on each particle due to the rest of the particles is calculated as,

$$\boldsymbol{F_i} = \sum_{j=1,\, j\neq i}^{N} \boldsymbol{F_{ij}}(r_{ij}) \tag{2.3}$$

Newton's equation can now be used to calculate the acceleration ($\boldsymbol{a_i}$) of the ith particle with mass m_i, which can be written as,

$$\boldsymbol{a_i} = \frac{\boldsymbol{F_i}}{m_i} \tag{2.4}$$

MD simulations follow the following algorithm:

1. *Initialisation*:- The initial positions of each atom are assigned based on available X-ray data, and the velocity component of each atom is selected from the Maxwell Boltzmann distribution. Subsequently, other parameters such as simulation temperature, pressure, and time step are also assigned.

2. *Force Calculation*:- The forces are computed based on the pairwise interaction potential energy, and subsequently, Newton's equation is employed to determine accelerations from these forces.

3. *Motion evolution*:- The new data set is obtained by updating the positions and velocities of each atom by integrating the equation of motion.

The steps (1-3) mentioned above are iterated to get the trajectory of each atom over the simulation time. After equilibration, the trajectory is analyzed for structural, dynamical and thermodynamic properties of interest.

The most expensive process in a molecular dynamics simulation is typically the calculation of the atomic forces. If the system contains N atoms, there will be a maximum of $N(N-1)/2$ different atom pairs, each of which has a force that needs to be calculated. Thus, the computational duration for a molecular dynamics simulation is (roughly) proportional to N^2. However, a cut-off is typically implemented at a specific interatomic distance, after which the force is thought to be zero. Since all atom pairs are no longer required to be taken into account, the forces can be calculated much faster as a result.

2.4 Integration algorithms

An integration algorithm serves as an approximate numerical method for advancing the system by finite-time increment. Many integration algorithms have been developed to meet essential requirements such as accuracy (providing a precise depiction of atomic motion), stability, speed (quickly determining atom velocities), and efficiency (using minimal computer memory and resources). In molecular dynamics

programming, the Verlet algorithms are regarded as typical integration algorithms because they possess all these advantages [364, 365]. Thus the Verlet algorithm has two forms,

1. The Verlet algorithm,
2. The velocity Verlet algorithm.

2.4.1 Verlet algorithm

Loup Verlet [378] introduced the Verlet algorithm during the early phases of molecular simulation [365]. The algorithm involves the following steps, including Taylor expansion for both forward and backward positions in time, and can be expressed as follows,

$$\boldsymbol{r}_{t+\delta t} = \boldsymbol{r}_t + \boldsymbol{v}_t \delta t + \frac{1}{2}\boldsymbol{a}_t(\delta t)^2 + \frac{1}{3!}\frac{d^3\boldsymbol{r}}{dt^3}(\delta t)^3 \tag{2.5}$$

$$\boldsymbol{r}_{t-\delta t} = \boldsymbol{r}_t - \boldsymbol{v}_t \delta t + \frac{1}{2}\boldsymbol{a}_t(\delta t)^2 - \frac{1}{3!}\frac{d^3\boldsymbol{r}}{dt^3}(\delta t)^3 \tag{2.6}$$

The final expression for position at time step $t + \delta t$, can be derived by combining the above two equations. Thus,

$$\boldsymbol{r}_{t+\delta t} = 2\boldsymbol{r}_t - \boldsymbol{r}_{t-\delta t} + \frac{\boldsymbol{f}_t}{m}(\delta t)^2 + O(\delta t)^4 \tag{2.7}$$

This algorithm requires the position one step backward, $\boldsymbol{r}_{t-\delta t}$, for predicting the position at a forward time step, $\boldsymbol{r}_{t+\delta t}$. However, the calculation of velocities are essential for determining kinetic energy. Thus, velocities are calculated indirectly by using the positions, and can be expressed as

$$\boldsymbol{v}_t = \frac{(\boldsymbol{r}_{t+\delta t} - \boldsymbol{r}_{t-\delta t})}{2\delta t} + O(\delta t)^2 \tag{2.8}$$

δt refers to the time step of the range of femtoseconds ($10^{-15}s$). Despite the simplicity of the algorithms, certain aspects are unsatisfactory. One drawback of this algorithm is that the velocity is not explicitly expressed in the equation of motion; instead, it is computed using the standard central difference method. The atomic positions are explicitly provided for the time step $t + \delta t$, while the velocities are provided for the time step t, meaning one time step behind. It is evident that to calculate velocities, we need to track atom positions for three consecutive time steps. It also exhibits relatively accurate position determination with a small error of $O(\delta t^4)$, while the

error associated with velocity is $O(\delta t^2)$. However, it is feasible to develop variants of the Verlet algorithm that eliminate these minor limitations.

2.4.2 Velocity Verlet Algorithm

The velocity Verlet algorithm provides both atomic positions and velocities simultaneously at a given time, representing the most comprehensive form of the Verlet algorithm. The algorithms are as follows:

$$\boldsymbol{r}_{t+\delta t} = \boldsymbol{r}_t + \boldsymbol{v}_t\, \delta t + \frac{1}{2}\boldsymbol{a}_t \delta t^2 \tag{2.9}$$

$$\boldsymbol{v}_{t+\delta t} = \boldsymbol{v}_t + \frac{1}{2}[\boldsymbol{a}_t + \boldsymbol{a}_{t+\delta t}]\delta t \tag{2.10}$$

In practice, these two equations are split further into three,

$$\boldsymbol{v}_{t+\frac{\delta t}{2}} = \boldsymbol{v}_t + \frac{1}{2}\boldsymbol{a}_t \delta t \tag{2.11}$$

$$\boldsymbol{r}_{t+\delta t} = \boldsymbol{r}_t + \boldsymbol{v}_{t+\frac{\delta t}{2}} \delta t \tag{2.12}$$

$$\boldsymbol{v}_{t+\delta t} = \boldsymbol{v}_{t+\frac{\delta t}{2}} + \boldsymbol{a}_{t+\delta t}\frac{\delta t}{2} \tag{2.13}$$

In this formulation, the initial equation computes a half-step velocity based on the force and velocity from time step t. This is adequate for calculating the atom positions at time step $t+\delta t$, as articulated in the second set of equations. Ultimately, utilizing the forces derived from the new atomic position $\boldsymbol{r}_{t+\delta t}$, the half-step velocity is updated to the full-step velocity $\boldsymbol{v}_{t+\delta t}$. This version of the velocity Verlet algorithm offers advantages in terms of less computer memory requirements, as it only needs to retain one set of positions, forces, and velocities at any given time.

2.5 Periodic Boundary Condition

In MD simulations, periodic boundary conditions (PBCs) are a key technique for overcoming finite-size limitations and simulating an infinite system by replicating the simulation box in all dimensions. The simple logic described below supports putting periodic boundary conditions on small systems. A typical number of atoms in a real system is of the order of 10^{23}, whereas the number of atoms used in computer simulation is usually in the range of 1000–10000 (of simulation box length $20\mathring{A} - 40\mathring{A}$). Consider a sphere of radius r and thickness dr. The surface atoms to total

atoms ratio can be expressed as,

$$\frac{N_{surface}}{N_{total}} = \frac{\rho\ 4\pi r^2 \delta r}{\rho \frac{4}{3}\pi r^3} = 3\frac{\delta r}{r} \tag{2.14}$$

This ratio is roughly small for a bulk system, whereas it is much higher in a typical simulation. PBCs ensure that simulated particles do not interact with the surface of the simulation box, preventing artifacts in the simulation results. In this technique, the original simulation cell is surrounded by replicas of the original simulation cell. During the simulation, when a molecule moves within the primary box, its replicated images in neighboring boxes mimic the same motion precisely. Consequently, as a molecule exits the central box, one of its replicated images enters through the opposite face (as shown in Figure 2.1). There are no barriers at the boundary of the central box, and there are no molecules present on its surface. Thus, the particle number density is conserved throughout the primary box, which comprises the entire system. The formula used to generate image coordinates (x_{im}, y_{im}, z_{im}) for an orthogonal simulation cell (with sides L_x, L_y, *and* L_z) can be expressed as,

$$\begin{aligned} x_{im} &= x_{sim} + n_x L_x \\ y_{im} &= y_{sim} + n_y L_y \\ z_{im} &= z_{sim} + n_z L_z \end{aligned} \tag{2.15}$$

where n_x, n_y, n_z are positive or negative integers, including zero, and x_{sim}, y_{sim}, and z_{sim} are the coordinates of particles in the original simulation cell. In principle, it is essential to account for all interactions between molecules within the central box and their respective images in surrounding boxes. Thus infinite pairs of interactions can be evaluated, which is physically not possible. To address this, an approximation is adopted which is known as the 'minimum image convention'. This involves defining a region, usually a circle centered on the tagged molecule in the primary box, and considering interactions with real and image molecules whose centers fall within this defined region (as demonstrated in Figure 2.1). Therefore, the primary contributions to the potential and forces originate from neighboring molecules, in close proximity to the molecule of interest. Typically, for short-range forces, a spherical cutoff is applied for restricting interactions up to a certain distance. This involves setting the pair potential $U(r)$ to zero for $r \geq r_c$, where r_c is the cutoff distance. Importantly, the cutoff distance must not exceed $L/2$ for consistency with the minimum image convention [364, 365]. For non-orthogonal simulation boxes, real coordinates should

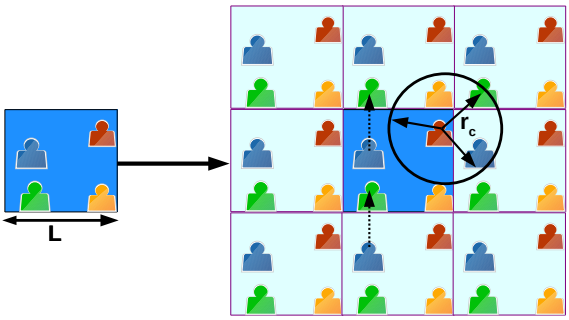

Figure 2.1: The minimum image convention for a two-dimensional system, where the central 'box' represents the primary simulation cell containing four atoms. The cutoff is depicted by the black solid circle.

be transformed to scaled coordinates using an appropriate matrix transformation. For this purpose, and H-matrix is defined as follows,

$$H = \begin{pmatrix} a_x & b_x & c_x \\ 0 & b_y & c_y \\ 0 & 0 & c_z \end{pmatrix} \tag{2.16}$$

The corresponding components of the cell parameter are denoted by the x, y, and z subscripts of the cell parameters a, b and c. The equation used to determine the scaled coordinates for an atom whose actual coordinates are x, y, and z is,

$$\boldsymbol{S}_{scaled} = H^{-1}\boldsymbol{X} \tag{2.17}$$

$$where \quad \boldsymbol{S}_{scaled} = \begin{pmatrix} x_{scaled} \\ y_{scaled} \\ z_{scaled} \end{pmatrix} \quad and \quad \boldsymbol{X} = \begin{pmatrix} x \\ y \\ z \end{pmatrix}$$

The equivalent coordinates in an orthogonal simulation box with sides of one unit length are provided by scaled coordinates. For a cubic box with unit dimensions, the PBC can be employed in the usual manner by following PBC equations. The coordinates are then converted back to real coordinates by following the equation,

$$\boldsymbol{X} = H\boldsymbol{S}_{scaled} \tag{2.18}$$

2.6 Interatomic Potential

The interatomic potential form and simulation parameters have a significant impact on the precision of the findings generated by classical MD simulation. The interatomic potential controls the balance between attraction and repulsion between atoms when they are close enough to each other. Each atom within a system interacts simultaneously with every other atom in the system, which implies the presence of two-atom interactions, three-atom interactions, and so forth. For the sake of simplifying the analysis, we exclusively focus on pair interactions and overlook higher-order interactions. The majority of pair potentials exhibit short-range characteristics, diminishing exponentially and approaching zero within a certain distance (up to a few neighbors). In the case of ionic solids, where ions may be polarized or charged, the Coulombic component can extend over a considerable distance, resulting in a very long-range interaction. Consequently, when describing potentials for these solids, it becomes necessary to account for two distinct pair-interaction terms: short-range potentials and long-range potentials ($\frac{1}{r^n}$, where $n \leq 3$). Lennard-Jones [364, 379], Born-Mayer [364], and Vashistha-Rahaman [380], are some examples of interatomic potentials that are frequently used. The Lennard-Jones potential [364] takes the following form,

$$U_{ij} = 4\epsilon_{ij}\,[(\frac{\sigma_{ij}}{r_{ij}})^{12} - (\frac{\sigma_{ij}}{r_{ij}})^{6}] \tag{2.19}$$

σ_{ij} denotes the equilibrium separation, and r_{ij} signifies the separation between particle i and j. ϵ_{ij} measures the depth of the pair potential at its equilibrium point. The second term in the bracket represents the attractive component arising from instantaneous dipole-dipole interactions, while the first term illustrates the Pauli repulsion resulting from overlapping electron clouds. This potential has been employed in simulations of inert gases such as argon [381, 382]. However, for certain ionic solids, the Lennard-Jones potential has been augmented with an additional Coulombic term [383].

One of the most common potentials for simulating ionic alkali halides is Born Mayer Huggins (BMH) potential, and it has the functional form as,

$$U_{ij} = \frac{q_i q_j}{r_{ij}} \; + \; A_{ij}\exp(-\frac{r_{ij}}{\rho_{ij}}) - \frac{C_{ij}}{r_{ij}^6} \tag{2.20}$$

here, q_i and q_j denote the charges of the ith and jth particles, while A_{ij} and ρ_{ij} represent the strength and range of the overlap repulsive term, respectively. The

dipole-dipole interaction term is denoted by C_{ij}. The repulsive component of this potential features an exponentially decaying term, which has a more robust theoretical foundation than the Lennard-Jones $\frac{1}{r^{12}}$ term. The Born-Mayer-Huggins (BMH) potential has found widespread use in simulating molten salts and various inorganic solids, including β-alumina [384], $SrCl_2$ [385], CaF_2 [386, 387], $LiMn_2O_4$ [388], $Gd_2Zr_2O_7$ [232], and others.

Vashistha and Rahaman [380] introduced a new functional form of interatomic potential, for the study of superionic conductor, α-AgI, in 1978, which can be represented as,

$$U_{ij} = \frac{q_i q_j}{4\pi\epsilon_0 r_{ij}} + A_{ij}\frac{(\sigma_i + \sigma_j)^n}{{r_{ij}}^n} - \frac{P_{ij}}{r_{ij}^4} - \frac{C_{ij}}{r_{ij}^6} \tag{2.21}$$

q_i, q_j, σ_i, and σ_j represent the charges and ionic radii of the ith and jth ions. The parameters A_{ij}, P_{ij}, and C_{ij} characterize, in respective order, the overlap-repulsion energy of the electron clouds, the average charge dipole interactions, and the dispersion constant between the ion pairs i and j. In comparison to the more familiar Born-Mayer (Buckingham) and Lennard-Jones potentials, this potential form exhibits a milder overlapping repulsion ($\frac{1}{r^n}$, where $n = 11$, 9, or 7 for cation-cation, cation-anion, and anion-anion pairs, respectively). This potential has been successfully applied to the investigation of various superionic conductors, including Ag_2Se [389] and UO_2 [390].

Other interatomic potential instances not covered here include bonded potentials [391], Tersoff potentials [391], embedded atom model (EAM) potentials [391], and reactive force field [391]. In the end, the system under study and the level of accuracy required for the simulation, both determine the potential that is chosen.

2.7 Ewald Summation

In MD simulations, the inclusion of the Ewald summation technique is crucial for precise and computationally efficient calculation of long-range electrostatic interactions with periodic boundary conditions. Coulomb's law governs the electrostatic interactions among charged particles, representing a pairwise interaction that decays proportionally to the reciprocal of the distance between the particles. The interactions between charged particles in a periodic system extend beyond the nearest neighboring unit cells, resulting in an infinite number of interactions that can not be directly computed. This issue is resolved by Ewald summation technique, which separates the long-range electrostatic interactions into two parts: a short-

range component that is computed directly, and a long-range component that is calculated using Fourier transformations[364, 365]. The electrostatic potential by a group of point charges on a charged particle q_i is,

$$U_i|_{coul} = \frac{1}{4\pi\epsilon_0} \sum_n \sum_{j=1}^{N} (\frac{q_j}{\boldsymbol{r}_{ij} + nL}) \tag{2.22}$$

where L=(L_x, L_y and L_z) are the lattice vectors along the crystallographic direction. The sum covers all periodic pictures n and all particles j, with the exception of $j = i$ when $n = 0$ (exclusion of self-interaction). The total Coulombic contribution to the potential energy of an N-particle system is given by,

$$U_{Total}|_{coul} = \frac{1}{2} \sum_{i=1}^{N} q_i U_i|_{coul} \tag{2.23}$$

The above equation can not used to compute the electrostatic energy in a simulation, due to its poorly converging sum. To improve the convergence, the charge density is reformulated as a sum of δ-functions, leading to a modified expression for the electrostatic potential energy. In this approach, it is assumed that a Gaussian charge distribution of opposite sign surrounds the charged particle i with charge q_i, such that the overall charge of the cloud precisely cancels out q_i. However, the objective is to calculate point charge contributions, not screened charges. Therefore, each particle is accompanied by a compensating Gaussian charge (in reciprocal space) with the opposite sign to the screening charge cloud, for correcting the screening charge cloud effect. Thus the contribution to the electrostatic potential can be divided into three components.

1. One as a result of point charge q_i (Self term)
2. one as a result of the screening Gaussian charge cloud with charge $-q_i$ (U_{direct}).
3. The compensating charge cloud distribution with charge q_i ($U_{reciprocal}$)

The potential of the screened point charge exhibits a short-range nature and is calculated in real space. Fourier space calculations are utilized to determine the additional contribution from the compensating Gaussian charge. The contributions from each component can now be determined using the formula below.

The potential due to screened point charges, has a short-range character. The Gaussian charge distribution with width $\sqrt{2/\alpha}$ surrounding the ith charge particle

is represented as,

$$\rho(r) = q_j \ (\frac{\alpha}{\pi})^{\frac{3}{2}} \ \exp(-\alpha r^2) \tag{2.24}$$

Using Poisson's equation, the potential at a distance r from the center of this Gaussian charge distribution can be expressed as,

$$V_{gaussian} = \frac{-q_j}{r} erf(\sqrt{\alpha} r) \tag{2.25}$$

where,

$$erf(x) = \frac{2}{\sqrt{\pi}} \int_0^x e^{-u^2} du \tag{2.26}$$

2.7.1 Self Term

The self-interaction was overestimated when the compensating charge was calculated, so this correction term should be removed from the overall potential energy. The total self-correction term can be written as,

$$V_{self} = \sqrt{\frac{\alpha}{\pi}} \sum_{i=1}^{N} q_i^2 \tag{2.27}$$

2.7.2 Short range Potential(Real space)

The overall contribution of the screened point charge cloud due to a point charge q_i surrounded by a Gaussian charge distribution with net charge $-q_i$ can be expressed as

$$V_{direct} = \frac{1}{2} \sum_{i \neq j}^{N} q_j V_{screened} \tag{2.28}$$

where $V_{screened}$ is the potential due to screened point charge and can be written as,

$$V_{screened} = V_{point} + V_{Gaussian} \tag{2.29}$$

where V_{point} is the potential contribution from the point charge distribution. Thus,

$$V_{screened} = \frac{q_i}{r} - \frac{q_i}{r} erf(\sqrt{\alpha} r) = \frac{q_i}{r} erfc(\sqrt{\alpha} r) \tag{2.30}$$

where,

$$erfc(x) = 1 - erf(x) \tag{2.31}$$

where $erfc(x)$ is the complementary error function. Thus the total short-range contribution in real space can be represented as,

$$V_{direct} = \frac{1}{2}\sum_{i\neq j}^{N}\frac{q_i q_j}{r_{ij}} erfc(\sqrt{\alpha} r_{ij}) \tag{2.32}$$

2.7.3 Long Range Potential(Reciprocal/ Fourier Space)

As previously explained, the primary challenge is to determine the energy associated with a given charge distribution ($\rho(r)$). This involves solving Poisson's equation for the electrostatic potential, which is given by,

$$-\nabla^2\phi_r(r) = 4\pi\rho(r) \tag{2.33}$$

Where $\phi_r(r)$ is the potential in real space which can be obtained from the potential in k-space ($\phi_k(k)$) by doing the Fourier transformation as given below.

$$\phi_r(r) = \frac{1}{V}\sum_{k\neq 0}\phi_k(k)\exp(i\boldsymbol{k}.\boldsymbol{r}) \tag{2.34}$$

The charge distribution in Fourier space can be expressed as,

$$\rho_k(k) = \sum_{j=1}^{N} q_j \exp\left(-i\boldsymbol{k}.\boldsymbol{r}_j\right)\exp\left(\frac{k^2}{4\alpha}\right) \tag{2.35}$$

which is obtained by applying the Fourier transformation to the periodic sum of the combining Gaussian charge distribution in real space i.e., ($\rho_r(r)$). Following the Poisson equation in Fourier space, the potential for this charge distribution in Fourier space $\phi_k(k)$ can be obtained as,

$$\phi_k(k) = \frac{4\pi}{k^2}\sum_{j=1}^{N} q_j \exp\left(-i\boldsymbol{k}.\boldsymbol{r}_j\right)\exp\left(\frac{k^2}{4\alpha}\right) \tag{2.36}$$

Thus,

$$V_{reciprocal} = \frac{1}{2}\sum_i q_i\phi_r(r_i) = \frac{1}{2V}\sum_{k\neq 0}\frac{4\pi}{k^2}|\rho(k)|^2\exp\left(\frac{-k^2}{4\alpha}\right) \tag{2.37}$$

Hence, it becomes feasible to compute the total Coulombic contribution of the

system, to its potential energy as follows,

$$V_{coulomb} = \sqrt{\frac{\alpha}{\pi}} \sum_{i=1}^{N} q_i^2 + \frac{1}{2} \sum_{i \neq j}^{N} \frac{q_i q_j}{r_{ij}} erfc(\sqrt{\alpha} r_{ij}) + \frac{1}{2V} \sum_{k \neq 0} \frac{4\pi}{k^2} |\rho(k)|^2 \exp(\frac{-k^2}{4\alpha}) \quad (2.38)$$

2.8 Characteristics of various Ensembles

An ensemble average is essentially the mean value of a property over all possible states, that a system may inhabit within the scope of a specific ensemble or as permitted by the external conditions. In MD simulations the structural, dynamic, and thermodynamic properties of the system are estimated as the time average over the particle trajectory. However, by virtue of the "ergodic hypothesis", the time average tends to the ensemble average, provided the system is monitored over long enough periods of time. In MD simulations, a variety of ensembles are commonly employed, and the choice of ensemble depends on the specific properties of interest and the conditions under which the system is being studied. The microcanonical (NVE), canonical (NVT), and isothermal-isobaric (NPT) ensembles are some examples of these ensembles.

2.8.1 Microcanonical Ensemble (NVE)

The microcanonical ensemble (NVE ensemble), is a fundamental thermodynamic ensemble in molecular dynamics simulations, which is characterized by constant values for the number of particles (N), volume (V), and energy (E). The results for an NVE ensemble can be acquired by directly integrating the equation of motion through the procedures outlined in earlier sections. Equipartition theory states that each kinetic energy term in the Hamiltonian has an average energy of $\frac{1}{2}k_BT$, which is associated with each degree of freedom. A system with N atoms has $3N$ kinetic degrees of freedom, which are represented as $\frac{1}{2}m_iv_i^2$ in the kinetic energy (K) term in the Hamiltonian (H) and,

$$\begin{aligned} H &= \sum_{i<j}^{N} U(r_{ij}) + \frac{1}{2} \sum_{i=1}^{N} \frac{p_i^2}{m_i} \\ \implies H &= \sum_{i<j}^{N} U(r_{ij}) + \frac{1}{2} \sum_{i=1}^{N} m_i v_i^2 \end{aligned} \quad (2.39)$$

where p_i is the momentum of ith atom. Now the instantaneous kinetic energy of the system is,

$$\frac{1}{2}\sum_{i=1}^{N} m_i (v_i^{inst})^2 = \frac{3}{2} N k_B T_{inst} \implies T_{inst} = \frac{\sum_{i=1}^{N} m_i (v_i^{inst})^2}{3N k_B} \tag{2.40}$$

and the required temperatures at any MD step can be calculated as,

$$T_{req} = \frac{\sum_{i=1}^{N} m_i (v_i^{req})^2}{3N k_B} \tag{2.41}$$

The instantaneous temperature, denoted as T_{inst}, is likely to deviate from the required temperature. Therefore, to obtain the required temperature, T_{req}, the velocities of individual atoms are multiplied by the scaling factor (S_f). The scaling factor (S_f) can be described as,

$$S_f = \frac{v_i^{req}}{v_i^{inst}} = \sqrt{\frac{T_{req}}{T_{inst}}} \tag{2.42}$$

Thus the re-scaled velocity can be expressed as,

$$v_i^{req} = v_i^{inst} \sqrt{\frac{T_{req}}{T_{inst}}} \tag{2.43}$$

At the beginning of the run, when this technique is employed over a few hundred MD steps, the instantaneous temperature of the system is set to fluctuate around the target temperature, T_{req}. Typically, the scaling is performed, when it matches the criteria ($T_{inst} - \delta T \leq T_{req} \leq T_{inst} + \delta T$). After that, the system is given a few nanoseconds to settle without velocity scaling. When the instantaneous temperature and potential energy of the system stabilize to fluctuations around the mean, equilibrium is typically assumed. The run for the remaining time period, which is frequently referred to as the "production phase", is used to calculate thermodynamic averages, and trajectories are saved for a thorough analysis of structural and dynamical properties. To ensure the reliability of results, it is essential to maintain the conservation of energy and linear momentum.

2.8.2 Canonical Ensemble (NVT)

The NVT ensemble (wherein the number of particles, volume, and temperature of the system are kept constant) is frequently used in molecular dynamics to model

systems at a constant temperature. In NVT-MD simulations, thermostats are used to control the temperature of the system, by managing the thermal interaction between the simulated system and a heat bath. The implementation of the thermostat mechanism can take various approaches, such as combining Newtonian molecular dynamics with specific Monte Carlo moves or reformulating the Lagrangian equation of motion for the system. There are various thermostat models, such as the Nose-Hoover, Langevin, Andersen, and Berendsen thermostats.[364, 365] In the Andersen thermostat method for NVT-MD simulations, a constant temperature is maintained through stochastic collisions with a heat bath. In contrast, the Nosé thermostat approach relies on an extended Lagrangian, incorporating additional artificial coordinates and velocities to achieve constant temperature.

The Nose-Hoover thermostat [392] is an extension of the original Nose thermostat [392], incorporating a second variable referred to as the "thermostat variable" to regulate temperature. The extended Hamiltonian approach developed by Nose and Hoover can be represented as,

$$H_{NVT} = \sum_{i=1}^{N} \frac{p_i^2}{2m_i d^2} + U(r) + \frac{p_d^2}{2Q} + Lk_BT\log(d) \tag{2.44}$$

Where "d" is the additional coordinate in the Hamiltonian and "Q" is the effective mass associated to d, and $p_i = m_i d^2 r_i$, and $p_d = Q\dot{d}$. The variable "Q" determines the frequency at which the kinetic energy is transformed. The expression $Lk_BTln(d)$ is constructed with the "L" parameter set up in such a manner that the extended system possesses $2nN + 2$ degrees of freedom, where n is a spatial dimension, and 2 is added for d and p_d.

2.8.3 Isothermal-Isobaric Ensemble (NPT)

Instead of maintaining a constant volume, the majority of experiments are performed at constant pressure. In NPT-MD (where the number of particles, pressure, and temperature are kept constant), the cell volume is allowed to fluctuate to maintain a constant pressure. The equilibrium volume is achieved by balancing the internal pressure with the externally set pressure (P_{ext}). By adding an additional degree of freedom (V) linked with pressure (P_{ext}), the NVT-MD can be expanded to the

NPT-MD. The corresponding expanded Hamiltonian can be expressed as follows,

$$H_{NPT} = \sum_{i=1}^{N} \frac{p_i^2}{2m_i d^2} + U(r) + \frac{p_d^2}{2Q} + \frac{p_V^2}{2W} + gk_\beta T \log(d) + P_{ext}V \tag{2.45}$$

The kinetic components associated with the thermostat and barostat are in the third and fourth terms, respectively, while the potential energy associated with the thermostat and volume shift is in the last two terms. W is the mass parameter associated with the degree of freedom, V, and p_V is the momentum conjugate to V. In our studies, we employed NPT-MD simulation which are described in the subsequent chapters.

2.9 Basic Analysis

2.9.1 Radial Distribution Function

The calculation of the radial distribution function (RDF) bears similarity to the XRD technique employed in experiments for obtaining structural information. RDF is determined as the ratio of the local density ($n(r)$) to the global density (ρ) of atoms within the simulated system. It gives the idea of the spatial organization of an atom at a certain distance, r, from another tagged atom [364, 391]. The RDF between a set of atoms α and β, can be expressed as,

$$g_{\alpha\beta}(r) = \frac{V}{4\pi r^2 \delta r N_\alpha N_\beta} \sum_{k=0}^{N_\beta} n_k(r, \delta r) \tag{2.46}$$

where N_α and N_β are the overall numbers of α and β atoms, respectively, that make up the system, and V is the volume of the simulation box. In order to determine the RDF, the system is usually divided into small, concentric shells of radius r and thickness δr around a reference atom α, and the number of β atoms in each shell is counted, as shown in Figure 2.2. For crystalline solids, this function $g_{\alpha\beta}(r)$ consists of sharp peaks at every neighbor distance around a given atom and indicates the crystal structure of the system. As a solid melts or becomes amorphous, these peaks will broaden according to the changes in neighbor distances so that one can determine structural changes.

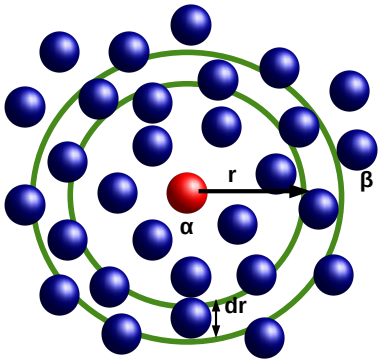

Figure 2.2: A schematic representation of the arrangement of α (red) and β (blue) atoms within the system for computing the radial distribution function,$g_{\alpha\beta}(r)$.

2.9.1.1 Running coordination number

By integrating $g_{\alpha\beta}$, it is possible to determine the number of atoms within the distance r from a tagged atom α, which is termed as running coordination number $C_{\alpha\beta}(r)$ and can be expressed as,

$$C_{\alpha\beta}(r) = \int_0^r g_{\alpha\beta}(r)\ 4\pi r^2 \delta r \tag{2.47}$$

The coordination number basically gives the number of neighboring atoms, around a central atom and reflects the local environment of a particle.

2.9.2 Mean square displacement

Mean square displacement (MSD) is one of the basic dynamic properties that defines the motion of the constituent atoms with time [364, 391]. Thus, the MSD can be expressed as,

$$\langle r_i(t)^2 \rangle = \frac{1}{N} \sum_{i=1}^{N} \langle [r_i(t+\tau) - r_i(\tau)]^2 \rangle \tag{2.48}$$

where $r_i(t)$ and $r_i(t+\tau)$ are the position vectors of i^{th} particle at time t and $t+\tau$. The angular bracket represents the statistical averaging. The self-diffusion coefficient, (D), can be extracted from MSD by using the Einstein relation i.e.,

$$\langle r_i(t)^2 \rangle = 6Dt + c \tag{2.49}$$

where c is the small thermal factor that arises from atomic vibration. D can be extracted from the slope of the MSD curve. Now the conductivity(σ) can be calculated from diffusion coefficient using the Nernst-Einstein equation,

$$\sigma = \frac{Dq_i^2 N}{H_r k_B T} \tag{2.50}$$

Where N is the number density of mobile atom. q_i is the charge of ion, T is Temperature, k_B is boltzman constant and H_r is Haven ratio. The diffusion process follows the Arrheneous equation, from which we can extract the activation energy E_a. The Arrheneous equation can be defined as,

$$\ln(D) = \frac{-E_a}{k_B T} + \ln A \tag{2.51}$$

where A is the pre-exponential factor. Thus the slope of $ln(D)$ against $1/T$ will give the activation energy (E_a).

2.9.3 Van Hove Correlation Functions

The van Hove correlation function describes how particles move over time and provides insights into the dynamic behavior of particles in a system. The van Hove correlation function, $G(r,t)$ is defined as the probability density of finding a particle at a time t, and at a distance r, from its initial position $r = 0$. The van Hove correlation function, $(G(r,t))$ is splited into two parts, i.e., self part of van Hove correlation function $(G_s(r,t)))$ of and distinct part of van Hove correlation function $(G_d(r,t))$.

1. Self part of van Hove correlation functions $(G_s(r,t)))$: It describes the probability density of finding a particle at a distance r from its initial position and can be defined as,

$$G_s(r,t) = \frac{1}{N}\sum_{i=1}^{N} \delta(r- \mid r_i(t) - r_i(0) \mid) \tag{2.52}$$

where $r_i(t)$ is the position vector of i^{th} particle at time t, N is the number of of particles, δ is the Dirac delta function. The integral of $G_s(r,t)$ over all space is unity and can be represented as,

$$\int_0^\infty 4\pi r^2 G_s(r,t)\, dr = 1 \tag{2.53}$$

The mean residence time of the atom is defined as the time at which around 50% of atoms jumped from their initial position ($r = 0$). Specifically, this corresponds to time, when the integrated area of the function $4\pi r^2 G_s(r,t)$ (upto the 1st neighbor distance) is equals 0.5.

2. Distinct part of van Hove correlation function ($G_d(r,t)$): It gives the probability density of finding a particle of type i at a distance r, from another another particle of type j, and can be defined as,

$$G_d(r,t) = \frac{1}{N(N-1)} \sum_{i=1}^{N} \sum_{j=1}^{N} \delta(r - \mid r_i(t) - r_j(0) \mid) \tag{2.54}$$

2.9.4 Spatial density distribution

Spatial density distribution is the three dimensional atomic density distribution over a volumetric space. It is calculated by splitting the entire volume into cubes and each cube is assigned with a quantity called atomic density of that particular location. The spatial density distribution is represented through $isosurfaces$ with a given atomic density value called $isovalue$. In crystalline solids, the spatial atomic density distribution is mainly used to visualize the diffusion pathways of the mobile species through the framework of the structure.

All of these analysis tools are utilized to analyse the structural and dynamic characteristics of ionic conductors discussed in the subsequent chapters of this thesis.

Chapter 3

Oxide Ion Transport In Yttria Doped Ceria

3.1 Introduction

The choice between ZrO_2 and CeO_2-based electrolytes depends on factors such as operational temperature, application requirements, and desired properties, like ZrO_2 favored for high-temperature stability and mechanical strength, while CeO_2 may be preferred for intermediate-temperature operation. However, YSZ exhibits high-enough ionic conductivity only above $1000°C$ for satisfactory SOFC operation [212, 276, 393–399]. This is one of the major drawbacks of this material, as the high operating temperature leads to deterioration of the chemical and mechanical stability of the interfaces while pairing with electrodes [400, 401]. The ceria-based electrolytes have the potential to address this issue due to their higher oxide ion conductivity permitting lower operational temperatures [402–409]. In fact, many popular cathode materials, such as $LaMnAO_3$ ($A = Co, Fe$ or Cr), are reported to be quite compatible with ceria-based electrolytes, whereas they were found to be reactive to zirconia-based electrolytes at high operating temperatures of around 1300 K [254, 410].

Unlike zirconia which undergoes several structural phase transitions, ceria retains the 'preferred' cubic (fluorite) structure across the entire range from room temperature to its melting point (above 2200 K) [411–414]. Thus, doping ceria with trivalent rare earth metals, such as Y^{3+}, Yb^{3+}, Sc^{3+}, Gd^{3+}, Sm^{3+}, Nd^{3+}, and La^{3+}, are being actively explored to further improve their oxide ion conductivity

The results based on this chapter is published: Madhual, S.; Kumar, P. P. J. Mater. Sci. **2023**, 58, 4499–4512.

while retaining the compatibility with electrode materials [254, 311, 312, 414–421]. As mentioned in Chapter 1, more and more states around the globe are investing heavily on the production of green hydrogen, arguably the most promising among sustainable alternatives to fossil fuels, we are witnessing a renewed interest in ceria based materials [293, 300, 422–427] for intermediate-temperature SOFCs.

Numerous experimental studies in the past have confirmed that with yttria doping, initially the ionic conductivity sharply increases, then starts dropping after reaching a maximum around $12 - 14\%$ of yttrium content [308, 414, 428–434]. Alongside, extensive investigations in the past couple of decades were also dedicated to improve and optimize these materials for SOFC applications [435–438]. Many atomistic computational studies in the past also have attempted to gain an understanding of the conduction mechanism of ceria doped with trivalent cations, some of which are highlighted in Chapter 1 [314, 439–448]. These studies have provided many fresh insight on the microscopic details of oxygen migration in the system. However, the nature of ionic conductivity variation with yttrium concentration still remains elusive [313, 316, 449–452], thus lacking in the much-desired recipe for material optimization.

This Chapter reports results based on our extensive molecular dynamics (MD) simulations on ceria over a wide range of yttrium doping. In the present work, simulations are carried out at a rather elevated temperature of 1300 K, only to enhance the ion transport in the system which improves the statistics of the data presented. The early part of the results discusses the gross macroscopic properties, such as variations in the structure and ionic conductivity with dopant concentration, and their agreement with previous experimental reports. Later, microscopic insights pertaining to the oxygen environments, migration channels, and microscopic energetics thereof, over a wide range of dopant concentrations are presented. We have critically analyzed the MD trajectories for the energy barriers as well as the contribution to the overall transport by the different channels connecting the distinct oxygen environments. This provides fresh insights on the observed nature of oxide ion transport in the matrix.

3.2 Simulation Details

Isothermal-isobaric ensemble (NPT) molecular dynamics (MD) simulations of the cubic (fluorite) phase of the yttriya doped ceria (YDC), $Y_xCe_{1-x}O_{2-x/2}$, are carried out at 1300 K. The starting structure of YDC is generated from the room

temperature X-Ray structure by McBride *et al.*, with initial unit cell parameters, $a = b = c = 5.411$ Å and $\alpha = \beta = \gamma = 90^0$ [295, 453–456]. The simulation cell is constructed from $6 \times 6 \times 6$ cubic unit cells. Thus the un-doped system, *pure* CeO_2, consists of a total of 2592 ions (864 Ce^{4+} and 1728 O^{2-} ions). The Y^{3+} dopants are introduced randomly at the Ce^{4+} locations in the simulation cell. For every x mole percent, half the corresponding number of oxygens are removed from the simulation cell at random. It may be noted that marginal amounts of additional oxygen vacancies could be present in the experimental samples due to defects or variations in oxygen partial pressure, the effects of which are not included in the present study. The ions are assumed to follow the Born-Mayer interaction [457],

$$V_{ij} = \frac{1}{4\pi\epsilon_0}\frac{q_i q_j}{r_{ij}} + A_{ij}exp(\frac{-r_{ij}}{\rho_{ij}}) - \frac{C_{ij}}{r_{ij}^6} \tag{3.1}$$

where q_i, q_j are respectively the *formal* charges of the i^{th} and j^{th} species, separated by a distance r_{ij}. A_{ij} controls the strength of the short-range repulsion between the species, while ρ_{ij} dictates the range of interaction. C_{ij} represents the Van der Waals attraction between the species. The parameters of the potential are taken from previous studies [270, 458], and listed in Table 3.1. The cation-cation interaction are assumed to be purely Coulombic in nature. Ewald summation technique is used to ensure the convergence of the long-range Coulombic interactions [364] in the system.

The NPT-MD simulations are carried out for 25 ns at a time step of 2 fs, after dedicating an initial 4 ns for the equilibration of the system. The calculations are carried out over the dopant (yttrium) concentrations of 4 to 40 $mol\%$ at 1300 K, using LAMMPS package [459]. The trajectories stored at intervals of 500 MD steps are analyzed for structural, dynamical and thermodynamic properties of the system, using in-house analysis codes.

Pairs	A_{ij} (eV)	ρ_{ij} (Å)	C_{ij} ($eV Å^6$)
Ce – O	1017.4	0.3949	0
Y – O	1345.1	0.3491	0
O – O	22764.3	0.1490	27.88

Table 3.1: Parameters of the Born-Mayer potential employed in the present simulation [270, 458]. Coulombic interactions are calculated using formal charges on ions.

3.3 Results and discussion

3.3.1 Structure

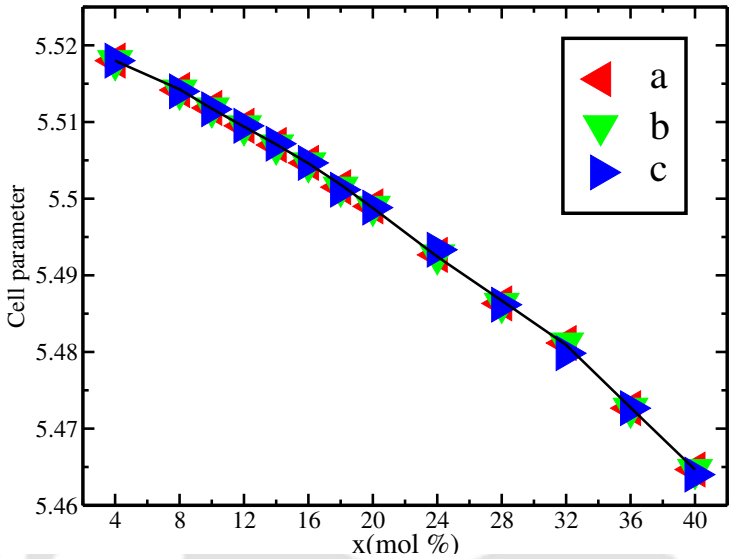

Figure 3.1: Variation of cell parameters in YDC, $Y_xCe_{1-x}O_{2-x/2}$, for concentration, x ranging from $4-40$ $mol\%$, from 25 ns long NPT-MD simulations at 1300 K.

The time-averaged lattice parameters of YDC, $Y_xCe_{1-x}O_{2-x/2}$, over dopant concentrations of 4 to 40 $mol\%$, from NPT-MD simulations at 1300 K are shown in Figure 3.1. The cell angles (not shown) are within 0.01% of the expected cubic cell. A regular decrease in the cell parameters with dopant concentration is observed, though this is rather marginal amounting only to 2% of change across the range. The observed behavior is in good agreement with previous experimental reports [295, 301, 429, 454, 460]. Certain other rare-earth-doped ceria, for instance, Yb doped ceria, show a similar trend [461]. In contrast, other dopants, such as La, Gd, and Sm, produce an enlargement in the lattice parameters with concentration [326, 419, 462–467].

The radial distribution functions (RDF) is defined as,

$$g_{\alpha\beta}(r) = \frac{n_\beta(r)}{\rho_\beta \; 4\pi r^2 \delta r} \tag{3.2}$$

where $n_\beta(r)$ is the average number of atoms of species β in a thin spherical shell of radius r and thickness δr, with respect to the reference species α, and ρ_β is the average number density of β species.

Presented in Figure 3.2, are the radial distribution functions (RDFs) between

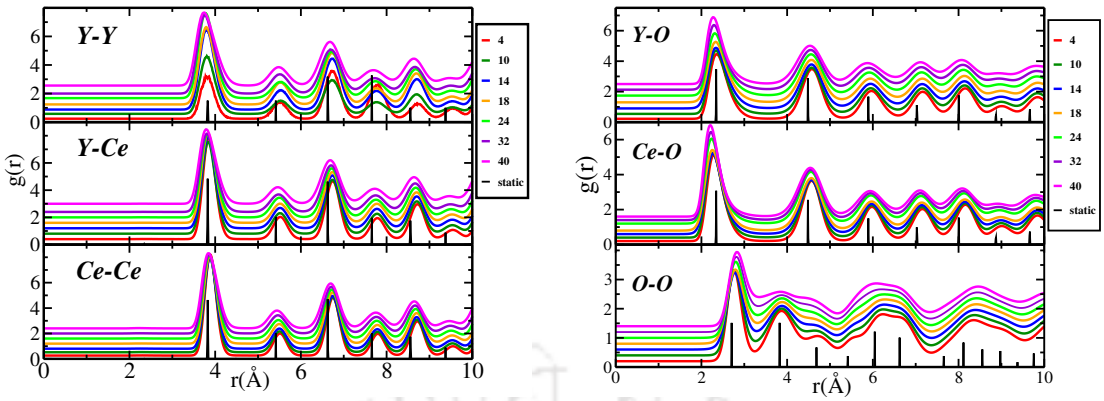

Figure 3.2: *Left panel*: The radial distribution functions (RDFs), $g(r)$ s, between cations, Y-Y, Ce-Y, Ce-Ce, of yttria doped ceria (YDC), $Y_xCe_{1-x}O_{2-x/2}$, for dopant concentrations, x, ranging from $4-40$ $mol\%$ from 25 ns NPT-MD simulations at 1300 K. *Right panel*: The corresponding RDFs between cation-oxygens, Y-O, Ce-O, and oxygen-oxygen, O-O. The vertical bars in all the graphs are the corresponding $g(r)$ s (with rescaled intensities) calculated from the X-ray structure of the un-doped system [454]. All the RDF s from the MD simulations are displaced uniformly along Y-axis for clarity.

Pairs	Neighbour distance (Å)
Ce – O	2.24
Y – O	2.41
O – O	2.83
M – M	3.62–3.64

Table 3.2: The average first neighbor distances between select ion pairs from NPT-MD simulation at 1300 K. M represents the framework cations, Ce^{4+} or Y^{+3}, of the system.

various ion pairs, averaged over MD trajectory at 1300 K, for a few select dopant compositions of YDC, $Y_xCe_{1-x}O_{2-x/2}$. Among other microscopic information, the RDFs are sensitive to the crystal structure of the material. For instance, in Figure 3.2 the locations of the peaks in the 'dynamic' RDFs of the system at 1300 K are in agreement with the corresponding distances for the ideal fluorite structure (shown as bars), thus asserting the structural integrity of the simulated system. Apart from the thermal broadening, the cation-cation peaks in the left panel, are shifted to slightly longer distances (more prominently seen for the distant ones) with respect to the corresponding 'static', X-ray positions, due to thermal expansion. However, the peaks shift to slightly lower values with dopant concentration which is consistent with the observed decrease in lattice parameters. The slightly smaller ionic radii of the yttrium ions as well as their lower charge, causes an overall reduced cation-cation repulsion in the matrix, could be responsible for the observed decrease in the

lattice parameters.

The cation-oxygen distances (shown in the right panel of Figure 3.2) also follow the decreasing trend with dopant concentration. However, a relatively more pronounced increase is observed in the oxygen-oxygen distance despite the decrease in lattice parameters with doping. This is suggestive of some degree of disorder of the oxygen sublattice. The slight broadening of the oxygen-oxygen RDFs also reflects this increasing disorder with dopant concentration. The average nearest neighbor distances, deduced from the first peak of the RDFs, at 1300 K are listed in Table 3.2. These are in good agreement with previous studies [313, 316, 451, 468].

3.3.2 Ion transport

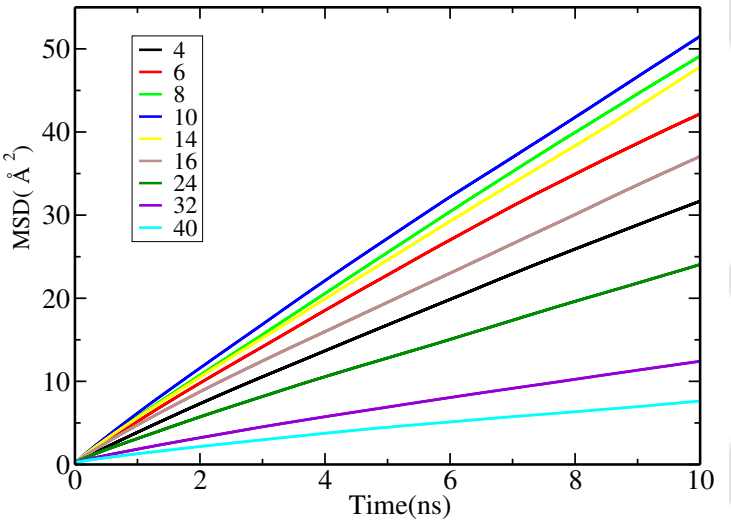

Figure 3.3: Mean square displacement of oxygens ions in YDC, $Y_xCe_{1-x}O_{2-x/2}$, for concentrations, x, ranging over $4-40$ $mol\%$, from 25 ns long NPT-MD simulation at 1300 K.

The mean-squared displacement (MSD) of ions with time is one of the dynamic quantities of interest. The quantity is defined as,

$$R^{\alpha}(t)^2 =< [\mathbf{r_i}^{\alpha}(t+\tau) - \mathbf{r_i}^{\alpha}(\tau)]^2 > \tag{3.3}$$

where $\mathbf{r}_i^{\alpha}(t)$ is the position vector of the i^{th} ion of species α at any instant of time, t. The angular brackets indicate the statistical averaging, wherein the function is averaged over the stored MD trajectory of the species in the system, and for numerous time origins τ. The MSD allows to estimate the self-diffusion coefficients

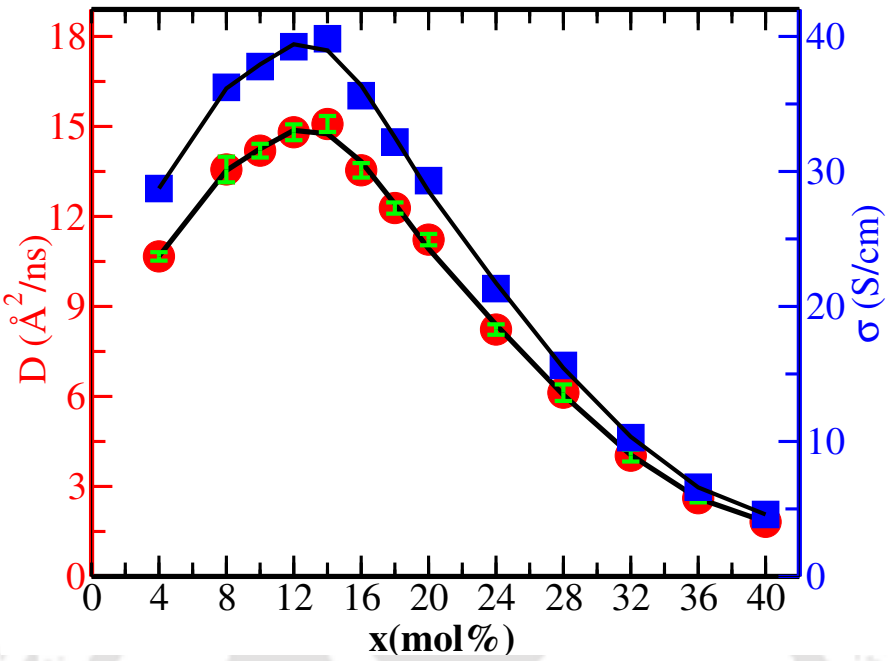

Figure 3.4: The self-diffusivity of oxygen ions (red) and the corresponding ionic conductivity (blue) in yttria doped ceria (YDC), $Y_xCe_{1-x}O_{2-x/2}$, for concentrations, x ranging over $4-40$ $mol\%$, at 1300 K. The error bars for the self-diffusivity are calculated using block averages [365]. The black lines are only to guide the eye.

of different species by virtue of the Einstein relation,

$$D^{\alpha} = \lim_{t \to \infty} \frac{R^{\alpha}(t)^2}{6t} \tag{3.4}$$

The MSD of oxygen ions at 1300 K calculated over a wide range of compositions, 4 to 40 $mol\%$, are shown in Figure 3.3. As expected, the framework cations, Ce^{4+} and Y^{3+}, do not show any self-diffusivity, with their MSDs remaining flat in time (thus, not shown), for the entire range of doping examined.

The ionic conductivity of YDC due the oxygen transport are estimated using the Nernst-Einstein relation,

$$\sigma = \frac{n\, q_0^2\, D}{k_B\, T} \tag{3.5}$$

where q_0 is the formal charge of the oxygen and n is the number density of the species in the system for the respective dopant concentration. T is the temperature of the system simulated and k_B the Boltzmann constant. The self-diffusivity of oxygens ions and the ionic conductivity of YDC, $Y_xCe_{1-x}O_{2-x/2}$, at 1300 K are shown in Figure 3.4, for the entire dopant concentration range of $x = 4$ to 40 $mol\%$. The highest oxygen diffusivity as well as ionic conductivity thereof is observed around

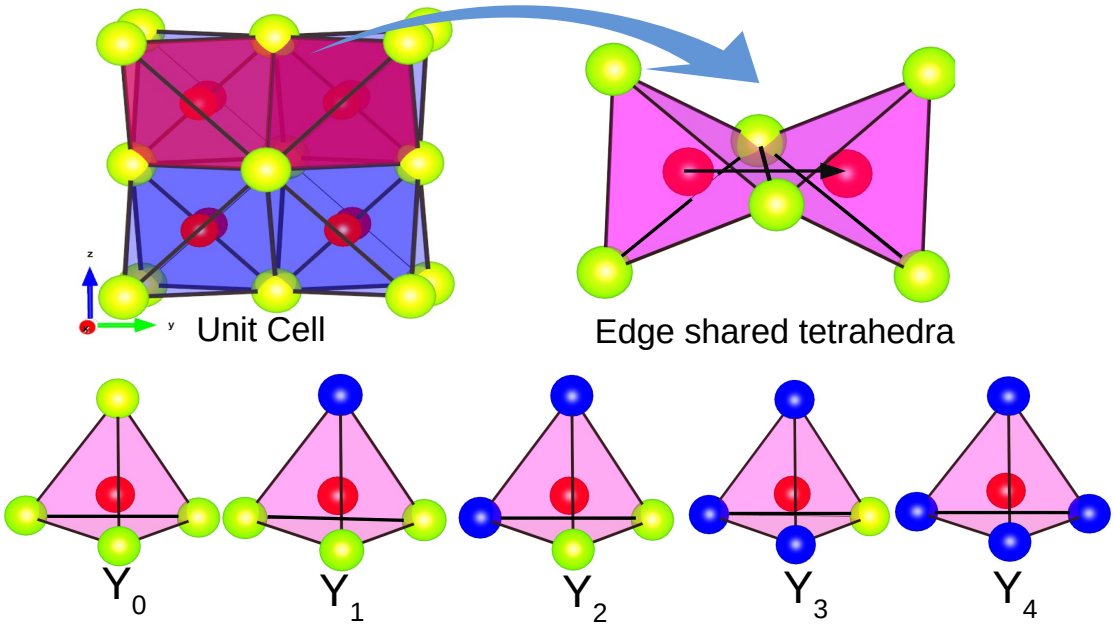

Figure 3.5: Different possible oxygen environments in $Y_xCe_{1-x}O_{2-x/2}$, based on the surrounding cation organization is demonstrated. On the top left, the cubic unit cell of $Y_xCe_{1-x}O_{2-x/2}$, with oxygen sites (red) located at the tetrahedral holes of the *fcc* sub-lattice of the cations, Ce^{4+} (green) and Y^{3+} (blue), is shown. In the remaining figures, labelled Y_0 to Y_4, the different oxygen environments are classified based on the number of Y^{3+}-ion occupying the corners of the tetrahedra. Use of the "ball-stick" model is only for the ease of visualization.

$x = 14\ mol\%$ which is in good agreement with previous experimental [431, 433, 469] and simulation studies [254, 316, 414, 470].

3.3.3 Microscopic insights

The fluorite structure of YDC has the cations forming an *fcc* sub-lattice with the oxygen residing at the tetrahedral holes. In other words, the oxygen sites are at the center of a tetrahedron with Ce^{4+} or Y^{3+} forming its four corners. Figure 3.5(a) depicts the edge-shared tetrahedral holes embedded in the *fcc* sub-lattice, and the possible five different oxygen environments, depending on the number of Y^{3+} ions forming the corners of the tetrahedra. We name these oxygen environments Y_m, where $m = 0, 1, 2, 3$ or 4, indicating the number of Y^{3+} corners in the tetrahedron. Shown in Figure 3.6 is the spatial distribution of oxygen density over two unit cells for a few iso-density values. As evident from the blue contour of low iso-density values in Figure 3.6, the oxygen migration channel connecting neighboring sites are parallel to the crystallographic axes and bisects the tetrahedral edges formed by the cations.

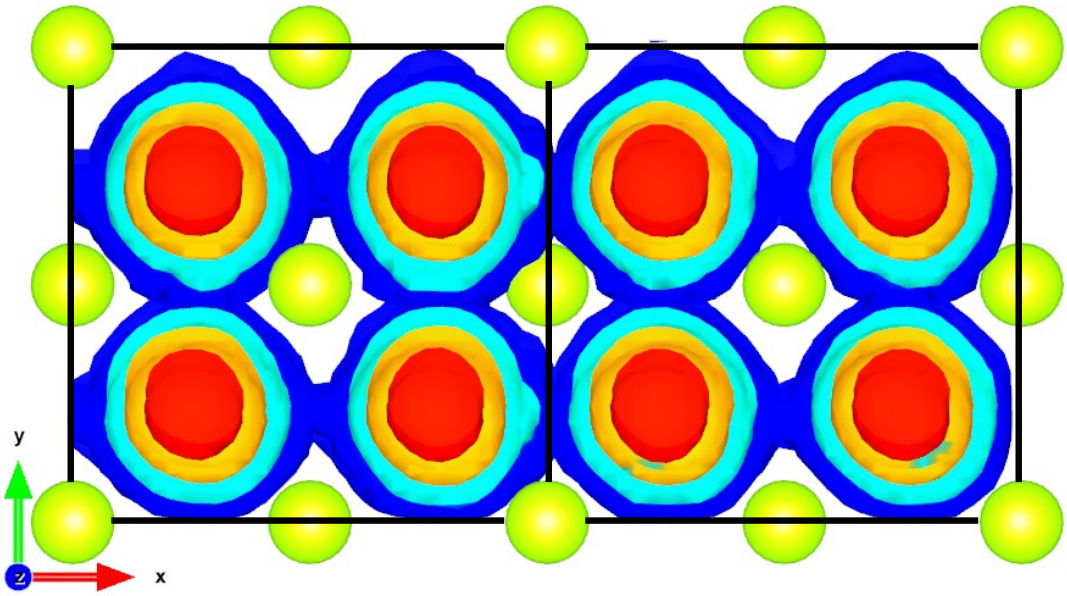

Figure 3.6: Spacial distribution of oxygens over two unit cells are shown for a few iso-density values (increasing from blue to red) in the fluorite structured YDC, $Y_xCe_{1-x}O_{2-x/2}$, (for $x = 14\ mol\%$ from present MD simulations at 1300 K). The balls in green colors indicate the cation sites, which may be occupied by the Ce^{4+} or Y^{3+} ions.

This is consistent with some of the earlier simulation studies [273, 277, 278, 471]. In the later discussion, we shall explore the energetics of the individual oxygen sites, the barriers for ion hops between different environments, etc. for better insights on the nature of oxygen migration in the system.

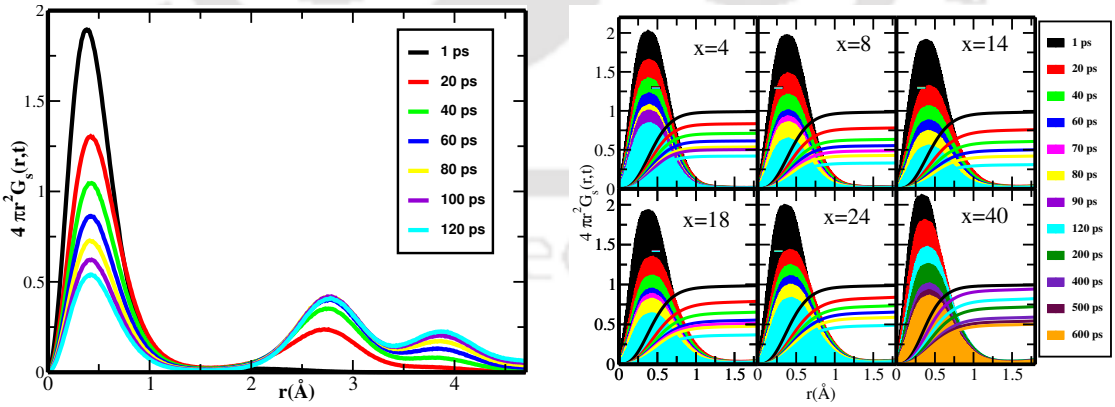

Figure 3.7: *Left panel:* The nature of the diffusion profile of oxygen ions demonstrated for the highest conducting $x = 14\,mol\%$. *Right panel:* The first peaks of the diffusion profiles (shaded plots) for a few select compositions at select timescales, and their respective cumulative area (continuous lines) over half the neighbor distance converging to 0.5.

The timescale of ion hops between neighboring sites are examined utilizing the

self-part of the van Hove correlation function given by,

$$G_s(r,t) = \frac{1}{N}\sum_{i=1}^{N}\delta(r- \mid r_i(t) - r_i(0) \mid) \tag{3.6}$$

where $r_i(t)$ is the position vector of i^{th} particle at time t, N is the number of oxygen ions, δ is the Dirac delta function. The integral of $G_s(r,t)$ over all space is unity, that is,

$$\int_0^\infty 4\pi r^2 G_s(r,t)\, dr = 1 \tag{3.7}$$

As the first peak of the $4\pi r^2 G_s(r,t)$ in Figure 3.7 suggests, for a short duration the oxygen ions are confined in their sites, oscillating about their mean position at an *average* amplitude of around 0.5 Å. At longer timescales, the ions hop to the nearest vacant site resulting in the second peak around 2.8 Å. And at even longer timescales the ion hops off to subsequent sites producing further peaks, as seen for $t \geq 40ps$, for instance. The mean residence time, τ, of the ion is estimated as the duration by which approximately 50% of particles hop off from their original location, that is, when the area under the first peak (up to $r = 1.5$ Å) of the function, $4\pi r^2 G_s(r,t)$, is 0.5. The values estimated suggest significant variation across the composition range, with the lowest value of $\tau = 60\,ps$ noted for the best conducting $x = 14\,mol\%$. The 'rough' estimates of the self-diffusivity could also be deduced from the residence time, τ, following, $D^\tau = d^2/6\tau$, where d is the separation between neighboring oxygen sites. As seen in Figure 3.8 the D^τ variation is in qualitative agreement with the self-diffusivity D^α (reproduced from Figure 3.4), calculated more precisely from the mean squared displacement. The fact that the nature of the self-diffusivity follows the inverse of the residence time re-confirms that the transport mechanism involves discrete ion hops through neighboring sites, as opposed to incremental advancements leading to a unimodal diffusion profile observed in fluids.

It shall be noted that the interaction energy of an oxygen ion with the rest of the system is given by,

$$u_i = \sum_{j=1,\, i\neq j}^{N} V_{ij} \tag{3.8}$$

where N is the total number of particles in the system, and V_{ij} is the interaction potential in eq 3.1.

Figure 3.9(top panel) shows the MD averaged potential energy of the oxygen ions (in absolute scale), occupying the various oxygen sites, Y_0 to Y_4. It shall be noted that these 'site-energies' of the oxygen decreases monotonically with composition.

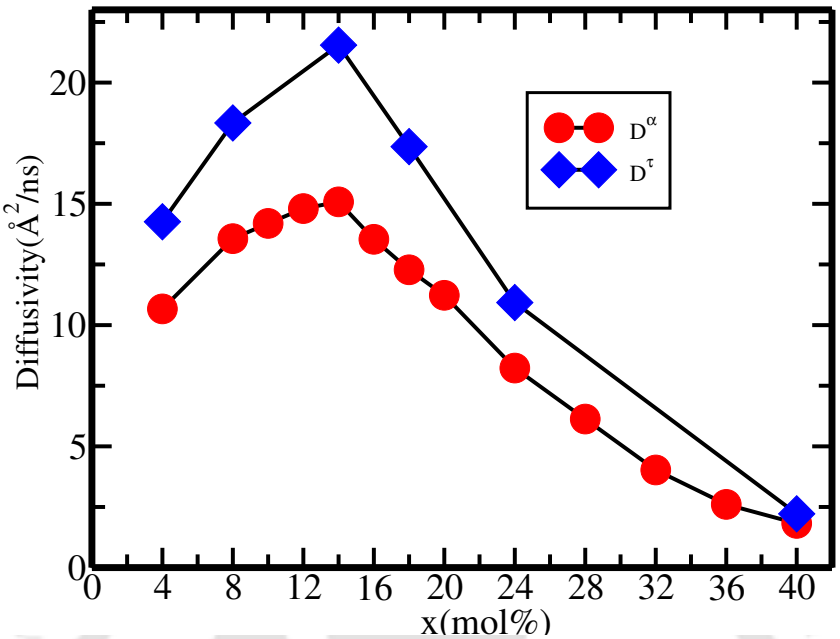

Figure 3.8: Comparison of self-diffusivity D^{τ} estimated from the average residence time of oxygen, with that calculated from the mean-squared displacement D^{α} .

More importantly, for a given composition the site energies are found to increase from Y_0 to Y_4, irrespective of the composition. The incremental energetic cost between 'successive' sites, that is, $\Delta E = E(Y_{i+1}) - E(Y_i)$, where $i = 0$ to 3, is sensitive to the site indices, but weakly on the dopant concentration. The approximate values for, ΔE are 0.10 eV, 0.14 eV, 0.18 eV, 0.22 eV, respectively between $Y_1 - Y_0$, $Y_2 - Y_1$, $Y_3 - Y_2$, and $Y_4 - Y_3$. Thus for every Y^{3+} in its local tetrahedral environment comes with energetic cost for the oxygen ion, and lower probabilistic occupancy as dictated by the Boltzmann factor. This increase in energy is attributed to the weaker Coulombic interaction between the O^{2-} ions with Y^{3+}, compared to Ce^{4+} ions.

The bottom panel of Figure 3.9 presents the statistics of Y_0 to Y_4 sites present in the matrix across the dopant concentration. It shall be noted in passing that since there is no cationic diffusion in the system the starting cationic distribution, based on the *random-* assignments of Y^{3+} and Ce^{4+} on the *fcc* sub-lattice, remains throughout the simulation. It is noted that the percentage of Y_0 sites of lowest energies decreases monotonically with the composition while that of the higher energy sites, Y_2 to Y_4, increases in the matrix. The percentage of Y_1 sites of moderate energy shows a broad plateau for intermediate compositions before starting to fall. While the creation of oxygen vacancies, progressively with the dopant concentration, promotes

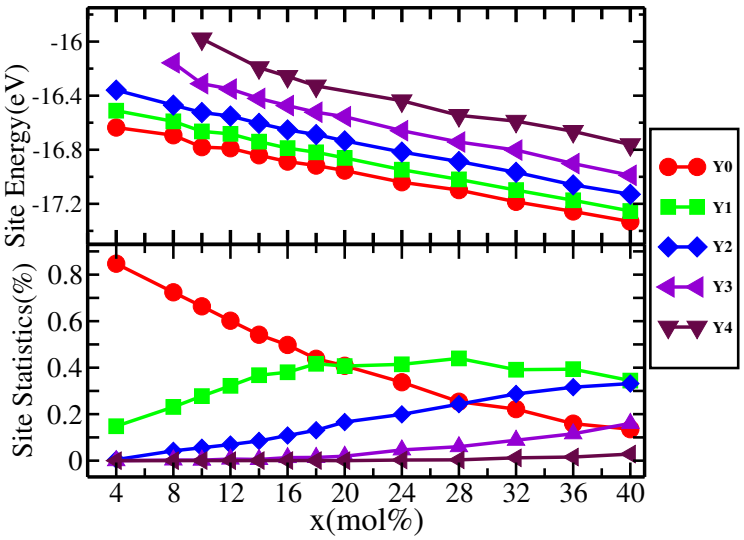

Figure 3.9: *Top panel*: Site energy of oxygens in different cationic environments, Y_m, where $m = 0, 1, ...4$, across the composition range, 4 to 40 $mol\%$ of $Y_xCe_{1-x}O_{2-x/2}$ are shown. *Bottom panel*: Statistics of the Y_m sites in the matrix are shown over the concentration range.

ion transport in the system, the subsequent increase in the number of higher energy sites (of lower probabilistic occupancy) in the matrix hampers the prospect. Thus the variation in conductivity producing a maximum at intermediate composition can be qualitatively understood as a result of these two competing aspects.

For better insights on the nature of ion migration, various channels connecting the distinct oxygen environments (as discussed in the context of Figure 3.6) are examined in greater detail. Of particular interest are the energy barriers encountered by the oxide ions during the hops, which are estimated from the individual potential energy of oxide ions (u_i's as defined by equation 3.8) calculated during the simulation. Figure 3.10 presents the potential energy profiles calculated along distinct channels, labeled $Y_i - Y_j$, where $i, j = 0, 1, 2, 3$ or 4, for a few selected compositions, $x = 4, 14, 28$ and 40 $mol\,\%$ of $Y_xCe_{1-x}O_{2-x/2}$. The statistics of the number of individual channels in the matrix as well as an estimate of the ion traffic along these channels are also reported. These are averaged over the entire 25 ns MD trajectories at 1300 K. The profiles are with reference to the average energy of the ions at the Y_0 sites of the respective composition. It shall be noted that since adjacent tetrahedral oxygen sites share a common cationic edge, not all distinct permutations of channels are possible, limiting the total number to a maximum of twelve. Further, out of these possible channels, those having less than 0.5% of traffic are left out of Figure 3.10 due to poor statistics. The following is the description of the strategy

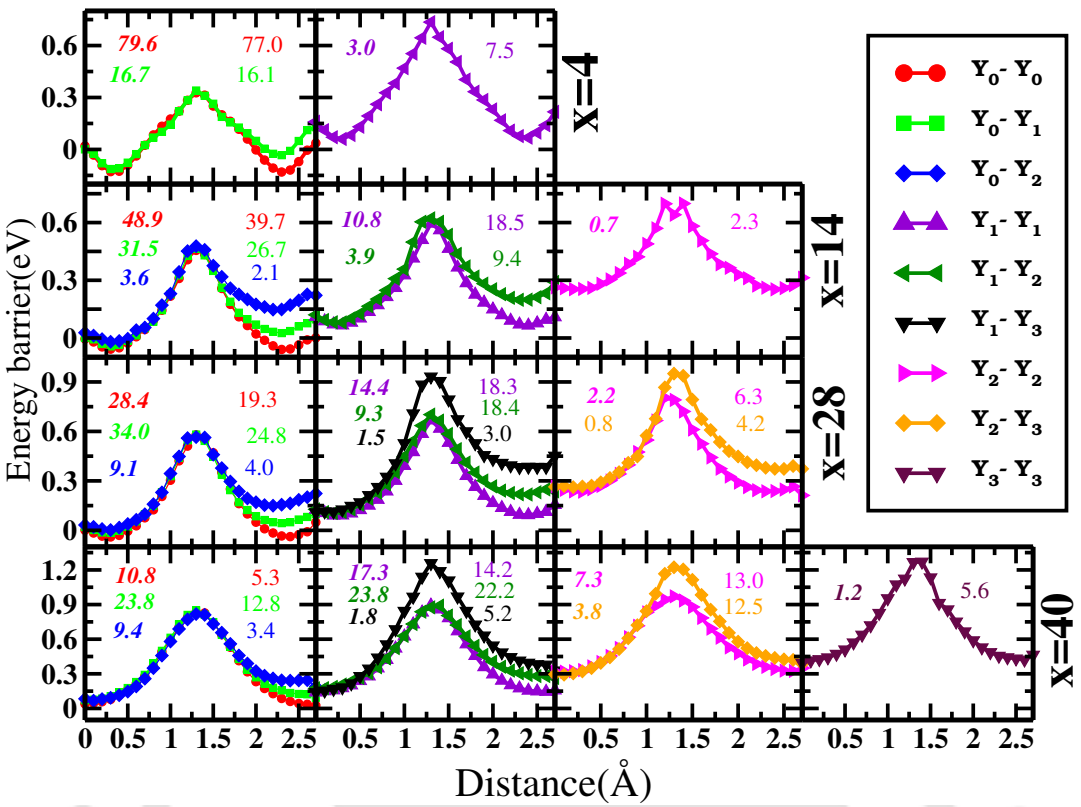

Figure 3.10: Energy profiles of oxygen ions along possible channels connecting the different oxygen sites are shown, for the few select compositions, $x = 4, 14, 28$ and 40 $mol\,\%$ of $Y_xCe_{1-x}O_{2-x/2}$, from NPT-MD simulation at 1300 K. All the energies are relative to the energy of the Y_0 site of the respective composition. The legends are common to all the plots. Marked with the same color, the numbers on the left side of each panel are the estimated traffic through the corresponding channel (in %), and the numbers on right give the percentage of the actual number of channels present in the matrix for a given composition. Channels having less than 0.5% of traffic are not shown. See text for details.

used in this calculation: during the trajectory analysis, every of the oxygen ions are located between *two of its nearest* individual oxygen sites say, O_l and O_m, where l and m could be any of the 1728 oxygen sites in the simulation cell comprising of $6\times6\times6$ unit cells. The channel is then identified as $Y_i - Y_j$ (where, i or j could be 0 to 4) based on the environments of O_l and O_m, and sorted following the convention that $i \leq j$. Now, the position vector of the ion with respect to O_l or O_m (following the above convention) is projected onto the vector connecting these two sites (O_l and O_m), and the individual energy of the ions (as defined by 3.8) are cumulated in linear bins along the respective projected distances. The bins are then averaged over the entire trajectory. It shall however be noted that the actual direction of ion hops, that is, from left to right or opposite, in time is not accounted for. The populations in the three *central* bins, normalized over all the different possible channels, are used

to estimate the percentage of traffic. Periodic boundary conditions are invoked for all vectors and distance measures involved in the above calculations.

It shall be noted in Figure 3.10 that all energy profiles peak at a distance of around 1.4 Å, at the mid-point of the two neighboring oxygen sites. The channels originating from Y_0 exhibits the lowest barrier for all compositions. The small dips observed in the barrier profiles of lower concentrations ($x = 4$, 14 $mol\%$, etc.) suggests that oxygen ions are assuming off-centered locations with respect to their ideal crystallographic positions. This is possibly due to the stronger repulsion between the neighboring oxygens, in a relatively 'crowded' matrix. This proposal is in agreement with the observed systematic reduction in the site energies with concentration (shown in 3.9), despite the fact that trivalent yttrium replacing the tetravalent cerium reduces the overall attractive contribution to the potential energy of the system. The barrier heights are increasing systematically with the increase in yttrium presence at the destination site, that is, with index j of $Y_i - Y_j$-channel originating from a given site of index i. The barriers of individual channels are also increasing with yttrium concentration, that is, down the column. As a consequence of the increase in the high indexed sites in the matrix (as seen in 3.9), the percentage of higher indexed channels increases with composition, at the expense of lower indexed ones. Also, these channels gradually start accounting for larger fractions of the overall transport in the system, despite the higher energy barriers they pose. Thus, the initial advantage due to the availability of lower-indexed, low-barrier, channels at lower concentrations ($\leq 14\%$) slowly fades away as the percentage of higher-barrier channels increases in the system, resulting in a monotonic drop in the mobility of oxygen ions.

Figure 3.11 presents the *statistically averaged* barrier profiles of the oxygen migration for a few select dopant compositions. Note that this essentially means that the profiles are averaged over the entire trajectory disregarding the details of the tetrahedral environments. The barriers are found to be sensitive to the composition, measuring a minimum of about 0.5 eV, for the highest conducting, $x = 14$ $mol\%$. Also, no signatures of appreciable oxygen-oxygen correlation is observed in the present study, though evidence for the same was noted YSZ, as well as in the earlier studies of Sm and Pr doped ceria [314, 472] and Sr doped $LaMnO_3$ [473]. It shall be noted in passing that earlier theoretical studies on alkali ion conducting solids also have proposed that an optimal degree ion-ion correlation can be one of the key factors for enhancing ion transport [474–476]. The variation of the microscopic energy barriers observed in the present study are in qualitative agreement with the activa-

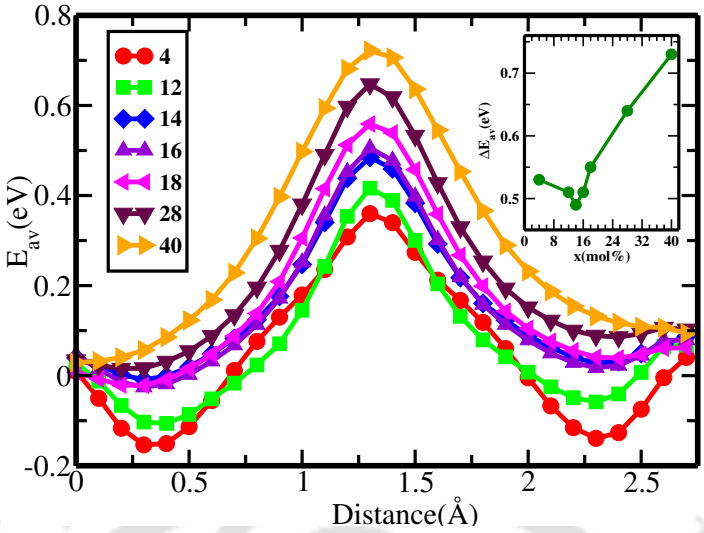

Figure 3.11: The average microscopic energy profiles, E_{av}, for oxygen hops calculated along the diffusion pathway at 1300 K for dopant concentration $x = 4, 12, 14, 16, 18, 28$ and 40 $mol\%$. The inset shows the energy barriers ΔE_{av}, calculated as the difference of maximum to minimum energy values for the respective composition.

tion energies reported in previous experimental studies [306, 307, 414, 429, 477, 478]. Thus, the nature of the conductivity variation of YDC with composition (Figure 3.4) follows the changes in the microscopic energy barriers.

3.4 Summary and Conclusions

The microscopic nature of the oxide transport in yttria doped ceria ($Y_xCe_{1-x}O_{2-x/2}$), is investigated by employing extensive molecular dynamics simulations in the isothermal-isobaric ensemble, over the range, $x = 4$ to 40 $mol\%$, at 1300 K. The cell parameters of the cubic (fluorite) YDC decreases monotonically with the yttrium concentration, in agreement with previous experimental reports. The microstructure examined utilizing the radial distribution functions (RDFs) suggest that the smaller ionic radii of Y^{3+} ions, combined with their lower charge in comparison with Ce^{4+}, results in a weaker cation-cation repulsion causing the decrease in lattice parameters.

The self-diffusivity of oxygen ions, as well as the ionic conductivity of the system, exhibits a maximum around 14 $mol\%$ of yttrium doping at 1300 K, which is in agreement with most previous experimental and theoretical investigations. The nature of this variation is consistent with the respective residence times of oxygens estimated from the van Hove correlation function. The oxygen migration channel connecting neighboring sites are found to be parallel to the crystallographic axes.

This is in agreement with the migration channels identified in the fluorite-structured yttria-stabilized zirconia as well.

It is noted that the individual potential energies of oxygen ions at their crystallographic sites increase with the number of yttrium ions in the neighborhood. A systematic analysis of the traffic of ions and the microscopic energy profiles, resolved along the distinct channels connecting the different oxygen environments, are carried out. The results suggest that the presence of yttrium in the environment not only increases the energy of the oxygen at the sites, but also the energy barriers in the channels connecting such sites. Thus, the optimal conductivity observed around 14% of yttria doping can be qualitatively understood in terms of two competing factors, that is, while the oxygen vacancy creation promotes ion hops between neighboring sites at lower concentrations, the increase in the fraction of higher-barrier channels in the matrix starts hampering the transport on further yttrium doping. In fact, the statistically averaged microscopic energy barriers for the oxygen migration produced a pronounced minimum for the highest conducting composition, namely, $x = 14\,mol\%$ of yttrium doping. Thus, the observed conductivity variation can be satisfactorily explained in terms of the microscopic energy barriers.

Chapter 4

Oxide Ion Transport In Yttria Stabilized Zirconia

4.1 Introduction

As explained in Chapter 1, zirconia-based materials are preferred for electrolyte materials in SOFCs due to their high oxygen-ion conductivity, thermal and chemical stability at elevated temperatures, and versatility with various fuel types [65, 89, 177, 479–483]. Among the different zirconia-based electrolytes, fluorite-structured (cubic) yttria-stabilized zirconia (YSZ), $Y_xZr_{1-x}O_{2-x/2}$ (where x is typically in the range of 4 to 40 $mol\%$ mole percentage), have gained better attention due to their high oxygen ion conductivity above 1000 K. In the fluorite structure of YSZ, the cations occupy the fcc position, and the anions mostly occupy the tetrahedral position. When doped with Y_2O_3, the trivalent Y^{3+} cations partially replace tetravalent Zr^{4+} leading to the creation of oxygen vacancies. The mobile oxygen ions migrate through these vacancies, resulting in appreciable ionic conductivity at high temperatures. Numerous previous experimental studies have concluded that the trend of increasing conductivity with increasing Y^{3+} dopant concentration follows up to the range of $8 - 12$ mol%, after which the conductivity decreases [212, 276, 393–396, 398, 484–486].

The computational study in this chapter aims to provide better insights into the microscopics of ion transport mechanisms and energy barriers in YSZ, exploiting the molecular dynamics (MD) technique. It shall be noted that many computational

The results based on this chapter is published: Madhual, S.; Pramanik, K.; Kumar, P. P. Phys. Chem. Chem. Phys. **2022**, 24, 18281–18290.

studies in the past have been dedicated to this pursuit, and with a certain degree of success [273, 274, 471, 487, 488, 488–494]. Some of these studies are addressed in Chapter 1, and some of them shall be highlighted in the later sections while making critical comparisons with the results from the present investigation.

4.2 Simulation Details

The classical MD simulation on YSZ are carried out in the isobaric-isothermal (NPT) over the temperature range of 800 K to 2200 K using LAMMPS package [459]. The interaction between the ions are assumed to be of the Born-Mayer form, [457]

$$V_{ij} = \frac{1}{4\pi\epsilon_0}\frac{q_i q_j}{r_{ij}} + A_{ij}exp(\frac{-r_{ij}}{\rho_{ij}}) - \frac{C_{ij}}{r_{ij}^6} \tag{4.1}$$

where q_i, q_j are the charges of the i^{th} and j^{th} species respectively, and r_{ij} the separation between them. A_{ij} controls the strength, while ρ_{ij} determines the range of the short-range repulsion between i^{th} and j^{th} ions. The C_{ij} appearing in the third term represents the Van der Waals attraction between the pairs. The parameters of the inter-atomic interactions are taken from previous studies [270, 458] as listed in Table 4.1. The cation-cation interactions are considered to be purely Coulombic. Convergence of the long-range Coulombic interactions are ensured using Ewald summation technique [364].

Pairs	A_{ij} (eV)	ρ_{ij} (Å)	C_{ij}(eV $Å^6$)
Zr – O	1453.80	0.3500	0
Y – O	1345.80	0.3491	0
O – O	22764.30	0.1490	27.88

Table 4.1: Parameters of the Born-Mayer potential employed in the present simulation [270, 458]. Coulombic interactions are calculated using formal charges on ions.

The initial position of the ions are taken from the X-Ray diffraction studies by Kim et al., with initial unit cell parameters, $a = b = c = 5.137$ Å and $\alpha = \beta = \gamma = 90^0$ [495, 496]. The simulation cell consists of $6 \times 6 \times 6$ cubic unit cells, with the un-doped system (ZrO_2) consisting of a total of 2592 ions (864 Zr-ions and 1728 O-ions). For every x mole percent, Y^{3+} dopants introduced randomly in the fluorite cationic lattice (replacing the same number of Zr^{4+} cations), half the corresponding the number of oxygens are removed from the simulation cell.

NPT-MD simulations are carried out for 20 ns, after dedicating 4 ns for equilibration, over the dopant (yttrium) concentrations of 4 to 40 $mol\%$, for temperatures in the range of $800-2200$ K. Simulations are performed at an integration time steps of 2 fs, and trajectories are stored at intervals of 200 MD steps.

4.3 Results and discussion

4.3.1 Structure

The average lattice parameters of YSZ, $Y_xZr_{1-x}O_{2-x/2}$, over the range 4 to 40 $mol\%$, from NPT-MD simulations at 1300 K are shown in Figure 4.1. The angles (not shown) are found to be within 0.01% of the expected cubic cell. It is noted that cell parameters increase monotonically with increasing dopant concentration, though the change across this wide range of concentration is only within 2%. The observed trend is found to be in agreement with previous experimental reports [497–499].

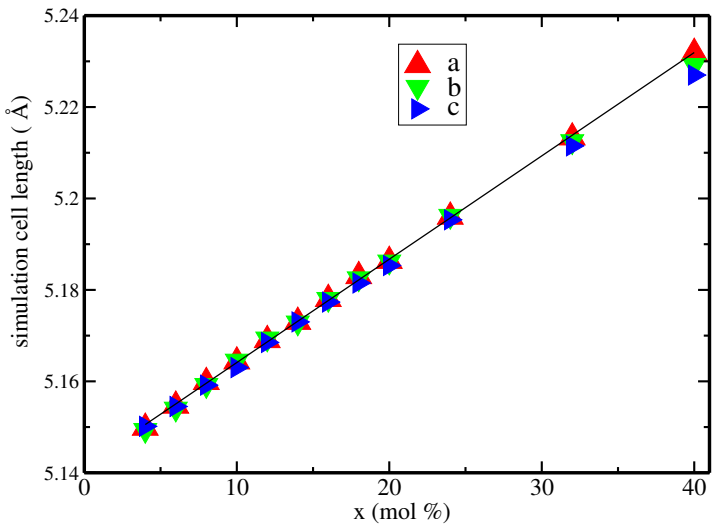

Figure 4.1: Variation of cell parameters in YSZ, $Y_xZr_{1-x}O_{2-x/2}$, for concentration, x ranging from $4-40$ $mol\%$, from 20 ns long NPT-MD simulations at 1300 K.

The radial distribution function (RDF) is given by,

$$g_{\alpha\beta}(r) = \frac{n_\beta(r)}{\rho_\beta \; 4\pi r^2 \delta r} \tag{4.2}$$

where $n_\beta(r)$ is the average number of atoms of species β in a thin spherical shell of radius r and $r+\delta r$, with respect to the reference species α, and ρ_β is the average

number density of β species.

The radial distribution functions between selected ion pairs, averaged over the stored MD trajectory, are shown in Figure 4.2 for a few compositions at 1300 K. The

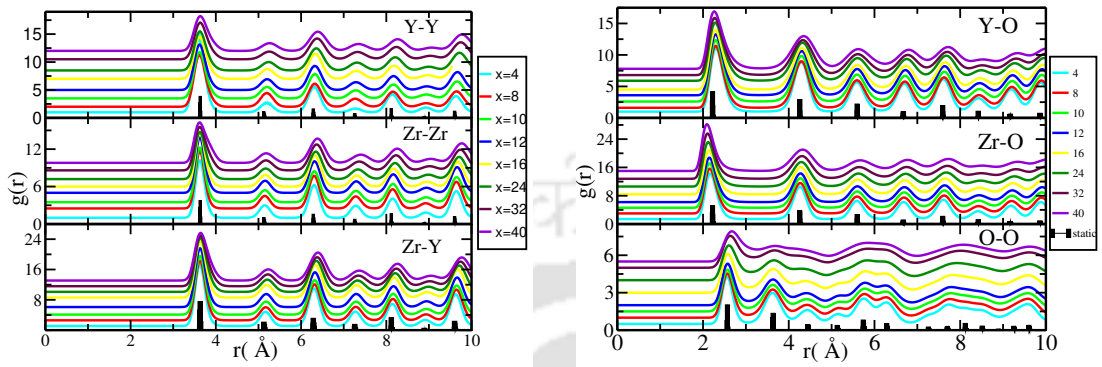

Figure 4.2: *Left panel*: The radial distribution functions (RDFs), $g(r)$ s, between cations, Y-Y, Zr-Y, Zr-Zr, of yttria stabilized zirconia (YSZ), $Y_xZr_{1-x}O_{2-x/2}$, for dopant concentrations, x, ranging from $4-40$ $mol\%$ from 20 ns NPT-MD simulations at 1300 K. *Right panel*: The corresponding RDFs between cation-oxygens, Y-O, Zr-O, and oxygen-oxygen, O-O. The vertical bars in all the graphs are the corresponding $g(r)$ s (with rescaled intensities) calculated from the X-ray structure of the un-doped system [495]. All the RDF s from the MD simulations are displaced uniformly along the Y-axis for clarity.

locations of the successive peaks in the RDFs describes the nearest, second nearest, and the next nearest neighbors, etc. in the material.

Pairs	Neighbour distance (Å)
Zr – O	2.11
Y – O	2.30
O – O	2.58
M – M	3.62–3.64

Table 4.2: The average first neighbor distances between select ion pairs from NPT-MD simulation at 1300 K. M represents the framework cations, Zr^{4+} or Y^{+3}, of the system.

The average nearest neighbor distances for various ion pairs at 1300 K listed in Table 4.2 are in good agreement with previous studies [271, 274, 275, 500].

The cation-cation RDFs in the left panel show a slight increase in their peak positions, more pronounced for peaks beyond 8 Å, due to expansion of the lattice with the dopant concentration. The Zr-O distance is slightly shorter than the Y-O distance across the compositions, indicating that the O-ion occupying the tetrahedral cavities are slightly off-centered, shifting closer to the Zr^{4+} ions owing to their stronger Coulombic attraction with Zr^{4+}. This is in agreement with previous MD

studies by Shimojo et al. [274] and Lau and Dunlap [489]. It is also noticeable in the RDFs that the $Zr-O$ distances slightly decrease for higher dopant concentrations, while the effect is less pronounced for $Y-O$ distances. This again suggests that the higher occupancy of Y^{3+} in the tetrahedral oxygen environment causes the ions to move closer to the Zr^{4+} ions. This shifting of the mean oxygen positions, away from the ideal crystallographic location in favor of Zr^{4+}, results in a slight increase in the $O-O$ distances, together with a broadening of their peaks, which is evident in Figure 4.2 for higher dopant concentrations.

4.3.2 Ion transport

The gross dynamic properties of the YSZ, $Y_xZr_{1-x}O_{2-x/2}$, lattice are extracted from the stored trajectories of ions, across the composition range of 4 to 40 $mol\%$, and over the range of 800 to 2200 K. The mean-squared displacement (MSD) of different species are calculated as,

$$R(t)^2 = \langle [\bar{r_i}(t+\tau) - \bar{r_i}(\tau)]^2 \rangle \tag{4.3}$$

where $\bar{r_i}$ is the position vectors of i^{th} ion at an instant, and the angular brackets represent averaged over all ions and for numerous time origins, τ, as available in the MD trajectory [174].

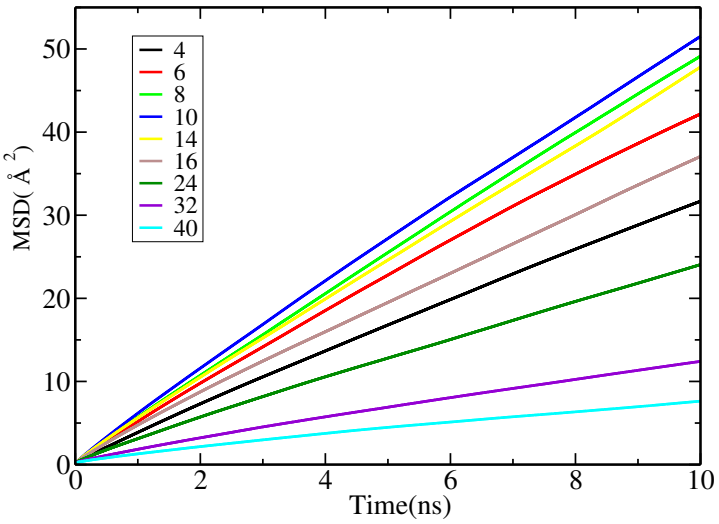

Figure 4.3: Mean square displacement of oxygens ions in YSZ, $Y_xZr_{1-x}O_{2-x/2}$, for concentrations, x, ranging over $4-40$ $mol\%$, from 20 ns long NPT-MD simulation at 1300 K.

The self-diffusion coefficients of oxygens are estimated by fitting to the Einstein relation,

$$D = \lim_{t \to \infty} \frac{R(t)^2}{6t} \tag{4.4}$$

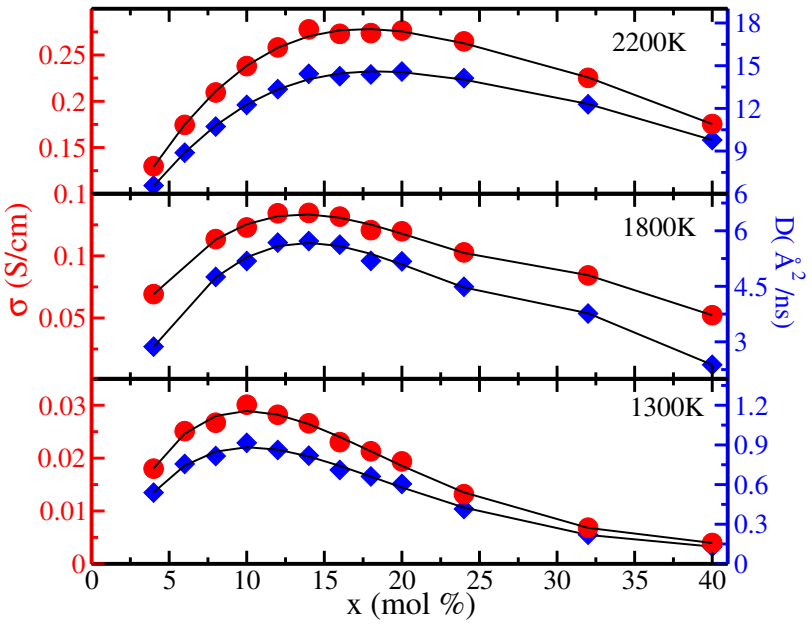

Figure 4.4: Oxygen ion self-diffusivity (blue) and corresponding ionic conductivity (red) in yttria stabilized zirconia (YSZ), $Y_xZr_{1-x}O_{2-x/2}$, for concentrations, x ranging over $4-40$ $mol\%$, at 1300 K, 1800 K and 2200 K. The black lines are only to guide the eye.

shown in Figure 4.3 are the MSD of oxygen ions at 1300 K for a wide range of compositions, 4 to 40 $mol\%$. Self-diffusion is a thermally activated process where the oxygen ions start hopping from site to site resulting in their long-range transport in the matrix. The MSD of Zr^{4+} and Y^{3+} remains flat (not shown) across the temperature range and for all concentrations, $x = 4$ to 40 $mol\%$ of $Y_xZr_{1-x}O_{2-x/2}$, indicating that their dynamics is limited to vibrations about their mean positions.

The ionic conductivity of YSZ due to oxygen ion transport is estimated using the Nernst-Einstein relation,

$$\sigma = \frac{n\, q_0^2\, D}{k_B\, T} \tag{4.5}$$

where n is the number density of oxygen species, q_0 is the formal charge of the oxygen, k_B is the Boltzmann constant, and T is the temperature of the simulation. The estimated self-diffusion coefficient of oxygens as well as the resulting ionic conductivity of YSZ, $Y_xZr_{1-x}O_{2-x/2}$, over compositions, $x = 4$ to 40 $mol\%$ are shown in Figure 4.4 for temperatures, 1300, 1800 and 2200 K. As seen in the figure, at 1300 K the highest conductivity is observed around $x = 10$ $mol\%$, consistent with

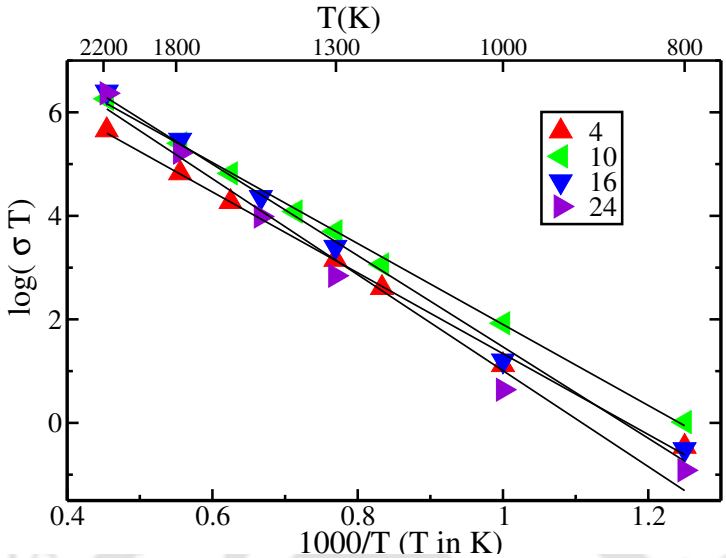

Figure 4.5: Arrhenius plot of oxygen diffusivity in yttria stabilized zirconia (YSZ) from 20 ns long NPT-MD simulations at over the range 800 to 2000 K. The plots are shown only for a few dopant concentrations of $Y_xZr_{1-x}O_{2-x/2}$, namely $x = 4$, 10, 16 and $x = 24$ $mol\%$.

previous experimental and theoretical studies [257, 273, 276, 277, 394, 489, 501, 502]. However, at elevated temperatures, the peak in the self-diffusivity and conductivity of oxygen shifts to higher compositions. The temperature dependence of diffusivity generally found to follow the Arrhenius expressions,

$$D = D_0 \; exp^{-E_a/k_BT} \tag{4.6}$$

where D_0 is the limiting diffusivity value, and E_a is the activation energy. Thus following eq. 4.5 and eq. 4.6 the activation energy for conduction, E_a, are estimated by fitting to,

$$ln(\sigma T) = \frac{-E_a}{k_BT} + ln\sigma_0 \tag{4.7}$$

the Arrhenius plots illustrated in Figure 4.5 for a few compositions, $x = 4$, 10, 16 and 24 $mol\%$, of YSZ. The activation energies estimated for these select compositions are listed in Table 4.3. The activation energies are in reasonable agreement with available experimental and previous theoretical studies [278, 396, 489, 503–511]. As seen, the activation energies are nearly the same for $x = 4$ and 10, but increase thereafter with the composition.

x	E_a (eV) This Work	E_a(eV) Experiment	E_a(eV) Theoretical
4	0.67	0.78–0.90 [393, 396, 504]	–
10	0.67	0.82–1.15 [393, 396, 398, 504, 507]	0.63–0.92 [277, 488, 508, 509]
16	0.76	–	–
24	0.80	–	–

Table 4.3: A compression of activation energy for different dopant concentrations, x, in $Y_xZr_{1-x}O_{2-x/2}$.

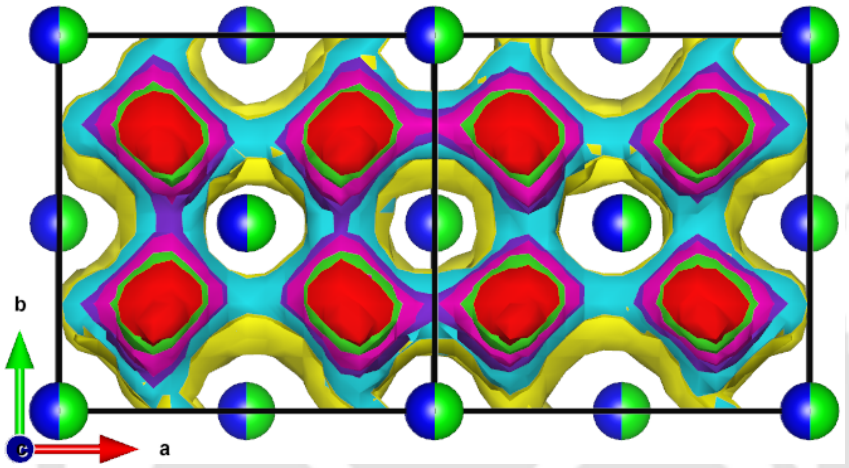

Figure 4.6: Spacial distribution of oxygens over two unit cells are shown for a few iso-density values (increasing from yellow to red) in the fluorite structured YSZ, $Y_xZr_{1-x}O_{2-x/2}$, (for $x = 24$ $mol\%$ from present MD simulations at 1300 K). The *split* balls in blue/green colors indicate the cation sites, which may be occupied by the Zr^{4+} or Y^{3+} ions.

4.3.3 Microscopic insights

The oxygen sites are located at the tetrahedral holes inside the fcc lattice formed by Zr and Y ions. The migration channel connecting these oxygen sites are illustrated in Figure 4.6, where the statistically averaged iso-density surface of oxygen ions are shown over two neighboring unit cells. This is produced by 'collapsing' the oxygen ion trajectories (of the $x = 24$ $mol\%$ at 1300 K) in the $6 \times 6 \times 6$ simulation cell into a $2 \times 1 \times 1$ unit cell. Consistent with many previous MD simulation studies, the oxygen migration channels are found to be parallel to the crystallographic axes connecting the tetrahedral holes [273, 277–279, 471, 488].

The microscopic energy barrier for the ion hops between two neighboring sites at 1300 K are shown in Figure 4.7, for a few select dopant concentrations, $x = 4, 10, 16$

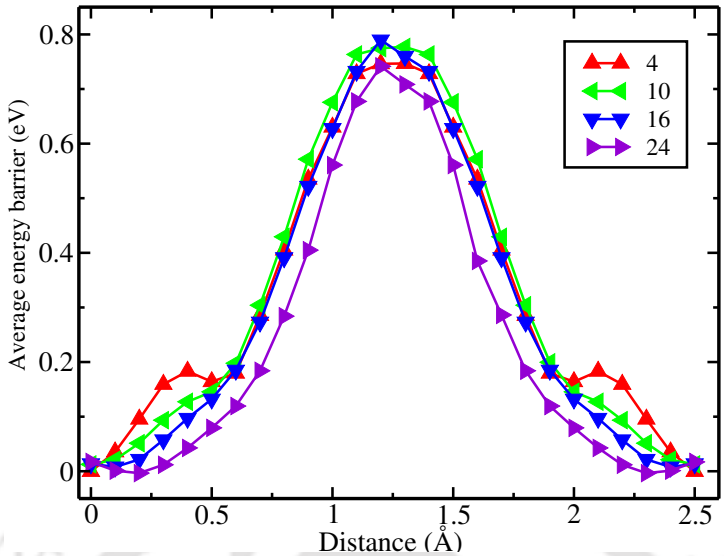

Figure 4.7: Microscopic energy barrier for oxygen ion hops calculated along the diffusion pathway at 1300 K for dopant concentration $x = 4, 10, 16$ and 24 $mol\%$.

and 24 $mol\,\%$. These are calculated by noting that the individual potential energy of an oxygen ion due to the rest of the $N-1$ ions in the system may be defined as,

$$u_i = \frac{1}{2} \sum_{j=1,\, j\neq i}^{N} V_{ij} \tag{4.8}$$

where V_{ij} is the interaction potential in equation 5.1, and N is the total number of ions in the system. Thus the total potential energy of the configuration is given by,

$$U = \sum_{i=1}^{N} u_i. \tag{4.9}$$

These individual energies, u_i 's, are stored along with the trajectory during the course of the simulation itself. During the analysis, these energies are cumulated in linear bins along the migration path connecting the two respective neighboring oxygen sites and averaged, to produce the barrier profile. Further, note that the energy profiles shown in Figure 4.7 are with reference to the average potential energy of an ion in its ideal crystallographic location for the *respective* compositions at 1300 K, thus has its minimum of zero at both edges of the channel of length 2.51 Å.

This microscopic energy barrier for ion transport, measuring about 0.75 eV, appears at a distance of around 1.25 Å, mid-way between two neighboring sites. These values are in reasonable agreement with previous studies [512, 513]. The

height of the microscopic barrier is well within the range of the activation energy barriers (0.67 to $0.8eV$) estimated from the Arrhenius plot in Figure 4.5, and listed in Table 4.3. However, it is intriguing that the microscopic barriers are roughly the same across the composition range, unlike the activation energy which shows an increasing trend with composition. Also, noticeable in Figure 4.7 is a prominent shoulder around 0.4 Å in the microscopic barrier of the $x = 4\ mol\%$ composition. As discussed in one of our earlier studies on $La_{1-x}Sr_xMnO_{3-0.5x}$ this originates due to the 'knock-out' mechanism of ion hops [473]. An oxygen that is in an imminent hop to one of the neighboring sites pushes the ions at its destination, causing an additional increase in its potential energy owing to mutual repulsion. Naturally, this effect is more pronounced where the density of the mobile species is higher.

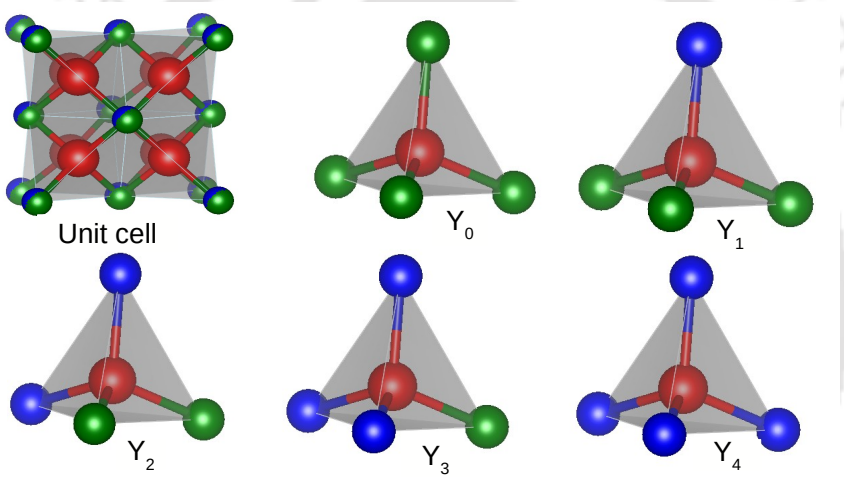

Figure 4.8: Different possible oxygen environments in $Y_xZr_{1-x}O_{2-x/2}$, based on the surrounding cation organization is demonstrated. On the top left, the cubic unit cell of $Y_xZr_{1-x}O_{2-x/2}$, with oxygen sites (red) located at the tetrahedral holes of the *fcc* sublattice of the cations, Zr^{4+} (green) and Y^{3+} (blue), is shown. In the remaining figures, labeled Y_0 to Y_4, the different oxygen environments are classified based on the number of Y^{3+}-ion occupying the corners of the tetrahedra. The use of the "ball-stick" model is only for the ease of visualization.

Noting that, thus far, we don't have a clue in understanding the observed variation in oxide ion diffusivity or ionic conductivity of the $Y_xZr_{1-x}O_{2-x/2}$, thus we have examined the oxygen environments in greater detail. Shown in Figure 4.8, the oxygens occupy the tetrahedral holes of the FCC lattice formed by the cations. That is, the oxygen ions can be imagined to be at the center of tetrahedra with its corners decorated by Zr^{4+} or Y^{3+} ions. This permits five different possible environments for oxygen ions to occupy, such as all four corners formed by the Zr^{4+}, to all four corners formed by the Y^{3+}, and three other combinations differing in Y^{3+} occu-

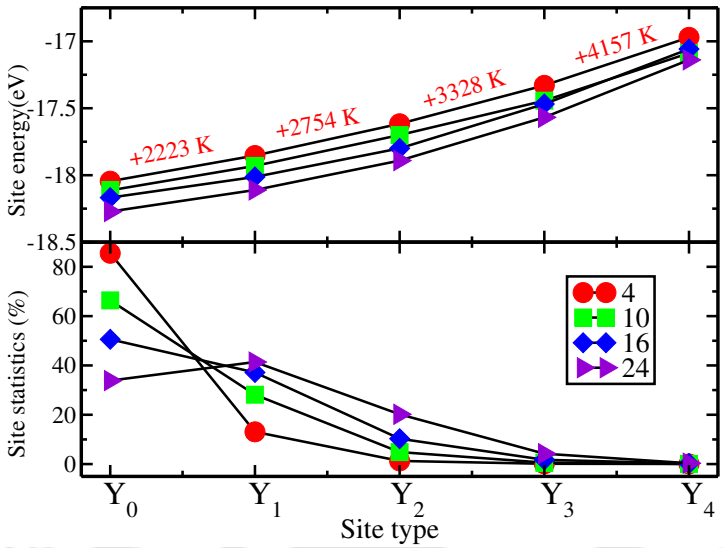

Figure 4.9: *Top panel*: Site energy of oxygen at different environments, Y_m, where $m = 0, 1, ...4$, for a few compositions, $x = 4, 10, 16$ and 24 $mol\,\%$ of $Y_xZr_{1-x}O_{2-x/2}$. The annotations in red show the increment in the site energy (as the temperature in K), with the addition of every Y^{3+} in the oxygen environment, demonstrated for the $x = 4$ $mol\,\%$ composition. *Bottom panel*: Statistics of the Y_m sites in the matrix for a few concentrations.

pancy. We chose to label these oxygen environments as, Y_m, where $m = 0, 1, 2, 3$ or 4, indicating the number of Y^{3+} present in an oxygen environment.

In Figure 4.9(Bottom panel) the statistics of these sites across a few selected compositions are shown as the percentage of the total number of cations (864) in the $6 \times 6 \times 6$ simulation cell. For every composition, x, these statistics, calculated based on the (*random*-) cation distribution in the initial fcc sub-lattice, remains throughout the simulation and over the temperatures examined, since there is no cationic diffusion in the system. Figure 4.9(top panel) shows the potential energy of oxygen ions, statistically averaged over the MD trajectory, while occupying the various available oxygen sites, Y_0 to Y_4. It shall be noted that this 'site-energy' of the oxygens increases from Y_0 to Y_4 across the composition. In other words, every Y^{3+} in the local tetrahedral environment has an energy penalty for the occupying oxygen. This increase in energy is attributed to the less stronger Coulombic interaction between the O^{2-} ions with Y^{3+}, compared to Zr^{4+} ions. As seen in Figure 4.9, this estimated increase in energy from Y_0 to Y_4, across the compositions demonstrated, is over 1 eV ($\sim 10^4$ K) which is quite significant with respect to the simulation temperature. We shall note in passing that the site energy of oxygen for all the five different sites also shows a marginal increase with concentration, x, but

is inconsequential as far as the dynamics or transport properties of the oxygen ions are concerned.

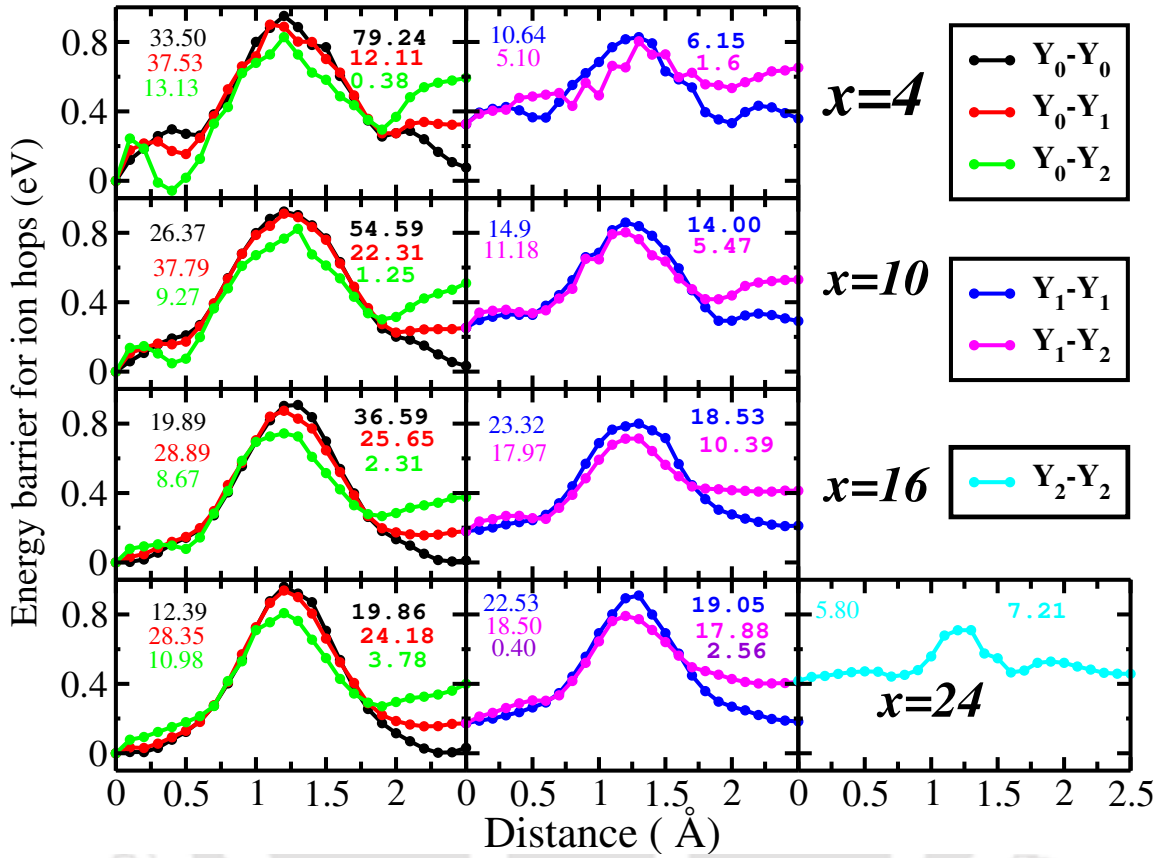

Figure 4.10: Energy profiles of oxygen ions along possible channels connecting the different oxygen sites are shown, for the few select compositions, $x = 4, 10, 16$ and 24 $mol\,\%$ of $Y_xZr_{1-x}O_{2-x/2}$, from NPT-MD simulation at 1300 K. All the energies are relative to the energy of the Y_0 site of the respective composition. The legends are common to all the plots. Marked with the same color, the numbers on the left side of each panel is the estimated traffic through the corresponding channel (in %), and numbers on right gives the percentage of the actual number of channels present in the matrix for a given composition. Channels having less than 4% of traffic are not shown. See text for details.

For a better understanding, the energetics and 'traffic' of oxygens along the various possible channels connecting the adjacent tetrahedral oxygen sites are examined. Figure 4.10 presents the potential energy profiles calculated for various individual channels, labelled $Y_i - Y_j$, where $i, j = 0, 1, 2, 3$ or 4, for a few select compositions, $x = 4, 10, 16$ and 24 $mol\,\%$ of YSZ ($Y_xZr_{1-x}O_{2-x/2}$), based on NPT-MD simulation at 1300 K.

These profiles are calculated in similar lines as detailed in the context of Figure 4.7 except that distinction of the migration channel connecting the two neigh-

boring oxygen sites, Y_i and Y_j, are made. Further, the origin of the distance measure along the channel is chosen such that $i \leq j$ to ensure that the nature of the profiles are sensitive to departing and arrival sites. The percentage of the 'traffic' of oxygens through respective channels are marked in the same color to the left corner of each panel. The traffic is estimated based on the population at the central bin of each channel, but disregarding the direction of the hop. The numbers on the right-corner of each panel give the percentage of the actual number of channels present in the matrix, for the composition. It shall be noted that, since adjacent tetrahedral oxygen sites share a common cationic edge, not all distinct permutations of channels are possible, limiting the number to a maximum of twelve. Further, out of these possible channels, those having less than 4% of traffic are left out of Figure 4.10 due to poor statistics. It is noted that in all cases, the barriers are roughly within the range of 0.75 to 0.95 Å. The $Y_0 - Y_0$ channel exhibits the highest barrier for all compositions, but the barrier reduces slightly with the number of yttrium in the environment of both the departure and destination oxygen sites. It is not surprising that with composition there is a systematic reduction in the fraction of channels (marked on the right-corner of each panel) of lower "index", say in the order (from top-down) the legends are presented in Figure 4.10, at the expense of others. However, it is intriguing that some of the channels, particularly $Y_0 - Y_1$, $Y_0 - Y_2$ and $Y_1 - Y_2$, accounts for an excessive fraction of the traffic (marked on the left corner of the panels) relative to their actual count (marked on the right) in the matrix. This feature is more pronounced at lower concentrations.

In the past, some of the leading authors have characterized the energy barriers in terms of the common cationic edge, such as the $Zr-Zr$, $Zr-Y$, and $Y-Y$, connecting the departure and destination tetrahedra. Krishnamurthy et al. [277] observed that the energy barriers for oxygen migration through the $Y-Y$ edges of the cationic tetrahedra are higher than that of the $Zr-Y$ and $Zr-Zr$ edges. Their study proposed that this is the major reason for the non-monotonic variation in conductivity. A later simulation study by Tarancón et al. [278] also arrived at a similar conclusion but also proposed that the migration energy of oxygen ions are independent of the departing and destination tetrahedral environments. However, our observation of significant differences in the energy of these oxygen environments suggests that they play a significant role in the long-range transport of ions in the system. In a more recent study, Jaipal and Chatterjee [279] noted that oxygen migration from the yttrium-rich environments are much fewer than those from zirconium-dominant environments, which is in agreement with the present observations. The present MD

Edge type	$Y_0 - Y_0$	$Y_0 - Y_1$	$Y_0 - Y_2$	$Y_1 - Y_1$	$Y_1 - Y_2$	$Y_2 - Y_2$
x=4						
Zr-Zr	0.95 (33.49/ 79.24)	0.90 (37.53/ 12.07)	0.82 (13.15/ 0.38)	0.66 (10.44/ 0.48)	0.58 (4.9/ 0.03)	– –
Zr-Y	– –	– –	– –	1.9 (0.18/ 5.67)	1.89 (0.1/ 1.62)	– –
x=10						
Zr-Zr	0.92 (26.47/ 54.59)	0.91 (37.93/ 22.31)	0.82 (9.3/ 1.25)	0.75 (14.79/ 2.71)	0.63 (10.99/ 0.36)	– –
Zr-Y	– –	– –	– –	1.8 (0.16/ 11.28)	1.58 (0.23/ 5.11)	1.63 (0.09/ 0.64)
x=16						
Zr-Zr	0.91 (19.9/ 36.59)	0.87 (28.9/ 25.65)	0.74 (8.7/ 2.31)	0.74 (23.08/ 5.18)	0.63 (17.64/ 1.11)	– –
Zr-Y	– –	– –	– –	1.79 (0.03/ 13.38)	1.71 (0.32/ 9.27)	1.27 (0.5/ 1.96)
x=24						
Zr-Zr	0.95 (12.39/ 19.86)	0.93 (28.35/ 24.18)	0.80 (10.99/ 3.78)	0.86 (22.24/ 7.25)	0.68 (17.88/ 2.68)	0.61 (5.0/ 0.13)
Zr -Y	– –	– –	– –	1.79 (0.3/ 11.8)	1.66 (0.62/ 15.2)	1.49 (0.8/ 5.11)

Table 4.4: Energy barriers for oxygen migration, estimated individually for different cation-cation edges connecting the departing and destination tetrahedral sites, along different migrating channels, for select compositions, $x = 4, 10, 16$ and 24 $mol\,\%$ of $Y_xZr_{1-x}O_{2-x/2}$, from NPT-MD simulation at 1300 K. All the barriers are with respect to the energy of the Y_0 site of the respective composition. The quantities in brackets are the corresponding estimates for the traffic, and the actual number of edges in the matrix, both in percentage. Y–Y edges are too few in number ($< 0.01\%$) even for the $x = 24\,mol\,\%$ composition, thus not shown.

study, in addition to examining the energetics and contribution to transport from various channels as presented in Figure 4.10, a further characterization in terms of the cationic edges present in the dominant channels are carried out.

The energy barriers along prominent channels resolved in terms of the cationic

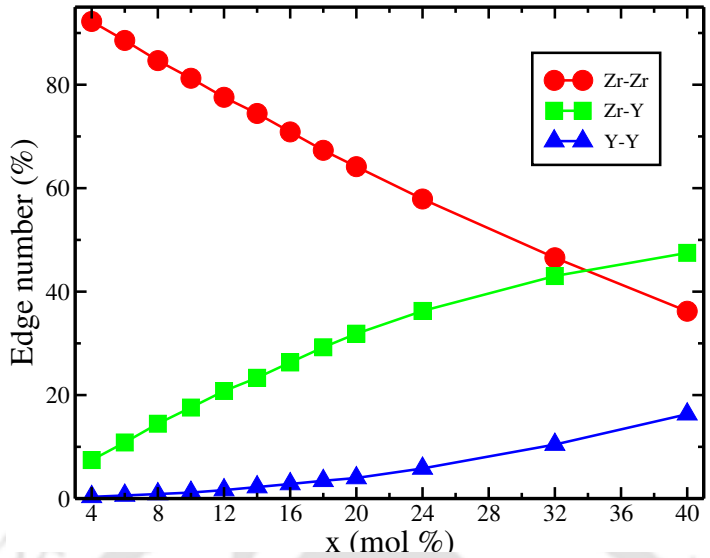

Figure 4.11: Number of Zr-Zr, Zr-Y, Y-Y edges variation with concentration in $Y_xZr_{1-x}O_{2-x/2}$for x ranging over 4 to 40 $mol\%$.

edges involved are presented in Table 4.4 for a few compositions from NPT-MD simulations at 1300 K. The quantities in the parenthesis represent respectively the percentage of traffic through the edge, and the fraction of edges present in the matrix (in %). It shall be noted that the energetics and statistics presented are estimated disregarding the direction ion hops. Before going into the discussion of the results, it shall be noted that the channels connecting to the Y_0 sites can have only the $Zr-Zr$ edges, while those connecting Y_1 sites to the same kind or to higher index sites (Y_2 or Y_3) can have both $Zr-Zr$ as well as $Zr-Y$ edges. $Y-Y$ edges can appear in Y_2-Y_2 and higher indexed channels. But in the present case, the $Y-Y$ edges did not measure any traffic in the Y_2-Y_2 channels, thus not listed in Table 4.4. However, from the Y_2-Y_3 channel, which is otherwise omitted in the foregoing discussions due to less 4 % traffic, an energy estimate of 1.78 eV is obtained for the $x=24$ composition, but based on extremely low traffic of about 0.0001 % – mentioning here for the sake of completeness.

As seen, the $Zr-Y$ and $Y-Y$ edges are of significantly higher in energy than the respective $Zr-Zr$ edges. Consequently, $Zr-Y$ and $Y-Y$ edges account for only a negligible fraction of the total traffic through the respective channels across the compositions. It shall also be noted in passing that, as expected, the weighted average of the edge-wise energies over the $Zr-Zr$ and $Zr-Y$ edges, for a given channel, is in agreement with the barriers reflected in the potential energy profiles shown in Figure 4.10. Essentially, these results suggest that nearly all the oxygen

transport, across the composition range, occur through the $Zr - Zr$ edges due favorable energy barriers. These observations are also in agreement with previous leading authors [277, 278, 514]. At this point, it is worthy of noting the statistics of the actual number of these edges in the matrix for different concentrations, shown in Figure 4.11. It is seen that the energetically unfavorable edges, $Zr - Y$ and $Y - Y$, increases monotonically with composition, at the expense of $Zr - Zr$ edges.

Further, it shall be noted that out of the six channels originating from any given oxygen site, the Y_1 sites have three $Zr - Zr$ edges and an equal number of $Zr - Y$ edges, while Y_2 sites have four $Zr - Y$ edges, and one $Zr - Zr$ and one $Y - Y$ edge. Thus, based on energetic considerations, the favorable channels originating from Y_1 sites is halved. While for the Y_2 sites, with just one favorable channel available, the incoming ions will, by and large, hop back to the departure site, with hardly any contribution to the long-range transport. Thus, the sites of still higher energy, Y_3 and Y_4, will contribute negligibly to the long-range transport, or self-diffusivity, of oxide ions.

Thus, the increase in the number of unfavorable sites, particularly Y_2, Y_3 and Y_4, compounded by their higher energy edges accounts for the slower oxygen mobility at higher concentrations (say beyond, $x = 10\,mol\%$). Now, focusing on the $Zr - Zr$ edges, a couple of interesting observations in Table 4.4 are that the energy barrier along the $Zr - Zr$ edges, show systematic reduction with the channel index, from left to right as organized in the table, for all compositions. Another aspect is that $Y_0 - Y_1$, $Y_0 - Y_2$ and $Y_1 - Y_2$ channels account for an excessive fraction of the traffic relative to their actual count in the matrix, also noted earlier in the context of Figure 4.10. Both features are closely related and can be understood in terms of the oxygen-oxygen interactions or in a broader context referred to as the ion-ion correlation [474, 476, 515–517] between the mobile species.

As noted earlier in the context of Figure 4.9, the oxygen occupancy of sites decreases as we move from Y_0 to Y_4, due increase in their site energies. A lower occupancy at the destination site facilitates the ion hops. For instance, in the $x = 4\,mol\%$ composition, $Y_0 - Y_0$ channel accounts for only 33 % of traffic despite having close to 80 % of the population in the matrix, in contrary $Y_0 - Y_1$ which accounts for over 37 % of traffic despite having only 12 % of channels. This clearly suggests that hopping from Y_0 to Y_1 site is facilitated by the lower occupancy of the Y_1 sites. The measured 13 % of traffic in the $Y_0 - Y_2$ channel with less than 0.4% of channels also follows the suit. Now, if we compare the the transport between $Y_0 - Y_2$ and $Y_1 - Y_2$, while 13 % of traffic is due by 0.38% of $Y_0 - Y_2$ channels, the

$Y_1 - Y_2$ contributes 4.9 % with just about 0.03% of channels. Here again, hops from Y_2 to Y_1 is aided by the relatively lower occupancy of the Y_1 sites in comparison to Y_0 sites. The reduction in the energy of the $Zr - Zr$ edges with the index of the channels owes to the existence of a certain degree of 'knock out' mechanism, where in an oxygen ion attempting to hop to a neighboring site need to dislodge the ion at the destination to be successful, costing higher barriers. Such events again depend on the occupancy of the destination site, controlled by the Boltzmann factor. Again, the slight reduction in the energy disparity of the $Zr-Zr$ edges of individual channels with concentration is attributed to the lower degree of ion-ion correlations, due increase in oxygen vacancies in the system. These observations also imply that energy barriers for ion hops are further sensitive to the departure and destination sites, due to their differential occupancy.

4.4 Summary and Conclusions

The structural and dynamical properties of the oxide ion conducting yttria-stabilized zirconia, $Y_xZr_{1-x}O_{2-x/2}$, is investigated employing isothermal-isobaric ensemble molecular dynamics simulations over a wide range of dopant concentrations (x = 4 to 40 $mol\%$) and temperature (800 - 2200 K). It is noted that the cell parameters of the cubic (fluorite) structure of the system increases linearly with the dopant concentration, across the entire range investigated. The self-diffusivity of oxygen ions as well as the ionic conductivity exhibit maximum around 10 $mol\%$ of yttrium doping at 1300 K. This maximum shifts to higher concentrations at elevated temperatures. The activation energies estimated from the Arrhenius plot of the conductivity shows an increase from 0.67 eV to 0.8 eV over the range of $x = 4$ to 24 $mol\%$. These observations are in good agreement with previous experimental and theoretical studies.

The microscopic analysis of the oxygen migration reveals that oxide ions, residing at the tetrahedral holes of the fcc sub-lattice of the cations, hops to neighboring sites along straight channels parallel to the crystallographic axes, producing long-range transport. The energies of the different oxygen sites are found to increase significantly with the number of Y^{3+} cations present in the environment, owing to the weaker Coulombic interaction of oxygen with yttrium, in comparison to Zr^{4+}. This difference in energy of the distinct oxygen sites results in variable occupancy of the sites, which is found to play a significant role in the oxygen migration in the matrix. The energetics as well as the contribution to overall transport along different channels connecting the oxygen sites are analysed in detail. These quantities, when

further resolved along the different possible cationic edges, such as the $Zr - Zr$, $Zr - Y$, and $Y - Y$ provide fresh insights on the mechanism of oxygen transport in the system. The $Zr - Y$ and $Y - Y$ edges found to pose prohibitively high barriers for oxygen migration, much higher than the $Zr - Zr$ edges. These energetically unfavorable edges around a given oxygen site, by their very nature, increase with the Y^{3+} count in the environment.

In retrospect, the generation of oxygen vacancies, taken singularly, should promote the self-diffusivity of oxygens in the system due availability of more vacant sites in its proximity. The increase in the lattice parameters with a composition also generally helps faster ion transport due to the widening of bottlenecks. Thus, an increase in the higher energy sites, and the consequent increase in cationic edges of prohibitively high energies, explain lower oxygen diffusivity at higher compositions. These results suggest that with a more homogeneous distribution of yttria in the matrix the oxide ion conductivity could be enhanced, by virtue of optimizing the yttrium presence in the local oxygen environments. Possibly, higher sintering temperatures of the sample, and for longer durations, could be one of the ways to achieve this. Further theoretical investigations would be required for a more comprehensive understanding of the nature of oxide ion transport in these systems. It is further noted that, for ions hopping between neighboring sites a lower occupancy at the destination site poses lower barriers and makes a significantly higher contribution to the transport relative to their actual count in the matrix. This suggests that the oxygen-oxygen interaction operating at the microscopic level also plays a role in the ion migration mechanism.

Arguably, the optimal conductivity with mobile ion concentration is a universal behavior, given that several families of fast ion conducting solids, including many aliovalently doped alkali ion conductors, exhibit this behavior. A better understanding of the phenomenon would be of great benefit in the selection and fine-tuning of solid electrolytes, in terms of size, charge and amount, etc., of the dopant species, for commercially viable next-generation portable energy devices.

Chapter 5

Oxide Ion Transport In Cation-Ordered Yttria Stabilized Zirconia

5.1 Introduction

Despite being a promising electrolyte for SOFC, YSZ solids have a major drawback, including their high operating temperature (> 1000°C) which leads to the generation of thermal stress and degradation of the electrode-electrolyte interface, as discussed in Chapter 1. This limits the choice of electrodes it can pair with, shortening of the lifetime of the cell, and reduced operational safety [50, 518, 519]. These hurdles can be resolved by reducing the operating temperature of the fuel cell which demands, a significant improvement in the ionic conductivity of the electrolyte, among other factors governing the performance of the electrodes at lower temperatures. Promising experimental strategies presently evolving in this direction are to co-dope [491] YSZ with other dopants (Sc^{3+}, Sm^{3+}, Gd^{3+}) or, possibly more effectively, by employing various controlled fabrication techniques such as atomic layer deposition (ALD) [520, 521], pulsed laser deposition (PLD) [522, 523], etc. In order to comprehend the fundamental process of oxygen anion transport in anion-conducting ceramics, a considerable amount of theoretical and experimental research has been done. [250, 293, 323, 327, 520, 524–534].

According to Jihwan et al., [299] the ALD cermet interlayer outperforms the non-mixed cermet layer, making it an ideal experimental technique for structuring by depositing interlayers. YSZ electrolytes deposited through the surface modi-

The manuscript based on this chapter is under preparation.

fication layer (SML) are studied by Chao et al. [520, 521]. They reported that layered YSZ with Zr/Y stacking in a systematic manner, having a dopant concentration 14 mol% has higher bulk ionic conductivity than randomly doped YSZ with a dopant concentration of 8 mol% [520, 521]. In addition to these controlled synthesis techniques, it has been experimentally discovered that the $Y_{0.25}Zr_{0.75}O_{2-x}$ and $Y_{0.5}Zr_{0.5}O_{2-x}$ phases can be formed when the cations in the unit cell have an ordered structure [535]. Furthermore, according to a number of theoretical and experimental investigations on vacancies and cation arrangements, the vacancy binds strongly to the host Zr^{4+} cations, producing an arrangement where the first nearest neighbor is Zr^{4+} and the second nearest neighbor is Y^{3+} for reliable ionic transport [536–540].

Due to the high operating temperature and complex chemical reactions of the SOFC, these experimental techniques can be difficult to carry out in order to determine how other internal variables affect the microscopic mechanism of the electrolyte. The precise mechanism of oxygen transport with various microscopic factors and its interrelationships remain unclear and additionally, the arrangement of the anions (oxygens) and cations (yttria/zirconia) in the cubic YSZ is a subject of discussion. This Chapter describes how different cationic arrangements in YSZ ($Y_xZr_{1-x}O_{2-x/2}$) influence oxygen ion transport in the system at a dopant concentration of x =12.5 mol%, which is close to the optimal value for the highest ionic conductivity, as reported in Chapter 4 and in previous studies. The microscopic analysis of these ordered structures provides a better understanding of the mechanism of oxygen ion mobility in these systems.

5.2 Simulation Details

5.2.1 Structural Models

In order to investigate the effect of cationic ordering on ion transport in YSZ ($Y_xZr_{1-x}O_{2-x/2}$), five different Zr/Y-ordered structures at a dopant concentration of 12.5 mol% are compared with the random structure of the same concentration. This choice of dopant concentration is in view of the fact that YSZ exhibits its highest conductivity around 8-12 mol% [276, 277, 393, 395, 396, 541]. The cations (Y and Zr) occupy the face-centered cubic position in the fluorite YSZ structure, and the oxygens occupy the tetrahedral interstices of the FCC lattice. As a result, each oxygen has four neighboring cations, and each cation is coordinated to eight oxygens in the undoped system.

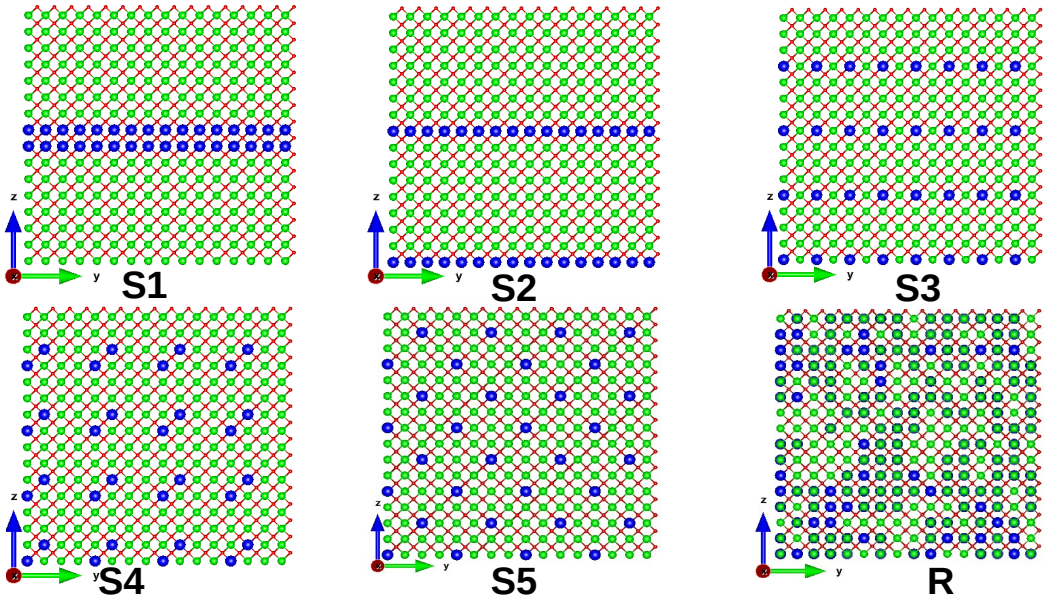

Figure 5.1: The various Y^{3+} ordered structures, labelled S1 to S5 (Y^{3+} as blue balls and the Zr^{4+} in green), in the 12.5 mol% of $Y_xZr_{1-x}O_{2-x/2}$ examined in the present NPT-MD simulations at 1300 K are demonstrated. Structure R has the Y^{3+} dispersed randomly at the cationic sites.

The size of the simulation cell is chosen to be $8 \times 8 \times 8$ unit cells, containing a total of 6144 ions, including 2048 cations (256 – Y^{3+} and 1792 – Zr^{4+} ions). Given that the cations in a unit cell are located at $(0,0,0)$, $(\frac{1}{2},\frac{1}{2},0)$, $(0,\frac{1}{2},\frac{1}{2})$, and $(\frac{1}{2},0,\frac{1}{2})$, the simulations cell consisting of $8 \times 8 \times 8$ unit cells feature 16 cationic layers, when visualized staked along the z- axis. The five different orders of Y^{3+}- layers (stacked along the z- axis) in the simulation cell, labeled S1 to S5 as illustrated in Figure 5.1, may be described as,

- S1: two sandwiching *full*-layers of Y^{3+} (that is, one block of unit cells spanning xy-plane),
- S2: two *full*-layers of Y^{3+} separated by half the simulation cell (that is, Y^{3+} occupies the $(l,m,0)$, $(l\frac{1}{2},m\frac{1}{2},0)$, $(l,m,4)$ and $(l\frac{1}{2},m\frac{1}{2},4)$ locations in the simulation cell, where l and m are 0 to 7.),
- S3: four *half-filled*-layers, with Y^{3+} occupying *only* the origin, $(0,0,0)$ of alternate unit cells along the z-axis (that is, at locations (l,m,n) of the simulation cell, where l and m can be between 0 to 7, and $n = 0, 2, 4$ and 6),
- S4: eight sparsely-filled layers of Y^{3+} created by displacing alternate corner ions on the basal planes in the S3 structure by $(\frac{1}{2},\frac{1}{2},\frac{1}{2})$,

- S5: eight sparsely-filled layers of Y^{3+} created by displacing alternate corner ions on the basal planes of the S3 structure by $(0, 0, 1)$.

The nature of oxygen transport in these structures are compared with a $'random'$ structure, named R, wherein the Y^{3+} ions replace the Zr^{4+} at random locations in the simulation cell.

5.2.2 Interatomic Potential

Classical MD simulations are performed on YSZ in the isothermal-isobaric (NPT) ensemble at 1300 K [459], using Born-Mayer interaction potential [457],

$$V_{ij} = \frac{1}{4\pi\epsilon_0}\frac{q_i q_j}{r_{ij}} + A_{ij}exp(\frac{-r_{ij}}{\rho_{ij}}) - \frac{C_{ij}}{r_{ij}^6} \tag{5.1}$$

where q_i and q_j represent the charges of the i^{th} and j^{th} ions, separated by distance r_{ij}. The strength and the range of the short-range repulsion between the ions are respectively controlled by A_{ij} and ρ_{ij}. The C_{ij} incorporates the strength of the Van der Waals attraction between the ion pairs. The parameters of the interatomic interaction, listed in Table 5.1, are taken from previous studies [270, 458]. The excellent quality of these parameters are demonstrated in many earlier MD studies [270, 488, 542].

Pairs	A_{ij} (eV)	ρ_{ij} (Å)	C_{ij} (eVÅ^6)
Zr – O	1453.80	0.3500	0
Y – O	1345.80	0.3491	0
O – O	22764.30	0.1490	27.88

Table 5.1: Parameters of the Born-Mayer potential employed in the present simulation. [270, 458] Coulombic interactions are calculated using formal charges on ions.

NPT-MD simulations are started from unit cell parameters, $a = b = c = 5.137$ Å and $\alpha = \beta = \gamma = 90°$, reported by the X-ray diffraction studies by Kim em et al. [495] After assigning $5ns$ to equilibration, production runs of $30ns$ are carried out at 1300 K, for all the structures described above. The simulations are performed with a time step of 2 fs, and the trajectories are recorded at intervals of 1000 MD steps. Ewald summation technique is employed under three-dimensional periodic boundary conditions, for the convergence of Coulombic interactions [364]. The simulations are carried out using LAMMPS software [459].

5.3 Results and discussion

5.3.1 Structure

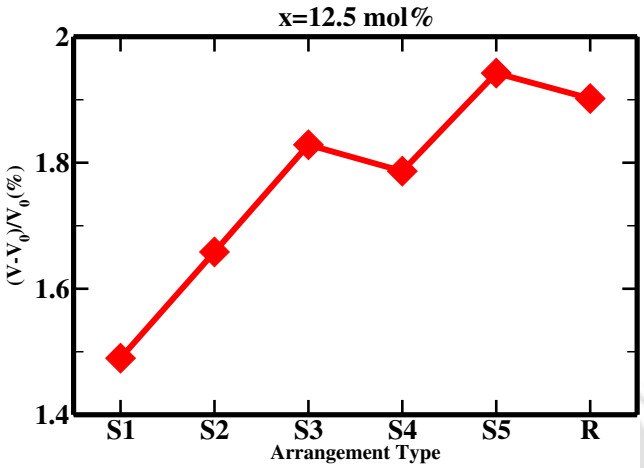

Figure 5.2: Variation in relative volume of all ordered and random YSZ structured, $Y_xZr_{1-x}O_{2-x/2}$, with x=12.5 mol%, obtained from 30ns long NPT-MD simulations at 1300 K.

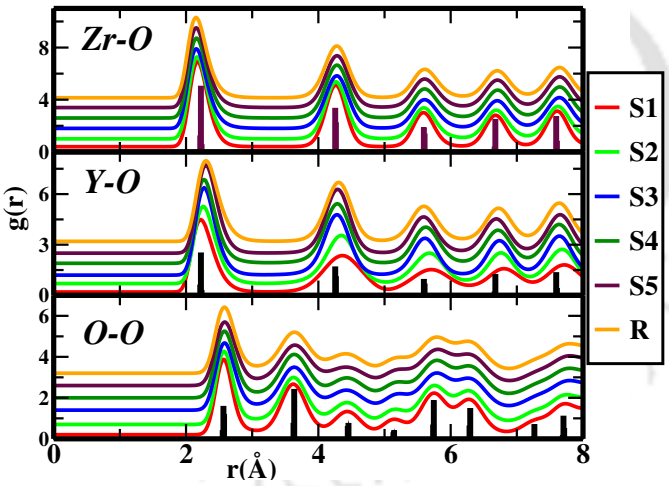

Figure 5.3: The corresponding Radial distribution functions(RDFs), g(r), between cations-oxygens (Y-O, Zr-O), and oxygen-oxygen (O-O). So the vertical bar of each graph represents the associated g(r)s (with rescaled intensities) estimated from the undoped system's X-ray structure. For clarity, all of the RDFs from the MD simulations are uniformly shifted along the Y-axis.

The NPT-MD simulations of various yttria-ordered structures showed only marginal changes in simulation cell volume ($\leq 2\%$) compared to their respective static structures, as illustrated in Figure 5.2. Presented in Figure 5.3 are the radial distribution

functions (RDF) for these structures, defined as,

$$g(r) = \frac{1}{\rho 4\pi r^2 \delta r} [\frac{1}{N} \sum_{i=1}^{N} n_i(r, \delta r)] \tag{5.2}$$

where ρ represents the number density of the ion, N stands for the total number of ions, and $n(r, \delta r)$ stands for the number of ions within the spherical shell of radius r and thickness δr.

For a given composition Zr-O distances tend to decrease when the dopant Y^{3+} is more dispersed in the matrix, while the converse applies to Y-O distances. Also, the Zr-O distances are shorter than the Y-O distance, indicating that oxygens in the tetrahedral cavity are off-centered locating themselves closer to Zr^{4+} rather than Y^{3+} due to greater Coulombic attraction. This results in an increasing disorder of the oxygen sub-lattice, causing a broadening in the O-O RDFs.

5.3.2 Oxide Ion transport

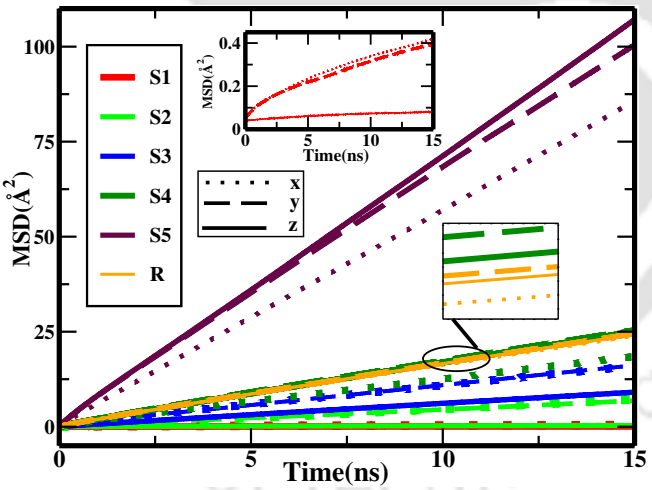

Figure 5.4: Mean squared displacement (MSD) of oxygen ion in YSZ ($Y_xZr_{1-x}O_{2-x/2}$) having different Y^{3+} orderings, for x =12.5 mol% from 30 ns of NPT-MD simulations at 1300K. These MSDs are resolved along the different crystallographic directions and can be distinguished from the line types (dot, dashed or continuous) while not overlapping. The inset highlights the anisotropic, though low, MSD of the S1 structure.

As expected, the cation-ordered YSZ lattices shown in Figure 5.1 are in general anisotropic in nature. Thus the transport properties of the different Y^{3+} ordered matrices are examined for the mean square displacement (MSD) of oxygen ions,

resolved along the different Cartesian axes, given by,

$$R_\alpha(t)^2 = \langle [r_\alpha^i(t) - r_\alpha^i(0)]^2 \rangle \tag{5.3}$$

where $r_\alpha^i(t)$ represents the coordinate of the i^{th} ion at an instant time t, and α stands for Cartesian directions x, y or z. The angular bracket denotes averaging over all the oxygen ions in the system, and for multiple time origins, across the length of the simulation. The self-diffusivities of oxygen along different Cartesian directions may be estimated from the slope of the MSDs,

$$D_\alpha = \lim_{t \to \infty} \frac{R_\alpha^2(t)}{2t} . \tag{5.4}$$

As expected, the MSDs resolved along the coordinate axes shown in Figure 5.4 for random and ordered Y^{3+} distribution in YSZ, are anisotropic in nature. Since the Y^{3+} arrangement in x and y - directions are identical for $S1$ to $S3$, thus the MSDs in these directions are *ideally* overlapping. In the case of $S4$ and $S5$, the unique axis is x- axis, thus the Y^{3+} arrangement in y and z- directions are identical, and their corresponding MSD are overlapping. For the $S1$ structure, MSD is completely flat along the z-direction suggesting no oxygen diffusion in the direction. However, the MSD along x and y- directions show marginal slopes indicative of sluggish oxygen transport. Like $S1$, the structure labeled $S2$ also exhibits a flat MSD along the z-axis, but has a noticeable slope along the x and y-directions. The oxygen diffusion in the $S3$-structure shows an overall improvement, with an appreciable slope also along the z-axis, though lower than that along x and y-directions. The diffusivity is substantially increasing along the unique axis (x-axis) in $S4$ whereas the R structure shows nearly isotropic diffusion along all three crystallographic axes. Furthermore, as the directional MSDs of $S4$ and R are overlapping, an expanded view of the directional MSDs of $S4$ and R is shown in Figure 5.4. The $S4$ and $S5$-structures also follow this overall upward trend, suggesting that channels along the *unique*-axis gradually turns favorable for oxygen diffusion. Nonetheless, the most important observation is that we can have Y^{3+}-ordered structure ($S5$) that is much better conducting than the randomly dispersed ones (R).

For better insights into the nature of oxygen diffusion in these differently Y^{3+}-ordered $Y_xZr_{1-x}O_{2-x/2}$ structures, the oxygen trajectories are collapsed onto the entire simulation cell (consisting of $8 \times 8 \times 8$ unit cells), from which one oxygen layer (having a thickness of half the unit cell) sandwiching two cation layers is screened out. Shown in Figure 5.5, the distribution of oxygens (red dots) in the

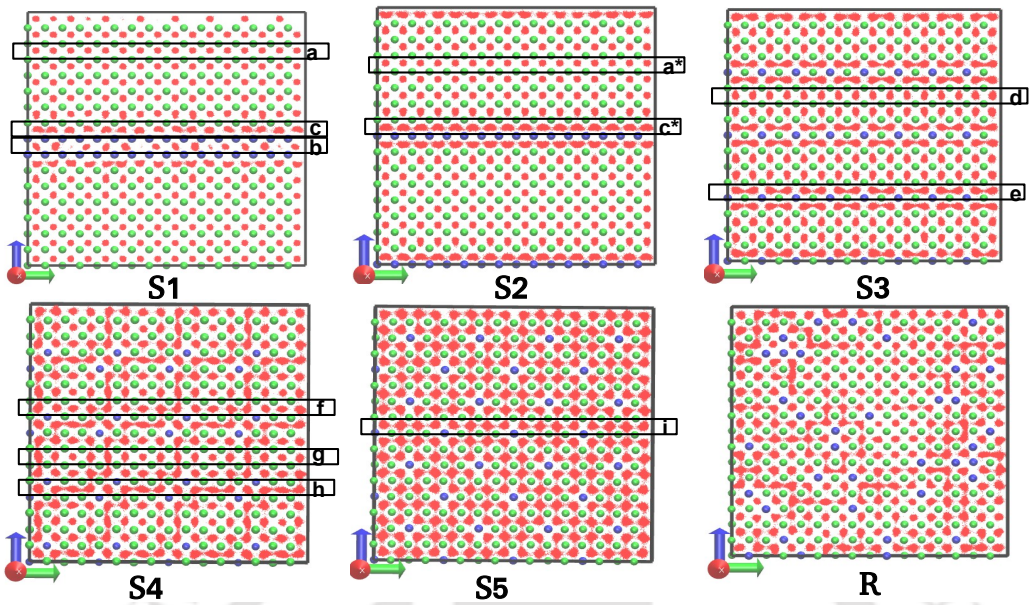

Figure 5.5: The distribution of a mono-layer of oxygen ions in the simulation cell for the differently ordered YSZ matrices are shown by red dots, for Y^{3+} concentration of x=12.5 mol%. These are generated by projecting the entire dynamical trajectory at 1300 K onto the yz-plane (that is, perpendicular to the Y^{3+}stacked layers) and skimming out one mono-layer (of half-unit cell thickness). The blue and green balls are respectively the locations of the Y^{3+} and Zr^{4+} cations. Certain select blocks having distinct local cationic environments are marked a, b, up to i for examination of oxygen distribution on the xy-plane. Blocks that are distinct in a given structure but have close similarities elsewhere are indicated with an asterisk.

system on the yz -plane, gives a qualitative idea of the oxygen migration in different local environments of the matrix. For some of the distinct regions marked, a, b, c, etc. in Figure 5.5, the distribution of oxygen on the xy-plane are demonstrated in Figure 5.6.

In the $S1$ structure, the oxygen distributions are poorly connected along the z-axis (that is, perpendicular to the stacked Y^{3+}- layers). However, in the region marked $S1c$, where the oxygens are sandwiched between Y^{3+}/Zr^{4+} layers the oxygen distributions are better connected along the xy-direction (see Figure 5.6), than the region $S1b$, which is confined between a pair of Y^{3+} layers and $S1a$, which is confined between two Zr^{4+} layers. As evident in Figure 5.5 and Figure 5.6 the Zr^{4+} rich regions marked by $S1a$, and $S2a^*$, respectively in $S1$ and $S2$-structures, significantly localize the oxygens in all three directions hampering ion transport. This reflects the negligible oxygen diffusivity of $S1$ and $S2$ structures along the z-direction. The increase in the diffusivity of $S2$ structure over $S1$ on the basal plane results from two factors, the improvement in the oxygen distribution (see Figure 5.6) in the $S2c^*$

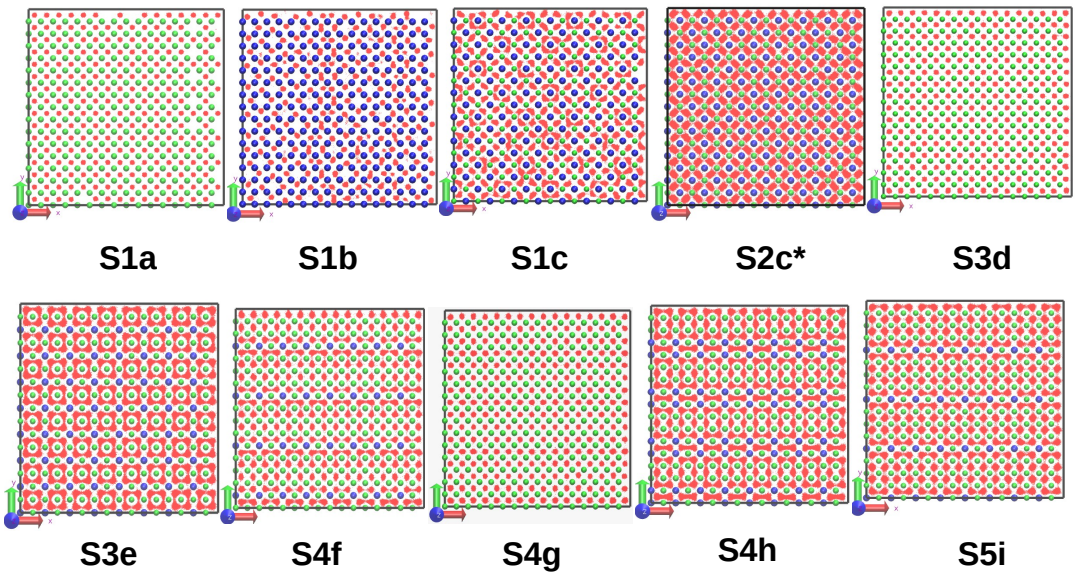

Figure 5.6: The distribution of oxygen ions on the xy-plane of the simulation cell (that is, parallel to the Y^{3+} stacked planes) for the select blocks marked in Figure 5.5.

layer (which is sandwiched between Y^{3+}/Zr^{4+} layers, and thus comparable to layer $S1c$ for its immediate local cationic arrangement), and to the multiplication in the number of $S1c$ or $S2c^*$-like layers in $S2$.

As noted in $S1$ and $S2$ structures in Figure 5.5, full layers Y^{3+} or Zr^{4+} restrict oxygen penetration across them. However, as the layers are getting sparse, the oxygen connectivity improves along the z-axis. It shall be further noted that in $S1$ and $S2$-structures, the oxygen distributions sandwiched between two Zr^{4+} layers but having a Y^{3+} layer adjacent to it, develops a tail *towards* the Y^{3+} locations. Again, in blocks marked $S3d$, where again the oxygens are sandwiched between two Zr^{4+} layers, like the $S1a$ and $S2a^*$-blocks (of the $S1$ and $S2$), the oxygen distribution progressively gets better connected along the z-direction, though the profile on the xy-plane is largely the same (see, $S3$d and $S4$g in Figure 5.6). This indicates that the presence of Y^{3+}, presumably at the second neighbor distance to oxygen sites plays a critical role in promoting mobility. This effect gets more pronounced as we move on to other structures, from S3 to S5, where the Y^{3+} layers are progressively more finely dispersed along the z-axis (at the expense of Y^{3+} coverage per layer). This explains the systematic improvement in the oxygen diffusion observed in Figure 5.4. As noted earlier $S1$ and $S2$-structures, the oxygens sandwiched between Y^{3+}/Zr^{4+}-planes have better mobility on the xy-plane. As we move along the series increasing the number of Y^{3+}-layers stacked along the z axis, reducing Y^{3+} coverage per layer,

the number of mobile oxygen gets multiplied.

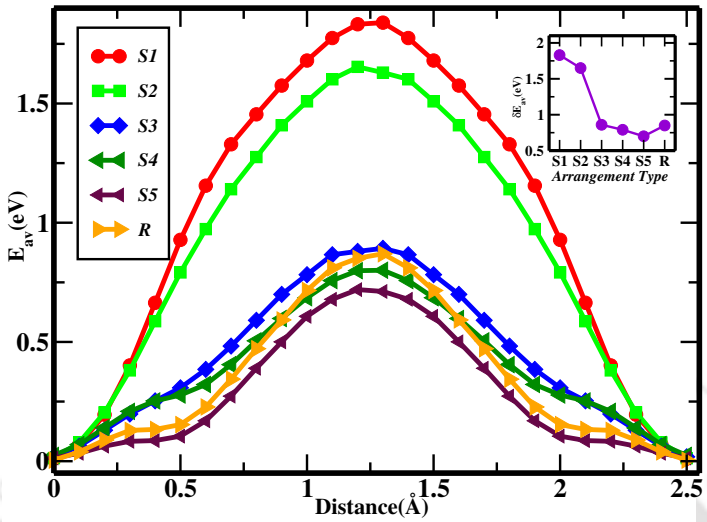

Figure 5.7: The computed average microscopic energy profile, all through the diffusion paths for oxygen hops at 1300K for a dopant concentration of x =12.5% containing both cationic ordered and random configurations of dopant. The inset shows the variation of the barrier across the structures.

Figure 5.7 shows the statistically averaged barrier profile for oxygen ion, ignoring the direction of oxygen ion hop and the nature of the local oxygen environment. The inset in Figure 5.7 shows barrier height variation across these matrices. Notably, the average energy barriers appear to be sensitive to the arrangement of Y^{3+} within the matrix. This implies that increased Y^{3+} dispersion in the matrix results in a lower average energy barrier for oxygen migration. Furthermore, as the Y^{3+} dispersion increases in the matrix an additional hump emerges in the energy profiles (see $S3$ to $S5$ and R structures in Figure 5.7). This is attributed to a higher degree of ion-ion repulsion resulting in a knock-out mechanism as discussed in the previous chapter.

As detailed in the previous Chapter, five different kinds of oxygen sites (denoted by Y_0, Y_1, Y_2, Y_3, and Y_4) are in general possible depending on the number Y^{3+} around a given site. As demonstrated earlier, the site-energies increase with the index of the site, with Y_0 exhibiting the lowest energy and maximum accessibility, while Y_4 highest in energy with the lowest probable occupancy. Similar energetics and accessibility patterns are observed in the present case of cation-ordered structures, $S1$ to $S5$, too (not shown). Further, it was noted in Chapter 4 that Zr-Zr offers the lowest saddle point (energy barrier) for ion hops, while Zr-Y and Y-Y edges pose prohibitively high barriers. The increase in the number of higher-energy (higher-indexed) sites in the matrix results in a proportionate increase in the high-energy

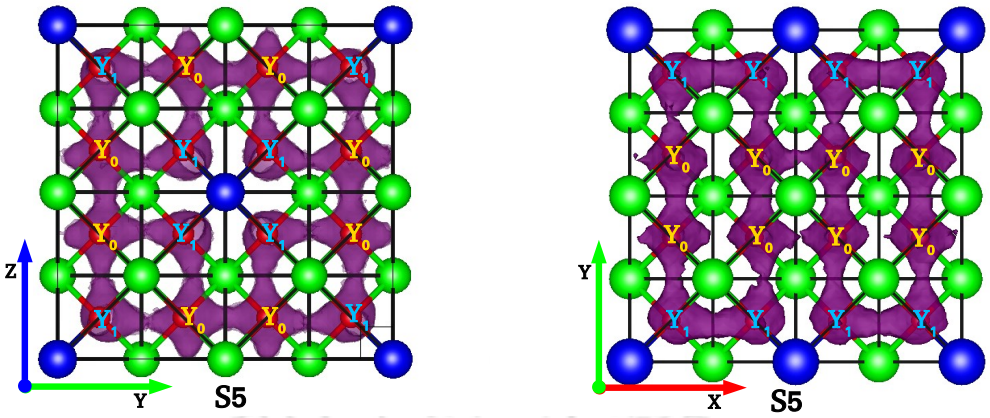

Figure 5.8: The spatial density distribution of oxygen ions across four unit cells with varying Y_0 and Y_1 arrangements is depicted for a single iso-density value in the fluorite-structured YSZ (the xy and yz-plane of $S5$). The green colored spheres represent Zr^{4+} cation sites, while blue spheres indicate Y^{3+} cation sites.

edges too. Thus reduction in the number of Y_2, Y_3 and Y_4-sites have a compounding effect on reducing the effective energy barriers for ion hops. Additionally, the edges were noted to be sensitive to the channel ($Y_0 - Y_0$, $Y_0 - Y_1$, $Y_1 - Y_1$, etc.), involving the departing and destination sites of oxide ions. While these observations noted previously remain grossly applicable, it is noticed in the present study that oxygen migration is influenced beyond the first nearest cation environment, marking their neighboring tetrahedral environments also significant. In other words, the cationic environment up to the second neighboring environment of both departing and destination sites turns out to be significant.

These aspects shall be revisited for the cation ordered $Y_xZr_{1-x}O_{2-x/2}$, but restricting to the $S5$ structure for the sake of brevity. The $S5$ structure has only two types of sites, Y_0 and Y_1. The spatial density distribution of oxygen ions (presented in Figure 5.8) in different planes in the $S5$ structure provides insights into the nature of oxygen migration pathways. It shall be noted that all the six channels emerging from a Y_0 have Zr-Zr edges, while three out of six channels emerging from the Y_1 have Zr-Y edges. It is seen that all the Zr-Y edges are depleted of oxygen density demonstrating that these edges are unfavorable for oxygen transport both in $Y_0 - Y_1$ and $Y_1 - Y_1$ channels. Further, it shall be noted Figure 5.8 that oxygen migration along the Zr-Zr edges are favorable, but only in the vicinity of the Y^{3+}. In fact, the oxygen density is also influenced by the directional nature of the Zr-Zr edges, wherein higher oxygen density is observed at edges when the channel is directed towards a neighboring Y^{3+} cation. These aspects shall also be looked at in terms of

the statistics of transport and energy barriers along the channel.

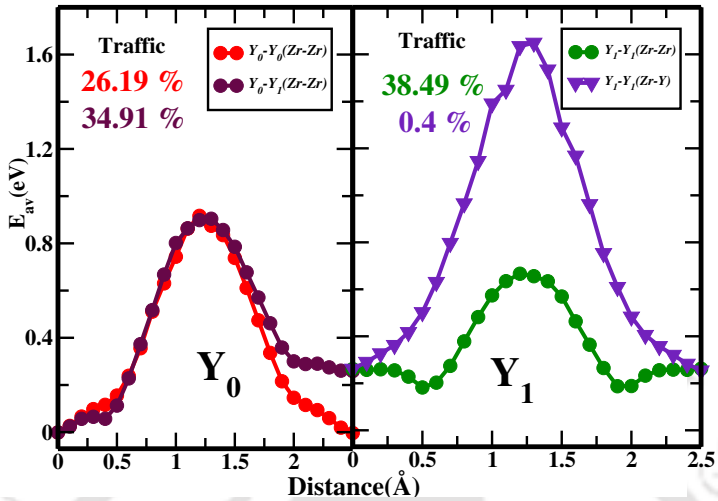

Figure 5.9: Energy barriers for oxygen migration were calculated for all possible cation-cation edge connecting the departure and arrival tetrahedral sites of all the variety migrating channels in the $Y_xZr_{1-x}O_{2-x/2}$ for the $S5$ structure using NPT-MD simulation at 1300 K. Estimated traffic through each channel (in %) is shown on the left side of each panel and is shown in the same color.

Figure 5.9 illustrates the energy barriers along the channels, resolved in terms of their cationic edges of the $S5$ structure. The profile of $Y_0 - Y_1$ channel suggests that the Y_1 sites are higher in energy by $0.26eV$ over the Y_0 sites. It is seen that compared to Zr–Zr edges, the Zr–Y edges have a significantly higher energy barrier. Consequently, Zr-Y accounts for only a negligible fraction (0.4%) of traffic in the corresponding channels. These findings are consistent with the spatial density distribution of oxygen ions in Figure 5.8. Furthermore, it is seen that the energy barrier at the Zr–Zr edges decreases considerably for the $Y_1 - Y_1$ channel due to its vicinity to Y^{3+}, as theorized earlier. Due to the higher energy of the Y_1 sites, the oxygen occupancy at these sites reduces slightly. Consequently, the oxygen vacancies tend to cluster around the Y_1 sites in a dynamic fashion. Thus the observed enhancement in oxygen mobility in the $S5$-structure is attributed to the generation of oxygen vacancies evenly across the matrix, consequent of the maximal dispersion of Y^{3+}.

The above discussion indicates that maximizing the Y^{3+} distribution in the matrix facilitates oxygen mobility. To characterize the cation-ordered $Y_xZr_{1-x}O_{2-x/2}$ structures in terms of the degree of Y^{3+} dispersion in the matrices, the Y^{3+} coordination number around the Y_0 sites ($C_{Y_0}^{Y^{3+}}(r)$) are calculated (see left panel of Figure 5.10). On the right panel in Figure 5.10 the net mean squared displacements

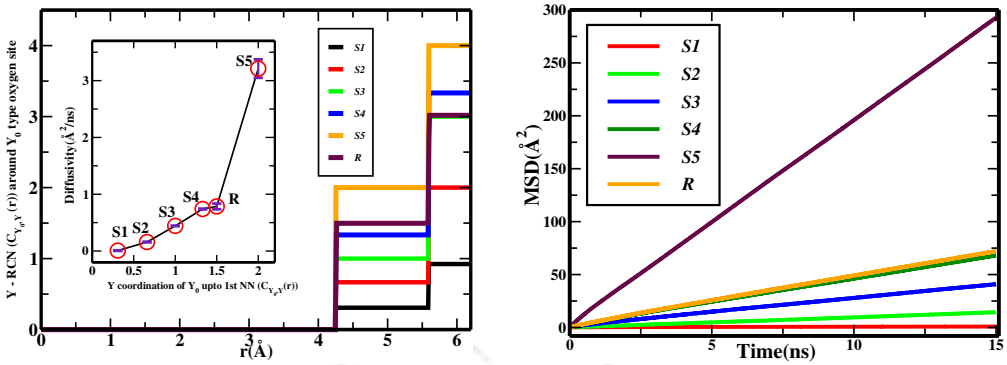

Figure 5.10: *Left panel:* The Y^{3+} co-ordination number with respect to the Y_0 sites $C_{Y_0}^{Y^{3+}}(r)$ for both the ordered and random structure of $Y_xZr_{1-x}O_{2-x/2}$. The inset suggests that the self-diffusivity of oxygen ions (red) is correlated to the $C_{Y_0}^{Y^{3+}}(r)$. The black lines are only for visual guides. The error bars for the self-diffusivity are calculated using the method of "block" averages. *Right panel:* The net mean square displacement (MSD) of oxygen ions in YSZ for different Y^{3+} ordering compared with the random structure from a 30 ns of NPT-MD simulation at 1300K, for the dopant concentration of x = 12.5 mol%.

(MSD), $R^2(t) = R_x^2(t) + R_y^2(t) + R_z^2(t)$, of these structures are shown. We observe that the Y^{3+} coordination number around the Y_0 sites ($C_{Y_0}^{Y^{3+}}(r)$) serves a good "order parameter" to define the Y^{3+} dispersion in the cation ordered $Y_xZr_{1-x}O_{2-x/2}$-structures $S1$ to $S5$, and R. This is illustrated in the inset of the left panel of Figure 5.10, wherein the total self-diffusivity of oxygens is found increase with the proposed order-parameter ($C_{Y_0}^{Y^{3+}}(r)$).

5.4 Summary and Conclusion

The findings presented here demonstrate that the ordered and random configurations of Zr^{4+} and Y^{3+} ions in yttria-stabilized zirconia (YSZ) have a significant impact on the transport of oxide ions within the framework. A classical MD simulation is performed on YSZ ($Y_xZr_{1-x}O_{2-x/2}$) at a temperature of 1300 K in an isothermal-isobaric (NPT) ensemble with x = 12.5 mol%. After verifying the underlying structural stability of the simulated framework through lattice parameter variation and radial distribution function (RDF), we analyzed the dynamical properties of the oxide ions in YSZ. It has been shown that the ordered structure $S5$ has the highest diffusivity compared to other ordered and random structures with the same composition x =12.5 mol%. Thus, for a given composition, the ion transportation in YSZ increases with increasing Y^{3+} dispersion in the matrix. This assertion is further supported by the variation in potential energy barriers across different

cationic arrangements ($S1$ to $S5$, and R), as well as the coordination number (Y^{3+} coordination) around Y_0 sites ($C_{Y_0}^{Y^{3+}}(r)$), which also serves as an order parameter for the dispersion of Y^{3+} within the matrix. The spatial density distribution of oxygen ions and the energy barriers along all the cationic edges (Zr-Zr and Zr-Y) in the highest conductive $S5$ structure are examined. The findings suggest that the presence of Y^{3+} (as Y_1 sites) in the vicinity of Y_0 sites (fully Zr^{4+}decorated tetrahedral holes) indirectly facilitates ion hops. This also indicates that the oxygen vacancies, primarily located at the Y_1 sites, provide a temporary "stop-over" for oxygen ions. As a result, the highest diffusivity of the $S5$ structure is attributed to the uniform distribution of Y_1 sites, which ensures consistent availability of oxygen vacancies throughout the matrix. Furthermore, this research suggests that the ionic conductivity of YSZ materials can be significantly improved through the implementation of various controlled synthesis routes such as atomic layer deposition (ALD), pulsed laser deposition (PLD), and so on.

Chapter 6

Summary and Outlook

Fuel cells are renewable energy devices that convert chemical energy directly into electricity without combustion, offering a clean and sustainable power source. Among all the fuel cell varieties, SOFCs stand out due to their fuel flexibility, high operating temperatures, enhanced durability with a solid ceramic electrolyte, and versatility for stationary and mobile applications. To promote the extensive commercial adoption of SOFCs, it is crucial to conduct further scientific investigations and make performance improvements in SOFC technology. In SOFCs, electrolyte is the vital component, facilitating the movement of ions between the anode and cathode during electricity generation. For its commercial viability the electrolyte of SOFCs should possess essential properties including high ionic conductivity, good chemical and thermal stability, compatibility with electrodes, negligible electronic conductivity, and cost-effectiveness. Although no electrolyte material synthesized thus far fully meets all the desired characteristics, ZrO_2 and CeO_2-based electrolyte materials have been realized to be very promising.

The thesis aims to provide fresh perspectives on the microscopic mechanism of ion transport in yttria doped ceria and zirconia, utilizing molecular dynamics (MD) simulations. Chapter 1 of the thesis, provides a concise literature review of various materials used as cathodes, anodes, and electrolytes in SOFCs. An in-depth survey of electrolyte materials across various structural families is presented, emphasizing prior theoretical studies and insights on ZrO_2 and CeO_2-based electrolytes. The theoretical foundations of the computational techniques that are employed in the studies detailed in subsequent chapters are outlined in Chapter 2 of the thesis.

In Chapter 3, NPT-MD simulations are conducted on yttria-doped ceria (YDC) over a range of dopant concentrations (x = 4 to 40 mol%) at 1300 K. The cell parameter of YDC consistently decreases as the yttrium concentration increases,

aligning with previous theoretical and experimental observations. This pattern is attributed to the smaller ionic radii and lower charge of Y^{3+} ions compared to Ce^{4+}, resulting in a reduced repulsion between cations. The investigation reveals that the self-diffusivity of oxygen ions in YDC peaks at $x = 14$ mol% dopant concentration, consistent with earlier theoretical and experimental findings. The study observes that oxide ions occupy tetrahedral holes in the face-centered cubic (fcc) cationic sub-lattice, migrating along the straight channels parallel to crystallographic axes for long-range transport. The observed variation in ionic conductivity correlates with the non-monotonic changes in the residence time of oxygen ions in tetrahedral holes. Five distinct oxygen sites (Y_0 to Y_4) are identified based on the number of surrounding yttrium ions at the tetrahedra corners. The potential energy of oxygen ions at those sites increases as the number of yttrium ions at the tetrahedral corner increases, making these sites less favourable. Along with yttrium content, the energy barriers along various channels connecting higher-indexed sites also increases. Consequently, at lower concentrations of yttrium, oxygen vacancies facilitate ion hops between neighboring sites. However, with further yttrium doping, the fraction of higher-barrier channels in the matrix increases, impeding ion transport. The statistically averaged microscopic energy barriers for oxygen migration exhibit a distinct minimum at the highest conducting composition, $x = 14$ mol% yttrium doping, providing an explanation for the non-monotonic variations in oxygen diffusivity with concentration.

In Chapter 4, NPT-MD simulations are employed to investigate the structural and dynamic properties of yttria-stabilized zirconia (YSZ) over a wide range of dopant concentrations ($x = 4$ to 40 mol%) and temperatures ranging from 800 to 2200 K. At 1300 K, the study confirms that the self-diffusivity of oxygen ions in YSZ peaks at $x = 10$ mol% yttrium doping, supporting previous theoretical and experimental findings. The activation energies, derived from the Arrhenius plot of conductivity, show good agreement with existing literature. Similar to YDC, the oxygen ion migration pathway in YSZ is parallel to the crystallographic axis due to their similar crystal structures, as explained in Chapter 3. As the yttrium content of the environment increases, the potential energy of oxygen sites increases, reducing the probabilistic occupancy of these sites. The further investigation focuses on the energetic characteristics of the channels connecting oxygen sites, particularly along various cationic edges such as Zr-Zr, Zr-Y, and Y-Y. Notably, compared to the Zr-Zr edges, the oxygen migration barriers along the Zr-Y and Y-Y edges are significantly higher. As a result, the low oxygen diffusivity at higher compositions

(above $x = 10$ mol%) can be attributed to an increase in high-energy sites and energetically unfavorable cationic edges, such as Zr-Y and Y-Y, in the matrix. The study also observed signatures of a certain degree of oxygen-oxygen correlations in YSZ materials, particularly at low concentrations of yttria.

In Chapter 5, we examine how cationic (Zr^{4+}/Y^{3+}) distribution impacts oxide ion transport in the YSZ matrix. The mobility of oxide ions in five cationically (Zr/Y) differently-ordered structures and compared the same with Y^{3+}-randomly distributed structure. The calculations are done at temperature 1300 K with a dopant concentration of $x = 12.5$ mol% in the NPT ensemble. The study shows that cationic ordering in the matrix strongly affects oxide-ion diffusion. Interestingly, the more evenly are the Y^{3+} distributed in the matrix the higher is the oxide ion transport in the system. Thus, certain cationic ordered structures produce four times higher oxide ion diffusivity than the random structure. This suggests that the ionic conductivity of YSZ materials could be significantly improved using various controlled synthesis routes such as atomic layer deposition (ALD), pulsed laser deposition (PLD), etc. It is observed that the higher energy of Y_1 sites (one Y^{3+} in the immediate tetrahedral oxygen environment) results in lower oxygen occupancy, and three of the unfavorable Zr-Y edges of such sites hinder the ion migration. However, ion hops are indirectly facilitated by the presence of Y^{3+} (as Y_1 sites) next to Y_0 sites (fully Zr-decorated tetrahedral holes). This involves a complex mechanism where oxygen vacancies, primarily located at the Y_1 sites, act as short 'stop-over' for oxygen ions, promoting transport in their vicinity. Thus, an even distribution of Y^{3+} (generating Y_1 sites), which ensures a uniform availability of oxygen vacancies across the matrix, is ascribed to the calculated high diffusivity. It is proposed that the Y^{3+} coordination number with respect to the Y_0 sites can be identified as an order parameter for oxygen diffusivity in the matrix.

This thesis brings out fresh insights on the microscopic nature of oxide ion transport in $Y_xCe_{1-x}O_{2-x/2}$ and $Y_xZr_{1-x}O_{2-x/2}$ materials, identifies certain factors that govern ion mobility, and proposes plausible experimental strategies for improving the ionic conductivity of samples.

Bibliography

[1] K. Tang, M. Wang and D. Zhou, *Environ. Sci. Pollut. Res.*, 2021, **28**, 21862–21873.

[2] G. P. Peters, R. M. Andrew, J. G. Canadell, P. Friedlingstein, R. B. Jackson, J. I. Korsbakken, C. Le Quéré and A. Peregon, *Nature Clim. Change*, 2020, **10**, 3–6.

[3] S. E. Hosseini, M. A. Wahid and N. Aghili, *Renew. Sust. Energ. Rev.*, 2013, **28**, 400–409.

[4] R. Newell, D. Raimi and G. Aldana, *Resources for the Future*, 2019, **1**, 8–19.

[5] S. Solomon, D. Qin, M. Manning, Z. Chen, M. Marquis, K. Averyt, M. Tignor and H. Miller, *Clim. Change*, 2007, **374**, year.

[6] C. Sturm, *Issues Sci Technol .*, 2017, **33**, 41.

[7] R. Beveridge and K. Kern, *Renewable Energy L. & Pol'y Rev.*, 2013, **4**, 3.

[8] M. Bolinger, 2014.

[9] J. S. Merrifield and S. Fowler, *J. Fusion Energy*, 2023, **42**, 26.

[10] N. Rietmann and T. Lieven, *J. Clean. Prod.*, 2019, **206**, 66–75.

[11] B. K. Sovacool, L. Noel, J. Kester and G. Z. de Rubens, *Energy*, 2018, **165**, 532–542.

[12] P. K. Tarei, P. Chand and H. Gupta, *J. Clean. Prod.*, 2021, **291**, 125847.

[13] C.-J. Winter, *Int. J. Hydrog. Energy*, 2009, **34**, S1–S52.

[14] N. Sazali, *Int. J. Hydrog. Energy*, 2020, **45**, 18753–18771.

[15] M. K. Singla, P. Nijhawan and A. S. Oberoi, *Environ. Sci. Pollut. Res.*, 2021, **28**, 15607–15626.

[16] M. Momirlan and T. N. Veziroglu, *Int. J. Hydrog. Energy*, 2005, **30**, 795–802.

[17] J. Andrews and B. Shabani, *Int. J. Hydrog. Energy*, 2012, **37**, 1184–1203.

[18] S. E. Hosseini, *Int. J. Green Energy*, 2023, 1–17.

[19] S. Ma, M. Lin, T.-E. Lin, T. Lan, X. Liao, F. Maréchal, Y. Yang, C. Dong, L. Wang *et al.*, *Renew. Sust. Energ. Rev.*, 2021, **135**, 110119.

[20] S. G. Chalk and J. F. Miller, *J. Power Sources*, 2006, **159**, 73–80.

[21] A. B. Stambouli, *Renew. Sust. Energ. Rev.*, 2011, **15**, 4507–4520.

[22] M. A. Abdelkareem, K. Elsaid, T. Wilberforce, M. Kamil, E. T. Sayed and A. Olabi, *Science of The Total Environment*, 2021, **752**, 141803.

[23] R.-A. Felseghi, E. Carcadea, M. S. Raboaca, C. N. Trufin and C. Filote, *Energies*, 2019, **12**, 4593.

[24] A. Dehghani-Sanij, E. Tharumalingam, M. Dusseault and R. Fraser, *Renew. Sust. Energ. Rev.*, 2019, **104**, 192–208.

[25] A. Z. A. Shaqsi, K. Sopian and A. Al-Hinai, *Energy Reports*, 2020, **6**, 288–306.

[26] M. M. Thackeray, C. Wolverton and E. D. Isaacs, *Energy Environ. Sci.*, 2012, **5**, 7854–7863.
[27] M. R. Palacín and A. de Guibert, *Science*, 2016, **351**, 1253292.
[28] U. Eberle and R. von Helmolt, *Electric and hybrid vehicles*, 2010, **9**, 227–245.
[29] C. Cunanan, M.-K. Tran, Y. Lee, S. Kwok, V. Leung and M. Fowler, *Clean Technologies*, 2021, **3**, 474–489.
[30] A. Ajanovic and R. Haas, *Fuel cells*, 2019, **19**, 515–529.
[31] A. Pramuanjaroenkij and S. Kakaç, *Int. J. Hydrog. Energy*, 2023, **48**, 9401–9425.
[32] B. Sorensen and G. Spazzafumo, 2018.
[33] G. Gahleitner, *Int. J. Hydrog. Energy*, 2013, **38**, 2039–2061.
[34] M. Lamagna, D. Groppi and B. Nastasi, *Int. J. Hydrog. Energy*, 2023.
[35] X. Wang, J. Zhu and M. Han, *J. Mar. Sci. Eng.*, 2023, **11**, 238.
[36] V. K. Visvanathan, K. Palaniswamy, D. Ponnaiyan, M. Chandran, T. Kumaresan, J. Ramasamy and S. Sundaram, *Energies*, 2023, **16**, 2748.
[37] Y. Wang, Y. Pang, H. Xu, A. Martinez and K. S. Chen, *Energy Environ. Sci.*, 2022, **15**, 2288–2328.
[38] H. Tuofu, H. Changhao, H. Qingyun, Y. Dongxiao, H. Tian and F. Yi, *Int. J. Hydrog. Energy*, 2022, **47**, 24493–24510.
[39] L. Giorgi and F. Leccese, *The Open Fuel Cells Journal*, 2013, **6**, year.
[40] C.-Y. Wang, *Chemical reviews*, 2004, **104**, 4727–4766.
[41] S. Shamim, K. Sudhakar, B. Choudhary and J. Anwar, *Advances in Applied Science Research*, 2015, **6**, 89–100.
[42] D. Stolten and B. Emonts, *Fuel Cell Science and Engineering, 2 Volume Set: Materials, Processes, Systems and Technology*, John Wiley & Sons, 2012, vol. 1.
[43] H.-H. Möbius, *J. Solid State Chem.*, 1997, **1**, 2–16.
[44] J. M. Andújar and F. Segura, *Renew. Sust. Energ. Rev.*, 2009, **13**, 2309–2322.
[45] R. Raccichini and U. Ulissi, *Nanomaterials for Electrochemical Energy Storage: Challenges and Opportunities;Elsevier*, 2021.
[46] W. R. Grove, *The London, Edinburgh, and Dublin Philosophical Magazine and Journal of Science*, 1839, **14**, 127–130.
[47] S. Kartha and P. Grimes, *Phys. Today*, 1994, **47**, 54–61.
[48] A. L. Dicks and D. A. Rand, *Fuel cell systems explained*, John Wiley & Sons, 2018.
[49] S. V. M. Guaitolini, I. Yahyaoui, J. F. Fardin, L. F. Encarnação and F. Tadeo, 2018 9th International renewable energy congress (IREC), 2018, pp. 1–6.
[50] A. Kirubakaran, S. Jain and R. Nema, *Renew. Sust. Energ. Rev.*, 2009, **13**, 2430–2440.
[51] N. Sazali, W. N. Wan Salleh, A. S. Jamaludin and M. N. Mhd Razali, *Membranes*, 2020, **10**, 99.
[52] L. Carrette, K. A. Friedrich and U. Stimming, *ChemPhysChem*, 2000, **1**, 162–193.
[53] S. Mekhilef, R. Saidur and A. Safari, *Renew. Sust. Energ. Rev.*, 2012, **16**, 981–989.
[54] L. van Biert, M. Godjevac, K. Visser and P. Aravind, *J. Power Sources*, 2016, **327**, 345–364.

[55] C. Song, *Catalysis today*, 2002, **77**, 17–49.
[56] J. R. Varcoe and R. C. Slade, *Fuel cells*, 2005, **5**, 187–200.
[57] Y. Shao, G. Yin, Z. Wang and Y. Gao, *J. Power Sources*, 2007, **167**, 235–242.
[58] N. Sammes, R. Bove and K. Stahl, *Current opinion in solid state and materials science*, 2004, **8**, 372–378.
[59] R. Remick and D. Wheeler, *National Renewable Energy Lab.(NREL), Golden, CO (United States)*, 2010.
[60] A. Mehr, A. Lanzini, M. Santarelli and M. A. Rosen, *Energy*, 2021, **228**, 120613.
[61] T. Coppola, L. Micoli and M. Turco, 2020 International Symposium on Power Electronics, Electrical Drives, Automation and Motion (SPEEDAM), 2020, pp. 430–435.
[62] M. Irshad, K. Siraj, R. Raza, A. Ali, P. Tiwari, B. Zhu, A. Rafique, A. Ali, M. Kaleem Ullah and A. Usman, *Appl. Sci.*, 2016, **6**, 75.
[63] M. L. Perry and T. F. Fuller, *J. Electrochem. Soc.*, 2002, **149**, S59.
[64] F. de Bruijn, *Green Chem.*, 2005, **7**, 132–150.
[65] R. M. Ormerod, *Chem Soc Rev*, 2003, **32**, 17–28.
[66] M. Singh, D. Zappa and E. Comini, *Int. J. Hydrog. Energy*, 2021, **46**, 27643–27674.
[67] S. C. Singhal, *Wiley Interdisciplinary Reviews: Energy and Environment*, 2014, **3**, 179–194.
[68] A. M. Abdalla, S. Hossain, A. T. Azad, P. M. I. Petra, F. Begum, S. G. Eriksson and A. K. Azad, *Renew. Sust. Energ. Rev.*, 2018, **82**, 353–368.
[69] S. Badwal, S. Giddey, C. Munnings and A. Kulkarni, *ChemInform*, 2015, **46**, no–no.
[70] I. Dincer and C. Acar, *Int. J. Energy Res.*, 2015, **39**, 585–606.
[71] G. Chasta, Himanshu and M. S. Dhaka, *Int. J. Energy Res.*, 2022, **46**, 14627–14658.
[72] P. Knauth and H. L. Tuller, *J. Am. Ceram. Soc.*, 2002, **85**, 1654–1680.
[73] W. Heraeus, *Zeitschrift für Elektrochemie*, 1899, **6**, 41–43.
[74] A. J. Appleby, 1988.
[75] H. Charlton, G. Baldinozzi and M. Patel, *Front. Nucl. Eng.*, 2023, **1**, 1096142.
[76] E. Baur and H. Preis, *Zeitschrift für Elektrochemie und angewandte physikalische Chemie*, 1937, **43**, 727–732.
[77] A. B. Stambouli and E. Traversa, *Renew. Sust. Energ. Rev.*, 2002, **6**, 433–455.
[78] L. Fan, B. Zhu, P.-C. Su and C. He, *Nano Energy*, 2018, **45**, 148–176.
[79] K. Huang and J. B. Goodenough, *Solid oxide fuel cell technology: principles, performance and operations,Elsevier*, 2009.
[80] B. C. Steele, *Curr Opin Solid State Mater Sci .*, 1996, **1**, 684–691.
[81] V. Thangadurai and W. Weppner, *Ionics*, 2006, **12**, 81–92.
[82] K. Huang, J. Wan and J. B. Goodenough, *J. Mater. Sci.*, 2001, **36**, 1093–1098.
[83] F. Lefebvre-Joud, G. Gauthier and J. Mougin, *J. Appl. Electrochem.*, 2009, **39**, 535–543.
[84] L. Bi, E. H. Da'as and S. P. Shafi, *Electrochem. commun.*, 2017, **80**, 20–23.
[85] I. T. Bello, S. Zhai, S. Zhao, Z. Li, N. Yu and M. Ni, *Int. J. Hydrog. Energy*, 2021, **46**, 37406–37428.
[86] F. S. Da Silva and T. M. de Souza, *Int. J. Hydrog. Energy*, 2017, **42**, 26020–26036.

[87] S. Hussain and L. Yangping, *Energy Transitions*, 2020, **4**, 113–126.
[88] P. S. Devi, A. D. Sharma and H. S. Maiti, *Trans. Indian Ceram. Soc.*, 2004, **63**, 75–98.
[89] N. Mahato, A. Banerjee, A. Gupta, S. Omar and K. Balani, *Prog. Mater. Sci.*, 2015, **72**, 141–337.
[90] S. Dwivedi, *Int. J. Hydrog. Energy*, 2020, **45**, 23988–24013.
[91] K. Kendall, *International materials reviews*, 2005, **50**, 257–264.
[92] J. Xu, R. Sakanoi, Y. Higuchi, N. Ozawa, K. Sato, T. Hashida and M. Kubo, *J. Phys. Chem. C*, 2013, **117**, 9663–9672.
[93] S. Suthirakun, G. Xiao, S. C. Ammal, F. Chen, H.-C. zur Loye and A. Heyden, *J. Power Sources*, 2014, **245**, 875–885.
[94] W. Zhu and S. Deevi, *Mater. Sci. Eng.: A*, 2003, **362**, 228–239.
[95] R. J. Gorte, J. M. Vohs and S. McIntosh, *Solid State Ionics*, 2004, **175**, 1–6.
[96] M. Rafique, H. Nawaz, M. Shahid Rafique, M. Bilal Tahir, G. Nabi and N. Khalid, *Int. J. Energy Res.*, 2019, **43**, 2423–2446.
[97] M. Shishkin and T. Ziegler, *Phys. Chem. Chem. Phys.*, 2014, **16**, 1798–1808.
[98] M. S. Khan, S.-B. Lee, R.-H. Song, J.-W. Lee, T.-H. Lim and S.-J. Park, *Ceram. Int.*, 2016, **42**, 35–48.
[99] Z. Cheng, J.-H. Wang, Y. Choi, L. Yang, M.-C. Lin and M. Liu, *Energy Environ. Sci.*, 2011, **4**, 4380–4409.
[100] A. I. Marquez, Y. De Abreu and G. G. Botte, *J Solid State Electrochem .*, 2006, **9**, A163.
[101] B. Hwang, H. Kwon, J. Ko, B.-K. Kim and J. W. Han, *Appl. Surf. Sci.*, 2018, **429**, 87–94.
[102] S. Vafaeenezhad, A. R. Hanifi, M. A. Laguna-Bercero, T. H. Etsell and P. Sarkar, *Materials Futures*, 2022.
[103] Y. Akdeniz, B. Timurkutluk and C. Timurkutluk, *Int. J. Hydrog. Energy*, 2016, **41**, 10021–10029.
[104] S. H. Lee and H. Kim, *Ceram. Int.*, 2014, **40**, 5959–5966.
[105] A. Singh and J. M. Hill, *ECS Trans.*, 2011, **35**, 1397.
[106] Q. Bkour, F. Che, K.-M. Lee, C. Zhou, N. Akter, J. A. Boscoboinik, K. Zhao, J. T. Gray, S. R. Saunders, M. G. Norton *et al.*, *Applied Catalysis B: Environmental*, 2020, **266**, 118626.
[107] X. Wu, X. Zhou, Y. Tian, X. Kong, J. Zhang, W. Zuo, X. Ye and K. Sun, *Int. J. Hydrog. Energy*, 2015, **40**, 16484–16493.
[108] F.-Y. Wang, G.-B. Jung, A. Su, S.-H. Chan, X. Hao and Y.-C. Chiang, *J. Power Sources*, 2008, **185**, 862–866.
[109] G. Kaur and S. Basu, *ECS Trans.*, 2013, **57**, 2961.
[110] R. J. Gorte, H. Kim and J. M. Vohs, *J. Power Sources*, 2002, **106**, 10–15.
[111] K. Matsumoto, Y. Tachikawa, S. M. Lyth, J. Matsuda and K. Sasaki, *Int. J. Hydrog. Energy*, 2022, **47**, 29441–29455.

[112] I. Unal, S. Meisuria, M. Choolaei, T. R. Reina and B. A. Horri, *Ceram. Int.*, 2018, **44**, 6851–6860.
[113] E. Putna, J. Stubenrauch, J. Vohs and R. Gorte, *Langmuir*, 1995, **11**, 4832–4837.
[114] P. I. Cowin, C. T. Petit, R. Lan, J. T. Irvine and S. Tao, *Adv. Energy Mater.*, 2011, **1**, 314–332.
[115] Z. Wang, W. Weng, K. Cheng, P. Du, G. Shen and G. Han, *J. Power Sources*, 2008, **179**, 541–546.
[116] M. Gong, X. Liu, J. Trembly and C. Johnson, *J. Power Sources*, 2007, **168**, 289–298.
[117] S. Zha, Z. Cheng and M. Liu, *J Solid State Electrochem .*, 2005, **8**, A406.
[118] C. Yang, Z. Yang, C. Jin, G. Xiao, F. Chen and M. Han, *Adv Mater.*, 2012, **24**, 1439–1443.
[119] J. B. Goodenough and Y.-H. Huang, *J. Power Sources*, 2007, **173**, 1–10.
[120] H. Kurokawa, L. Yang, C. P. Jacobson, L. C. De Jonghe and S. J. Visco, *J. Power Sources*, 2007, **164**, 510–518.
[121] O. A. Marina, N. L. Canfield and J. W. Stevenson, *Solid State Ionics*, 2002, **149**, 21–28.
[122] S. Zha, P. Tsang, Z. Cheng and M. Liu, *J. Solid State Chem.*, 2005, **178**, 1844–1850.
[123] G. Xiao, Q. Liu, X. Dong, K. Huang and F. Chen, *J. Power Sources*, 2010, **195**, 8071–8074.
[124] K. B. Yoo and G. M. Choi, *Solid State Ionics*, 2011, **192**, 515–518.
[125] I. Rahman, M. Raza and M. Rahman, *Adv Mater. Research*, 2012, **445**, 497–502.
[126] L. Shu, J. Sunarso, S. S. Hashim, J. Mao, W. Zhou and F. Liang, *Int. J. Hydrog. Energy*, 2019, **44**, 31275–31304.
[127] M. B. Hanif, M. Motola, S. Rauf, C.-J. Li, C.-X. Li *et al.*, *Chemical Engineering Journal*, 2022, **428**, 132603.
[128] M. Pidburtnyi, B. Zanca, C. Coppex, S. Jimenez-Villegas and V. Thangadurai, *Chem. Mater.*, 2021, **33**, 4249–4268.
[129] T. H. Shin, S. Ida and T. Ishihara, *J. Am. Chem. Soc.*, 2011, **133**, 19399–19407.
[130] Y.-W. Ju, S. Lee, B. S. Kang, H. H. Kim and T. Ishihara, *Int. J. Hydrog. Energy*, 2019, **44**, 29641–29647.
[131] S. B. Adler, J. Lane and B. Steele, *J. Electrochem. Soc.*, 1996, **143**, 3554.
[132] C. Moure and O. Peña, *Progress in Solid State Chemistry*, 2015, **43**, 123–148.
[133] N. H. Perry and T. Ishihara, *Materials*, 2016, **9**, 858.
[134] W. Bao, H. Guan and J. Cheng, *J. Power Sources*, 2008, **175**, 232–237.
[135] X.-F. Ye, S. Wang, Z. Wang, Q. Hu, X. Sun, T. Wen and Z. Wen, *J. Power Sources*, 2008, **183**, 512–517.
[136] J. H. Kim, D. Miller, H. Schlegl, D. McGrouther and J. T. Irvine, *Chem. Mater.*, 2011, **23**, 3841–3847.
[137] T. Ishihara, S. Fukui, M. Enoki and H. Matsumoto, *J. Electrochem. Soc.*, 2006, **153**, A2085.
[138] W.-X. Kao, M.-C. Lee, Y.-C. Chang, T.-N. Lin, C.-H. Wang and J.-C. Chang, *J.*

Power Sources, 2010, **195**, 6468–6472.
[139] A. C. van Veen, M. Rebeilleau, D. Farrusseng and C. Mirodatos, *Chemical communications*, 2003, 32–33.
[140] C. Harrison, P. Slater and R. Steinberger-Wilckens, *Solid State Ionics*, 2020, **354**, 115410.
[141] Y. Takeda, Y. Sakaki, T. Ichikawa, N. Imanishi, O. Yamamoto, M. Mori, N. Mori and T. Abe, *Solid State Ionics*, 1994, **72**, 257–264.
[142] R. A. De Souza, M. S. Islam and E. Ivers-Tiffée, *J. Mater. Chem.*, 1999, **9**, 1621–1627.
[143] J. Van Herle, A. McEvoy and K. R. Thampi, *Electrochim. Acta*, 1996, **41**, 1447–1454.
[144] W. J. Quadakkers, J. Pirón-Abellán and V. Shemet, *Materials Research*, 2004, **7**, 203–208.
[145] J. Piao, K. Sun, N. Zhang and S. Xu, *J. Power Sources*, 2008, **175**, 288–295.
[146] O. Agbede, K. Hellgardt and G. Kelsall, *Mater. Today Chem.*, 2020, **16**, 100252.
[147] K. Chen, Z. Lü, X. Chen, N. Ai, X. Huang, X. Du and W. Su, *J. Power Sources*, 2007, **172**, 742–748.
[148] S. J. Skinner, *Int. j. inorg. mater.*, 2001, **3**, 113–121.
[149] T.-L. Wen, H. Tu, Z. Xu and O. Yamamoto, *Solid State Ionics*, 1999, **121**, 25–30.
[150] Y. Sakaki, Y. Takeda, A. Kato, N. Imanishi, O. Yamamoto, M. Hattori and Y. Esaki, *J. Jpn. Soc. Powder Powder Metall.*, 1999, **46**, 293–299.
[151] S. Jiang, J. Love and L. Apateanu, *Solid State Ionics*, 2003, **160**, 15–26.
[152] I. Yasuda, Y. Baba, T. Ogiwara, H. Yakabe and Y. Matsuzaki, *ECS Proceedings Volumes*, 2001, **2001**, 131.
[153] G. C. Kostogloudis, N. Vasilakos and C. Ftikos, *J. Eur. Ceram.*, 1997, **17**, 1513–1521.
[154] G. C. Kostogloudis and C. Ftikos, *J. Eur. Ceram.*, 1999, **19**, 497–505.
[155] L.-W. Tai, M. Nasrallah, H. Anderson, D. Sparlin and S. Sehlin, *Solid State Ionics*, 1995, **76**, 273–283.
[156] B. Wei, Z. Lü, X. Huang, J. Miao, X. Sha, X. Xin and W. Su, *J. Eur. Ceram.*, 2006, **26**, 2827–2832.
[157] Y. Wang, H. Nie, S. Wang, T.-L. Wen, U. Guth and V. Valshook, *Mater. Lett.*, 2006, **60**, 1174–1178.
[158] F. Bidrawn, G. Kim, N. Aramrueang, J. Vohs and R. Gorte, *J. Power Sources*, 2010, **195**, 720–728.
[159] W. Zhou, Z. Shao, R. Ran, P. Zeng, H. Gu, W. Jin and N. Xu, *J. Power Sources*, 2007, **168**, 330–337.
[160] L. Guo, L. Bo, Y. Li, Z. Jiang, Y. Tian and X. Li, *Solid State Sci.*, 2021, **113**, 106519.
[161] N. Ortiz-Vitoriano, I. R. de Larramendi, I. G. de Muro, A. Larrañaga, J. I. R. de Larramendi and T. Rojo, *J. Mater. Chem.*, 2011, **21**, 9682–9691.
[162] L. M. Garcia, D. A. Macedo, G. L. Souza, F. V. Motta, C. A. Paskocimas and R. M.

Nascimento, *Ceram. Int.*, 2013, **39**, 8385–8392.
[163] X. Meng, S. Lü, Y. Ji, T. Wei and Y. Zhang, *J. Power Sources*, 2008, **183**, 581–585.
[164] W. Xia, X. Liu, F. Jin, X. Jia, Y. Shen and J. Li, *Electrochim. Acta*, 2020, **364**, 137274.
[165] S. Yoo, A. Jun, Y.-W. Ju, D. Odkhuu, J. Hyodo, H. Y. Jeong, N. Park, J. Shin, T. Ishihara and G. Kim, *Angewandte Chemie*, 2014, **126**, 13280–13283.
[166] F. Jin, Y. Shen, R. Wang and T. He, *J. Power Sources*, 2013, **234**, 244–251.
[167] V. Dusastre and J. A. Kilner, *Solid state ionics*, 1999, **126**, 163–174.
[168] K. Wang, R. Ran, W. Zhou, H. Gu, Z. Shao and J. Ahn, *J. Power Sources*, 2008, **179**, 60–68.
[169] C. Fu, K. Sun, N. Zhang, X. Chen and D. Zhou, *Electrochim. Acta*, 2007, **52**, 4589–4594.
[170] J. Nielsen, T. Jacobsen and M. Wandel, *Electrochim. Acta*, 2011, **56**, 7963–7974.
[171] M. E. Perry, M. Sever and S. Barnett, *Solid State Ionics*, 2002, **148**, 27–34.
[172] X. Fan, C.-Y. You, J.-L. Zhu, L. Chen and C.-R. Xia, *Ionics*, 2015, **21**, 2253–2258.
[173] S. F. Mohammad, S. Ahmad, H. A. Rahman and A. Muchtar, *Int. J. Integr.*, 2019, **11**, 162–168.
[174] A. Chroneos, B. Yildiz, A. Tarancón, D. Parfitt and J. A. Kilner, *Energy Environ. Sci.*, 2011, **4**, 2774–2789.
[175] C. Sun, H. Li and L. Chen, *Energy Environ. Sci.*, 2012, **5**, 8475–8505.
[176] M. Mogensen, D. Lybye, N. Bonanos, P. Hendriksen and F. Poulsen, *Solid State Ionics*, 2004, **174**, 279–286.
[177] L. Malavasi, C. A. Fisher and M. S. Islam, *Chem Soc Rev*, 2010, **39**, 4370–4387.
[178] N. Preux, A. Rolle and R. Vannier, *Functional materials for sustainable energy applications*, Elsevier, 2012, pp. 370–401.
[179] S. Speakman, J. Richardson, B. Mitchell and S. Misture, *Solid State Ionics*, 2002, **149**, 247–259.
[180] J. B. Goodenough, *Annual review of materials research*, 2003, **33**, 91–128.
[181] M. Khan, M. Islam and D. Bates, *The Journal of Physical Chemistry B*, 1998, **102**, 3099–3104.
[182] R. Perriot and B. P. Uberuaga, *J. Mater. Chem. A*, 2015, **3**, 11554–11565.
[183] M. Kanzaki, A. Yamaji and K. Kawakami, *MRS Online Proceedings Library (OPL)*, 1997, **496**, year.
[184] J. K. MacBride, *PhD thesis*, University of Maryland, College Park, 2016.
[185] J. P. A. De Mendonca, T. C. Lourenço, L. P. M. Freitas, A. A. Santo, G. T. Feliciano and J. L. Da Silva, *Mater. Adv.*, 2021, **2**, 7759–7772.
[186] X. Xie, J. Sun, C. Brigden, I. Farnan, Y. Hong and R. V. Kumar, *J. Mater. Chem.*, 2011, **21**, 9570–9575.
[187] T. Ishihara, H. Matsuda and Y. Takita, *J. Am. Chem. Soc.*, 1994, **116**, 3801–3803.
[188] M. Feng and J. B. Goodenough, *Eur. J. Inorg. Chem.*, 1994, **31**, 663–672.
[189] T. Ishihara, *Perovskite oxide for solid oxide fuel cells*, 2009, 65–93.
[190] M. Cherry, M. S. Islam and C. Catlow, *J. Solid State Chem.*, 1995, **118**, 125–132.

[191] M. S. Islam and P. R. Slater, *MRS bulletin*, 2009, **34**, 935–941.
[192] K. Huang, R. S. Tichy and J. B. Goodenough, *J. Am. Ceram. Soc.*, 1998, **81**, 2576–2580.
[193] T. Ishihara, J. A. Kilner, M. Honda, N. Sakai, H. Yokokawa and Y. Takita, *Solid State Ionics*, 1998, **113**, 593–600.
[194] C. Tealdi and P. Mustarelli, *J. Phys. Chem. C*, 2014, **118**, 29574–29582.
[195] M. Lerch, H. Boysen and T. Hansen, *J. Phys. Chem. Solids*, 2001, **62**, 445–455.
[196] K. Zhang, J. Sunarso, Z. Shao, W. Zhou, C. Sun, S. Wang and S. Liu, *RSC advances*, 2011, **1**, 1661–1676.
[197] T. Ishihara, H. Matsuda and Y. Takita, *Solid State Ionics*, 1995, **79**, 147–151.
[198] M. S. Islam, *J. Mater. Chem.*, 2000, **10**, 1027–1038.
[199] M.-Y. Yoon, K.-J. Hwang, D.-S. Byeon, H.-J. Hwang and S.-M. Jeong, *J. Power Sources*, 2014, **248**, 1085–1089.
[200] D.-S. Byeon, S.-M. Jeong, K.-J. Hwang, M.-Y. Yoon, H.-J. Hwang, S. Kim and H.-L. Lee, *J. Power Sources*, 2013, **222**, 282–287.
[201] D. Xu, A. Yan, Y. Yang, S. Xu, Y. Zhou, S. Yang and W.-F. Lin, *J. Power Sources*, 2023, **561**, 232723.
[202] T.-Y. Chen and K.-Z. Fung, *Journal of Alloys and Compounds*, 2004, **368**, 106–115.
[203] J. Yang, Q. Zhang, L. Dong, H. Li and C. Tian, *Functional Mater. Lett.*, 2022, **15**, 2251056.
[204] T. Onishi, *International Journal of Quantum Chemistry*, 2010, **110**, 2912–2917.
[205] H. U. Anderson, *Solid State Ionics*, 1992, **52**, 33–41.
[206] L. G. Tejuca, J. L. G. Fierro and J. M. Tascón, *Adv. Catal.*, Elsevier, 1989, vol. 36, pp. 237–328.
[207] N. Yamazoe and Y. Teraoka, *Catalysis Today*, 1990, **8**, 175–199.
[208] H. Shi, C. Su, R. Ran, J. Cao and Z. Shao, *Prog. Nat. Sci.*, 2020, **30**, 764–774.
[209] C. Alcock, J. Carberry, R. Doshi and N. Gunasekaran, *J. Catal.*, 1993, **143**, 533–538.
[210] D. Lybye, F. W. Poulsen and M. Mogensen, *Solid State Ionics*, 2000, **128**, 91–103.
[211] A. Nikonov, K. Kuterbekov, K. Z. Bekmyrza and N. Pavzderin, *Eurasian J. Phys. Funct. Mater.*, 2018, **2**, 274–292.
[212] V. Kharton, F. Marques and A. Atkinson, *Solid State Ionics*, 2004, **174**, 135–149.
[213] J. Ferguson, Y. Kim, L. F. Kourkoutis, A. Vodnick, A. Woll, D. Muller and J. Brock, *Adv Mater.*, 2011, **23**, 1226–1230.
[214] G. Kaur, Y. Cheng and M. Kaur, *Intermediate Temperature Solid Oxide Fuel Cells*, Elsevier, 2020, pp. 57–79.
[215] A. Mancini, J. F. Shin, A. Orera, P. R. Slater, C. Tealdi, Y. Ren, K. L. Page and L. Malavasi, *Dalton Trans.*, 2012, **41**, 50–53.
[216] P. Berastegui, S. Hull, F. Garcıa-Garcıa and S.-G. Eriksson, *J. Solid State Chem.*, 2002, **164**, 119–130.
[217] T. Schober, J. Friedrich and F. Krug, *Solid State Ionics*, 1997, **99**, 9–13.
[218] W. Paulus, H. Schober, S. Eibl, M. Johnson, T. Berthier, O. Hernandez, M. Ceretti, M. Plazanet, K. Conder and C. Lamberti, *J. Am. Chem. Soc.*, 2008, **130**, 16080–

16085.
[219] M. Kanzaki and A. Yamaji, *Mater. Sci. Eng.: B*, 1996, **41**, 46–49.
[220] Y.-L. Lee and D. Morgan, *MRS Online Proceedings Library (OPL)*, 2006, **972**, 0972–AA04.
[221] C. E. Mohn, N. L. Allan, C. L. Freeman, P. Ravindran and S. Stølen, *J. Solid State Chem.*, 2005, **178**, 346–355.
[222] J. B. Goodenough, J. Ruiz-Diaz and Y. Zhen, *Solid State Ionics*, 1990, **44**, 21–31.
[223] T. Yao, Y. Uchimoto, M. Kinuhata, T. Inagaki and H. Yoshida, *Solid State Ionics*, 2000, **132**, 189–198.
[224] C. Fisher, Br. Ceram. Proc., 1995, pp. 25–33.
[225] M. Pirzada, R. W. Grimes, L. Minervini, J. F. Maguire and K. E. Sickafus, *Solid State Ionics*, 2001, **140**, 201–208.
[226] L. Minervini, R. W. Grimes and K. E. Sickafus, *J. Am. Ceram. Soc.*, 2000, **83**, 1873–1878.
[227] J. Lian, L. Wang, J. Chen, K. Sun, R. Ewing, J. M. Farmer and L. Boatner, *Acta Materialia*, 2003, **51**, 1493–1502.
[228] M. Subramanian, G. Aravamudan and G. S. Rao, *Progress in Solid State Chemistry*, 1983, **15**, 55–143.
[229] P. Moon and H. Tuller, *Solid State Ionics*, 1988, **28**, 470–474.
[230] H. L. Tuller, *J. Phys. Chem. Solids*, 1994, **55**, 1393–1404.
[231] H. Yamamura, H. Nishino, K. Kakinuma and K. Nomura, *Solid State Ionics*, 2003, **158**, 359–365.
[232] P. Wilde and C. Catlow, *Solid State Ionics*, 1998, **112**, 173–183.
[233] P. Wilde and C. Catlow, *Solid State Ionics*, 1998, **112**, 185–195.
[234] M. Díaz-Guillén, K. Moreno, J. Díaz-Guillén, A. Fuentes, K. Ngai, J. Garcia-Barriocanal, J. Santamaria and C. Leon, *Phys. Rev. B*, 2008, **78**, 104304.
[235] B. J. Wuensch, K. W. Eberman, C. Heremans, E. M. Ku, P. Onnerud, E. M. Yeo, S. M. Haile, J. K. Stalick and J. D. Jorgensen, *Solid State Ionics*, 2000, **129**, 111–133.
[236] R. Perriot, P. P. Dholabhai and B. P. Uberuaga, *Phys. Chem. Chem. Phys.*, 2016, **18**, 22852–22863.
[237] P. P. Dholabhai, R. Perriot and B. P. Uberuaga, *J. Phys. Chem. C*, 2016, **120**, 10485–10499.
[238] P. Lacorre, *Solid State Sci.*, 2000, **2**, 755–758.
[239] P. Lacorre, F. Goutenoire, O. Bohnke, R. Retoux and Y. Laligant, *Nature*, 2000, **404**, 856–858.
[240] R. Subasri, H. Näfe and F. Aldinger, *Materials research bulletin*, 2003, **38**, 1965–1977.
[241] J. R. Peet, C. A. Fuller, B. Frick, M. Zbiri, A. Piovano, M. R. Johnson and I. R. Evans, *Chem. Mater.*, 2017, **29**, 3020–3028.
[242] C. Hou, Y. Li, P. Wang, C. Liu, X. Wang, Q. Fang and D. Sun, *Phys. Rev. B*, 2007, **76**, 014104.

[243] A. Nowick, G. Murch and A. Nowick, *Atom transport in oxides of the fluorite structure*, Academic Press New York, NY, USA, 1984.
[244] V. V. Kharton, A. A. Yaremchenko, E. N. Naumovich and F. M. Marques, *J. Solid State Chem.*, 2000, **4**, 243–266.
[245] D.-J. Kim, *J. Am. Ceram. Soc.*, 1989, **72**, 1415–1421.
[246] P. Sharma, K. Singh, C. Sharma and A. Singh, *International Journal of Innovative Research and Advanced Studies*, 2016, **3**, 51.
[247] B. Bai, W. A. McPhee, A. L. Smirnova and N. M. Sammes, *ECS Trans.*, 2007, **7**, 2213.
[248] W. Zhao, S. An and L. Ma, *J. Am. Ceram. Soc.*, 2011, **94**, 1496–1502.
[249] T. K. Maiti, J. Majhi, S. K. Maiti, J. Singh, P. Dixit, T. Rohilla, S. Ghosh, S. Bhushan and S. Chattopadhyay, *Environ. Sci. Pollut. Res.*, 2022, **29**, 64489–64512.
[250] A. O. Zhigachev, V. V. Rodaev, D. V. Zhigacheva, N. V. Lyskov and M. A. Shchukina, *Ceram. Int.*, 2021, **47**, 32490–32504.
[251] A. Azad, S. Larose and S. Akbar, *J. Mater. Sci.*, 1994, **29**, 4135–4151.
[252] V. V. Kharton, E. N. Naumovich, A. A. Yaremchenko and F. M. Marques, *J. Solid State Chem.*, 2001, **5**, 160–187.
[253] T. Etsell and S. N. Flengas, *Chemical Reviews*, 1970, **70**, 339–376.
[254] S. Badwal and F. Ciacchi, *Ionics*, 2000, **6**, 1–21.
[255] J. Nowotny, T. Bak, M. Nowotny and C. Sorrell, *Advances in applied ceramics*, 2005, **104**, 147–153.
[256] B. Butz, *Yttria-doped zirconia as solid electrolyte for fuel-cell applications*, 2009.
[257] T. Liu, X. Zhang, X. Wang, J. Yu and L. Li, *Ionics*, 2016, **22**, 2249–2262.
[258] S. R. Hui, J. Roller, S. Yick, X. Zhang, C. Decès-Petit, Y. Xie, R. Maric and D. Ghosh, *J. Power Sources*, 2007, **172**, 493–502.
[259] P. Vinchhi, M. Khandla, K. Chaudhary and R. Pati, *Inorganic Chemistry Communications*, 2023, 110724.
[260] N. Q. Minh, *ECS Proceedings Volumes*, 1999, **1999**, 127.
[261] N. Sammes and Z. Cai, *Solid State Ionics*, 1997, **100**, 39–44.
[262] N. Mahato, A. Gupta and K. Balani, *Nanomaterials and Energy*, 2012, **1**, 27–45.
[263] J. Kilner and R. Brook, *Solid State Ionics*, 1982, **6**, 237–252.
[264] Y. Arachi, H. Sakai, O. Yamamoto, Y. Takeda and N. Imanishai, *Solid State Ionics*, 1999, **121**, 133–139.
[265] O. Yamamoto, Y. Arachi, H. Sakai, Y. Takeda, N. Imanishi, Y. Mizutani, M. Kawai and Y. Nakamura, *Ionics*, 1998, **4**, 403–408.
[266] S. Badwal, *Solid State Ionics*, 1992, **52**, 23–32.
[267] K. Anandan, K. Rajesh, K. Gayathri, S. V. Sharma, S. M. Hussain and V. Rajendran, *Physica E: Low-dimensional Systems and Nanostructures*, 2020, **124**, 114342.
[268] S. A. Artemov, M. A. Borik, A. V. Kulebyakin, I. E. Kuritsyna, N. A. Larina, E. E. Lomonova, V. A. Myzina, P. A. Ryabochkina, N. Y. Tabachkova and T. V. Volkova,

Journal of Alloys and Compounds, 2021, **870**, 159396.

[269] M. Kilo, M. A. Taylor, C. Argirusis, G. Borchardt, S. Weber, H. Scherrer and R. A. Jackson, *J. Chem. Phys.*, 2004, **121**, 5482–5487.

[270] M. Razmkhah, M. T. Hamed Mosavian and F. Moosavi, *Int. J. Energy Res.*, 2016, **40**, 1712–1723.

[271] C. Catlow, A. Chadwick, G. Greaves and L. Moroney, *J. Am. Ceram. Soc.*, 1986, **69**, 272–277.

[272] T. Welberry, B. Butler, J. Thompson and R. Withers, *J. Solid State Chem.*, 1993, **106**, 461–475.

[273] M. áSakib Khan, M. áSaiful Islam and D. Bates, *J. Mater. Chem.*, 1998, **8**, 2299–2307.

[274] F. Shimojo and H. Okazaki, *Journal of the Physical Society of Japan*, 1992, **61**, 4106–4118.

[275] F. Shimojo, T. Okabe, F. Tachibana, M. Kobayashi and H. Okazaki, *Journal of the Physical Society of Japan*, 1992, **61**, 2848–2857.

[276] M. Meyer, N. Nicoloso and V. Jaenisch, *Phys. Rev. B*, 1997, **56**, 5961.

[277] R. Krishnamurthy, Y.-G. Yoon, D. Srolovitz and R. Car, *J. Am. Ceram. Soc.*, 2004, **87**, 1821–1830.

[278] A. Tarancón, A. Morata, F. Peiró and G. Dezanneau, *Fuel Cells*, 2011, **11**, 26–37.

[279] M. Jaipal and A. Chatterjee, *J. Phys. Chem. C*, 2017, **121**, 14534–14543.

[280] R. Kumar, V. Chauhan, D. Gupta, S. Upadhyay, J. Ram, S. Kumar *et al.*, *Indian Journal of Pure & Applied Physics (IJPAP)*, 2021, **59**, 811–826.

[281] J. Wang, X. Xiao, Y. Lu, Y. Wang, C. Chen and H. Pang, *ChemElectroChem*, 2019, **6**, 1949–1968.

[282] J. W. Fergus, *J. Power Sources*, 2006, **162**, 30–40.

[283] M. Sase, D. Ueno, K. Yashiro, A. Kaimai, T. Kawada and J. Mizusaki, *J. Phys. Chem. Solids*, 2005, **66**, 343–348.

[284] S. Omar, W. B. Najib and N. Bonanos, *Solid State Ionics*, 2011, **189**, 100–106.

[285] Z. Zakaria and S. K. Kamarudin, *Int. J. Energy Res.*, 2021, **45**, 4871–4887.

[286] Y.-H. Choi, S.-H. Lee, J. Wackerl, D.-H. Jung, D.-S. Suhr, S.-Y. Choi and D.-H. Peck, *Ceram. Int.*, 2012, **38**, S485–S488.

[287] N. A. Arifin, A. A. Afifi, A. Samreen, R. Hafriz and A. Muchtar, *Solid State Ionics*, 2023, **399**, 116302.

[288] Q. Xue, X. Huang, L. Wang, H. Zhang and J. Zhang, *Phys. Rev. Applied*, 2018, **10**, 014032.

[289] J. Savioli and G. W. Watson, *Current Opinion in Electrochemistry*, 2020, **21**, 14–21.

[290] K. Amarsingh Bhabu, J. Theerthagiri, J. Madhavan, T. Balu, G. Muralidharan and T. Rajasekaran, *J. Mater. Sci.: Materials in Electronics*, 2016, **27**, 1566–1573.

[291] M. Dudek, *J. Eur. Ceram.*, 2008, **28**, 965–971.

[292] P. Arunkumar, M. Meena and K. S. Babu, *Nanomaterials and Energy*, 2012, **1**, 288–305.

[293] P. Temluxame, P. Puengjinda, S. Peng-ont, W. Ngampuengpis, N. Sirimungkalakul, T. Jiwanuruk, T. Sornchamni and P. Kim-Lohsoontorn, *Int. J. Hydrog. Energy*, 2021, **46**, 24568–24580.
[294] J. Zhang, C. Lenser, N. H. Menzler and O. Guillon, *Solid State Ionics*, 2020, **344**, 115138.
[295] J. F. Q. Rey and E. Muccillo, *J. Eur. Ceram.*, 2004, **24**, 1287–1290.
[296] C. Cheng, S. Lee and C. Hong, *J. Electrochem. Soc.*, 2007, **154**, E158.
[297] T. Horita, T. Kawada, N. Sakai, H. Yokokawa, M. Dokiya *et al.*, *Solid State Ionics*, 1996, **86**, 1255–1258.
[298] T. Horita, T. Kawada, N. Sakai, H. Yokokawa, M. Dokiya *et al.*, *J. Eur. Ceram.*, 1996, **16**, 961–973.
[299] Z. Fan and F. B. Prinz, *Nano letters*, 2011, **11**, 2202–2205.
[300] A. Sawka and A. Kwatera, *Mater. Sci. Eng.: B*, 2022, **276**, 115580.
[301] K. Eguchi, T. Setoguchi, T. Inoue and H. Arai, *Solid State Ionics*, 1992, **52**, 165–172.
[302] T. Takahashi, *p. 989 in 'Physics of Electrolytes' Vol 2., Edit. J. Hladik*, 1972.
[303] V. Butler, C. Catlow, B. Fender and J. Harding, *Solid State Ionics*, 1983, **8**, 109–113.
[304] J.-Y. Park, H. Yoon and E. D. Wachsman, *J. Am. Ceram. Soc.*, 2005, **88**, 2402–2408.
[305] S. Sameshima, Y. Hirata and Y. Ehira, *Journal of alloys and compounds*, 2006, **408**, 628–631.
[306] Y.-P. Fu, S.-H. Chen and J.-J. Huang, *Int. J. Hydrog. Energy*, 2010, **35**, 745–752.
[307] J. Faber, C. Geoffroy, A. Roux, A. Sylvestre and P. Abelard, *Applied Physics A*, 1989, **49**, 225–232.
[308] J. Koettgen and M. Martin, *J. Am. Ceram. Soc.*, 2020, **103**, 3776–3787.
[309] J. Koettgen and M. Martin, *J. Phys. Chem. C*, 2019, **123**, 6333–6339.
[310] M. Burbano, S. T. Norberg, S. Hull, S. G. Eriksson, D. Marrocchelli, P. A. Madden and G. W. Watson, *Chem. Mater.*, 2012, **24**, 222–229.
[311] S. Omar, E. D. Wachsman, J. L. Jones and J. C. Nino, *J. Am. Ceram. Soc.*, 2009, **92**, 2674–2681.
[312] L. Minervini, M. O. Zacate and R. W. Grimes, *Solid State Ionics*, 1999, **116**, 339–349.
[313] H. Inaba, R. Sagawa, H. Hayashi and K. Kawamura, *Solid State Ionics*, 1999, **122**, 95–103.
[314] P. P. Dholabhai and J. B. Adams, *J. Mater. Sci.*, 2012, **47**, 7530–7541.
[315] S. B. Adler and J. W. Smith, *Journal of the Chemical Society, Faraday Transactions*, 1993, **89**, 3123–3128.
[316] H. Hayashi, R. Sagawa, H. Inaba and K. Kawamura, *Solid State Ionics*, 2000, **131**, 281–290.
[317] S. Huang, L. Li, O. Van der Biest and J. Vleugels, *Solid State Sci.*, 2005, **7**, 539–544.
[318] G. VanHandel and R. Blumenthal, *J. Electrochem. Soc.*, 1974, **121**, 1198.
[319] Y.-P. Xiong, H. Kishimoto, K. Yamaji, M. Yoshinaga, T. Horita, M. E. Brito and H. Yokokawa, *J Solid State Electrochem .*, 2010, **13**, B21.
[320] A. Tsoga, A. Naoumidis and D. Stöver, *Solid state ionics*, 2000, **135**, 403–409.

[321] T. Tsai, E. Perry and S. Barnett, *J. Electrochem. Soc.*, 1997, **144**, L130.
[322] R. V. PASCU, *REV. CHIM (Bucharest)*, 2019, **70**, 4181.
[323] Z. Gao, V. Y. Zenou, D. Kennouche, L. Marks and S. A. Barnett, *J. Mater. Chem. A*, 2015, **3**, 9955–9964.
[324] J. Van Herle, D. Seneviratne and A. McEvoy, *J. Eur. Ceram.*, 1999, **19**, 837–841.
[325] P. P. Dholabhai, J. B. Adams, P. A. Crozier and R. Sharma, *J. Mater. Chem.*, 2011, **21**, 18991–18997.
[326] Y. Zheng, Y. Shi, H. Gu, L. Gao, H. Chen and L. Guo, *Materials Research Bulletin*, 2009, **44**, 1717–1721.
[327] J. T. Irvine, J. W. Dobson, T. Politova, S. G. Martín and A. Shenouda, *Faraday discussions*, 2007, **134**, 41–49.
[328] K.-L. Tung, K.-S. Chang, C.-C. Hsiung, Y.-C. Chiang and Y.-L. Li, *Separation and Purification Technology*, 2010, **73**, 13–19.
[329] M. E. Kilic and A. Soon, *J. Phys. Chem. C*, 2018, **122**, 22374–22388.
[330] Z. Lu, J. Zhu, Z. Bi and X. Lu, *J. Power Sources*, 2008, **180**, 172–175.
[331] M. Chen, B. H. Kim, Q. Xu, O. J. Nam and J. H. Ko, *J. Eur. Ceram.*, 2008, **28**, 2947–2953.
[332] B. Zhu, X. Liu, P. Zhou, Z. Zhu, W. Zhu and S. Zhou, *J. Mater. Sci. letters*, 2001, **20**, 591–594.
[333] E. P. Murray, T. Tsai and S. A. Barnett, *Nature*, 1999, **400**, 649–651.
[334] S. Park, J. M. Vohs and R. J. Gorte, *Nature*, 2000, **404**, 265–267.
[335] X.-F. Ye, S. Wang, Q. Hu, J. Chen, T. Wen and Z. Wen, *Solid State Ionics*, 2009, **180**, 276–281.
[336] B. Huang, X. Ye, S. Wang, H. Nie, R. Liu and T. Wen, *Materials research bulletin*, 2007, **42**, 1705–1714.
[337] Y. Nabae and I. Yamanaka, *Applied Catalysis A: General*, 2009, **369**, 119–124.
[338] D. Ding, L. Li, K. Feng, Z. Liu and C. Xia, *J. Power Sources*, 2009, **187**, 400–402.
[339] A. Sin, E. Kopnin, Y. Dubitsky, A. Zaopo, A. Aricò, D. La Rosa, L. Gullo and V. Antonucci, *J. Power Sources*, 2007, **164**, 300–305.
[340] N. Metropolis, A. W. Rosenbluth, M. N. Rosenbluth, A. H. Teller and E. Teller, *J. Chem. Phys.*, 1953, **21**, 1087–1092.
[341] A. G. Kalinichev, P. Padma Kumar and R. James Kirkpatrick, *Philosophical Magazine*, 2010, **90**, 2475–2488.
[342] X. Liu, C. Tournassat, S. Grangeon, A. G. Kalinichev, Y. Takahashi and M. Marques Fernandes, *Nature Reviews Earth & Environment*, 2022, **3**, 461–476.
[343] R. T. Cygan, J.-J. Liang and A. G. Kalinichev, *The Journal of Physical Chemistry B*, 2004, **108**, 1255–1266.
[344] A. G. Kalinichev and R. J. Kirkpatrick, *Chem. Mater.*, 2002, **14**, 3539–3549.
[345] C. M. MacDermaid, H. K. Kashyap, R. H. DeVane, W. Shinoda, J. B. Klauda, M. L. Klein and G. Fiorin, *J. Chem. Phys.*, 2015, **143**, year.
[346] S. Kaur, S. Sharma and H. K. Kashyap, *J. Chem. Phys.*, 2017, **147**, year.

[347] M. Kumari, P. Kumari and H. K. Kashyap, *Phys. Chem. Chem. Phys.*, 2022, **24**, 5627–5637.
[348] H. W. Lee, G.-U. Jeong, M.-C. Kim, D. Kim, S. Kim and S. S. Han, *Int. J. Hydrog. Energy*, 2023, **48**, 3931–3941.
[349] S. Prasad, C. Chakravarty and H. K. Kashyap, *Journal of Molecular Liquids*, 2017, **225**, 240–250.
[350] A. Sayeed, S. Mitra, A. Anil Kumar, R. Mukhopadhyay, S. Yashonath and S. Chaplot, *The Journal of Physical Chemistry B*, 2003, **107**, 527–533.
[351] A. Anil Kumar, S. Yashonath and G. Ananthakrishna, *The Journal of Physical Chemistry B*, 2006, **110**, 3835–3840.
[352] R. Chitra, A. Anil Kumar and S. Yashonath, *J. Chem. Phys.*, 2001, **114**, 11–14.
[353] A. Anil Kumar, *J. Chem. Phys.*, 2014, **141**, year.
[354] H.-K. Tian, Z. Liu, Y. Ji, L.-Q. Chen and Y. Qi, *Chem. Mater.*, 2019, **31**, 7351–7359.
[355] S. Punnathanam and P. Monson, *J. Chem. Phys.*, 2006, **125**, year.
[356] I. Daems, G. V. Baron, S. Punnathanam, R. Q. Snurr and J. F. Denayer, *J. Phys. Chem. C*, 2007, **111**, 2191–2197.
[357] H. Pimpalgaonkar, S. K. Veesam and S. N. Punnathanam, *J. Phys. Chem. B*, 2011, **115**, 10018–10026.
[358] S. Ravipati and S. N. Punnathanam, *Ind. Eng. Chem. Res. I*, 2012, **51**, 9419–9426.
[359] C.-H. Chan, S. Y. Lee and S. S. Han, *Int. J. Hydrog. Energy*, 2023.
[360] M. Kim, B. C. Yeo, Y. Park, H. M. Lee, S. S. Han and D. Kim, *Chem. Mater.*, 2019, **32**, 709–720.
[361] H. Choi, D. Shin, B. C. Yeo, T. Song, S. S. Han, N. Park and S. Kim, *ACS Catal.*, 2016, **6**, 2745–2753.
[362] R. P. Hardikar, D. Das, S. S. Han, K.-R. Lee and A. K. Singh, *Phys. Chem. Chem. Phys.*, 2014, **16**, 16502–16508.
[363] J. Park, H. Kim, S. S. Han and Y. Jung, *J. Phys. Chem. Lett.*, 2012, **3**, 826–829.
[364] M. P. Allen and D. J. Tildesley, *Computer simulation of liquids*, Oxford university press, 2017.
[365] D. Frenkel and B. Smit, *B. Smit*, Elsevier, 2001, vol. 1.
[366] B. J. Alder and T. E. Wainwright, *J. Chem. Phys.*, 1959, **31**, 459–466.
[367] A. Rahman, *Phys. Rev.*, 1964, **136**, A405.
[368] A. Rahman and F. H. Stillinger, *J. Chem. Phys.*, 1971, **55**, 3336–3359.
[369] K. Supreet, G. Aditya *et al.*, 2016.
[370] S. Kaur, M. Kumari and H. K. Kashyap, *The Journal of Physical Chemistry B*, 2020, **124**, 10601–10616.
[371] A. Gupta, S. Kaur and H. K. Kashyap, *The Journal of Physical Chemistry B*, 2019, **123**, 2057–2069.
[372] R. Car and M. Parrinello, *Phys. Rev. letters*, 1985, **55**, 2471.
[373] W. Kohn and L. J. Sham, *Phys. Rev.*, 1965, **140**, A1133.
[374] A. A. Kumar, S. Yashonath, M. Sluiter and Y. Kawazoe, *Phys. Rev. E*, 2001, **65**, 011203.

[375] B. Gao, R. Jalem, H.-K. Tian and Y. Tateyama, *Adv. Energy Mater.*, 2022, **12**, 2102151.
[376] H.-K. Tian, B. Xu and Y. Qi, *J. Power Sources*, 2018, **392**, 79–86.
[377] S. Punnathanam and D. S. Corti, *J. Chem. Phys.*, 2003, **119**, 10224–10236.
[378] L. Verlet, *Phys. Rev.*, 1967, **159**, 98.
[379] C. Kittel and D. F. Holcomb, *American Journal of Physics*, 1967, **35**, 547–548.
[380] P. Vashishta and A. Rahman, *Phys. Rev. Letters*, 1978, **40**, 1337.
[381] R. Etters and J. Kaelberer, *Phys. Rev. A*, 1975, **11**, 1068.
[382] H. L. Davis, J. Jellinek and R. S. Berry, *J. Chem. Phys.*, 1987, **86**, 6456–6464.
[383] D. Adams, *Mol. Phys.*, 1975, **29**, 307–311.
[384] M. Wolf, J. Walker and C. Catlow, *Solid State Ionics*, 1984, **13**, 33–38.
[385] M. Gillan and M. Dixon, *Journal of Physics C: Solid State Physics*, 1980, **13**, 1901.
[386] Z. Cheng, J. Chang, Z. Jia and N. Chen, *Molecular simulation*, 1993, **10**, 27–39.
[387] R. A. Montani, *J. Chem. Phys.*, 1994, **100**, 8381–8384.
[388] B. Ammundsen and J. Paulsen, *Adv Mater.*, 2001, **13**, 943–956.
[389] J. R. Ray and P. Vashishta, *J. Chem. Phys.*, 1989, **90**, 6580–6586.
[390] P. Sindzingre and M. Gillan, *Journal of Physics C: Solid State Physics*, 1988, **21**, 4017.
[391] J. G. Lee, *Computational materials science: an introduction*, CRC press, 2016.
[392] S. Nosé, *J. Chem. Phys.*, 1984, **81**, 511–519.
[393] S. Ikeda, O. Sakurai, K. Uematsu, N. Mizutani and M. Kato, *J. Mater. Sci.*, 1985, **20**, 4593–4600.
[394] T. Suemoto and M. Ishigame, *Solid State Ionics*, 1986, **21**, 225–229.
[395] J. Luo, D. P. Almond and R. Stevens, *J. Am. Ceram. Soc.*, 2000, **83**, 1703–1708.
[396] W. Jung, J. L. Hertz and H. L. Tuller, *Acta Mater.*, 2009, **57**, 1399–1404.
[397] R. Grosso, R. Muccillo and E. Muccillo, *Mater. Lett.*, 2014, **134**, 27–29.
[398] M. Asadikiya and Y. Zhong, *J. Mater. Sci.*, 2018, **53**, 1699–1709.
[399] H.-J. Beie and A. Gn rich, *Sens. Actuators B Chem.*, 1991, **4**, 393–399.
[400] B. C. Steele and A. Heinzel, *A. Heinzel*, World Scientific, 2011, pp. 224–231.
[401] J. Koettgen, S. Grieshammer, P. Hein, B. O. Grope, M. Nakayama and M. Martin, *Phys. Chem. Chem. Phys.*, 2018, **20**, 14291–14321.
[402] B. C. Steele, *Solid State Ionics*, 2000, **129**, 95–110.
[403] M. Mogensen, N. M. Sammes and G. A. Tompsett, *Solid State Ionics*, 2000, **129**, 63–94.
[404] T. Inoue, T. Setoguchi, K. Eguchi and H. Arai, *Solid State Ionics*, 1989, **35**, 285–291.
[405] K. Tanwar, N. Jaiswal, D. Kumar and O. Parkash, *J. Alloys Compd.*, 2016, **684**, 683–690.
[406] J. Huang, Z. Mao, L. Yang and R. Peng, *Electrochem. solid-state lett.*, 2005, **8**, A437.
[407] X. Wang, Y. Ma, R. Raza, M. Muhammed and B. Zhu, *Electrochem. commun.*, 2008, **10**, 1617–1620.
[408] H. Hayashi, M. Kanoh, C. J. Quan, H. Inaba, S. Wang, M. Dokiya and H. Tagawa, *Solid State Ionics*, 2000, **132**, 227–233.

[409] Y.-D. Kim, J. Yang, J.-I. Lee, M. Saqib, J.-S. Shin, K. Park, M. Jo, S.-J. Song and J.-Y. Park, *J. Power Sources*, 2020, **452**, 227758.
[410] C. Chen, M. Nasrallah and H. Anderson, *ECS Proceedings Volumes*, 1993, **1993**, 598.
[411] R. J. Konings, O. Beneš, A. Kovács, D. Manara, D. Sedmidubskỳ, L. Gorokhov, V. S. Iorish, V. Yungman, E. Shenyavskaya and E. Osina, *J. Phys. Chem. Ref. Data*, 2014, **43**, 013101.
[412] H. Tuller and A. Nowick, *J. Electrochem. Soc.*, 1975, **122**, 255.
[413] H. Tuller and A. Nowick, *J. Electrochem. Soc.*, 1979, **126**, 209.
[414] D. Park, J. Griffith, A. Nowick *et al.*, *Solid State Ionics*, 1981, **2**, 95–105.
[415] M. A. Panhans and R. Blumenthal, *Solid State Ionics*, 1993, **60**, 279–298.
[416] J. O. Nilsson, M. Leetmaa, O. Y. Vekilova, S. I. Simak and N. V. Skorodumova, *Phys. Chem. Chem. Phys.*, 2017, **19**, 13723–13730.
[417] N. Jaiswal, K. Tanwar, R. Suman, D. Kumar, S. Upadhyay and O. Parkash, *J. Alloys Compd.*, 2019, **781**, 984–1005.
[418] J.-H. Lee, S. Yoon, B.-K. Kim, J. Kim, H.-W. Lee and H.-S. Song, *Solid State Ionics*, 2001, **144**, 175–184.
[419] S. Zha, C. Xia and G. Meng, *J. Power Sources*, 2003, **115**, 44–48.
[420] Q. Fu, S. Zha, W. Zhang, D. Peng, G. Meng and B. Zhu, *J. Power Sources*, 2002, **104**, 73–78.
[421] V. Longo and L. Podda, *J. Mater. Sci.*, 1981, **16**, 839–841.
[422] M. Murutoglu, T. Ucun, O. Ulasan, A. Buyukaksoy, Y. K. Tur and H. Yilmaz, *Int. J. Hydrog. Energy*, 2022, **47**, 19772–19779.
[423] I. W. Choi, W. Yu, M. S. Lee, S. Ryu, Y. H. Lee, S. W. Cha and G. Y. Cho, *J. Power Sources*, 2022, **531**, 231320.
[424] T. H. Dang, V. H. Vu, N. T. Pham, N. D. Lo, T. H. Le Thi, T. M. A. Hoang and L. Le Thu, *VNU Journal of Science: Mathematics-Physics*, 2022, **38**, year.
[425] M. Gupta, S. C. Shirbhate, O. V. Rambadey, S. A. Acharya and P. R. Sagdeo, *ACS Appl. Energy Mater.*, 2022, **5**, 9759–9769.
[426] A. Solovyev, A. Shipilova, E. Smolyanskiy, S. Rabotkin and V. Semenov, *Membranes*, 2022, **12**, 896.
[427] S. Anirban and A. Dutta, *ACS Appl. Energy Mater.*, 2021, **303**, 122451.
[428] A. Murray, G. Murch and C. Catlow, *Solid State Ionics*, 1986, **18**, 196–202.
[429] H. Inaba and H. Tagawa, *Solid State Ionics*, 1996, **83**, 1–16.
[430] G. F. Harrington, S. Kim, K. Sasaki, H. L. Tuller and S. Grieshammer, *J. Mater. Chem A*, 2021, **9**, 8630–8643.
[431] X. Sha, Z. Lü, X. Huang, J. Miao, Z. Ding, X. Xin and W. Su, *J. Alloys Compd.*, 2007, **428**, 59–64.
[432] D. Pérez-Coll and G. C. Mather, *Solid State Ionics*, 2010, **181**, 20–26.
[433] H. Yahiro, Y. Baba, K. Eguchi and H. Arai, *J. Electrochem. Soc.*, 1988, **135**, 2077.
[434] E. Subbarao and H. Maiti, *Solid State Ionics*, 1984, **11**, 317–338.

[435] H.-C. Lee, D. Kim, J.-A. Lee, Y.-W. Heo, J.-J. Kim and J.-H. Lee, *s J. Sci.: Adv. Mater. Devices*, 2022, **7**, 100450.
[436] M. E. Kilic, J.-H. Lee and K.-R. Lee, *J. Mater. Chem A.*, 2021, **9**, 13883–13889.
[437] S. Anirban, P. T. Das and A. Dutta, *Ceram. Int.*, 2019, **45**, 5751–5760.
[438] H. Wang, Y. Ma, W. Yang, D. Wang, C. Wang, D. Yan and R. Liu, *Ceram. Int.*, 2022.
[439] J. A. Kilner, *Solid State Ionics*, 2000, **129**, 13–23.
[440] J. Conesa, *Surf. Sci.*, 1995, **339**, 337–352.
[441] L. Gerward, J. S. Olsen, L. Petit, G. Vaitheeswaran, V. Kanchana and A. Svane, *J. Alloys Compd.*, 2005, **400**, 56–61.
[442] A. Ismail, J. Hooper, J. B. Giorgi and T. K. Woo, *Phys. Chem. Chem. Phys.*, 2011, **13**, 6116–6124.
[443] D. E. Vanpoucke, P. Bultinck, S. Cottenier, V. Van Speybroeck and I. Van Driessche, *J. Mater. Chem A*, 2014, **2**, 13723–13737.
[444] C. B. Gopal and A. van de Walle, *Phys. Rev. B*, 2012, **86**, 134117.
[445] M. Alaydrus, M. Sakaue and H. Kasai, *Phys. Chem. Chem. Phys.*, 2016, **18**, 12938–12946.
[446] S. Grieshammer, B. O. Grope, J. Koettgen and M. Martin, *Phys. Chem. Chem. Phys.*, 2014, **16**, 9974–9986.
[447] J. Koettgen and M. Martin, *J. Phys. Chem. C.*, 2019, **123**, 19437–19446.
[448] P. Hein, B. O. Grope, J. Koettgen, S. Grieshammer and M. Martin, *Mater. Chem. Phys.*, 2021, **257**, 123767.
[449] R. Gerhardt-Anderson and A. Nowick, *Solid State Ionics*, 1981, **5**, 547–550.
[450] D. A. Andersson, S. I. Simak, N. V. Skorodumova, I. A. Abrikosov and B. Johansson, *Proceedings of the National Academy of Sciences*, 2006, **103**, 3518–3521.
[451] S. Vives, D. Ramel and C. Meunier, *Ceram. Int.*, 2019, **45**, 21625–21634.
[452] J. Koettgen, P. C. Schmidt, T. Bučko and M. Martin, *Phys. Rev. B*, 2018, **97**, 024305.
[453] D. Taylor, *Br. Ceram. Trans.*, 1984, **83**, 32–37.
[454] J. McBride, K. Hass, B. Poindexter and W. Weber, *J. Appl. Phys.*, 1994, **76**, 2435–2441.
[455] M. WoŁcyrz and L. Kepinski, *J. Solid State Chem.*, 1992, **99**, 409–413.
[456] R. Ko, M. Ricken, J. No, I. Riess *et al.*, *J. Solid State Chem.*, 1989, **78**, 136–147.
[457] R. A. Buckingham, *m, R. A. Proc. Roy. Soc. (London)*, 1938, **168**, 264–283.
[458] G. Lewis and C. Catlow, *J. Phys. C: Solid State Phys*, 1985, **18**, 1149.
[459] S. Plimpton, *J. Comput. Phys.*, 1995, **117**, 1–19.
[460] J. Kilner, *Solid State Ionics*, 1983, **8**, 201–207.
[461] B. Matović, M. Stojmenović, J. Pantić, A. Varela, M. Žunić, N. Jiraborvornpongsa and T. Yano, *J. Asian Ceram. Soc.*, 2014, **2**, 117–122.
[462] S. Dikmen, P. Shuk and M. Greenblatt, *Solid State Ionics*, 1999, **126**, 89–95.
[463] Z. Tianshu, P. Hing, H. Huang and J. Kilner, *Solid State Ionics*, 2002, **148**, 567–573.
[464] W. Miśta, M. A. Małecka and L. Kepiński, *Appl. Catal. A: Gen.*, 2009, **368**, 71–78.

[465] *J. Electrochem. Soc.*, 2001, **148**, A427.
[466] L. Aneflous, J. A. Musso, S. Villain, J.-R. Gavarri and H. Benyaich, *J. Solid State Chem.*, 2004, **177**, 856–865.
[467] V. Kharton, F. Figueiredo, L. Navarro, E. Naumovich, A. Kovalevsky, A. Yaremchenko, A. P. Viskup, A. Carneiro, F. Marques, Frade and JR, *J. Mater. Sci.*, 2001, **36**, 1105–1117.
[468] T. Ohashi, S. Yamazaki, T. Tokunaga, Y. Arita, T. Matsui, T. Harami and K. Kobayashi, *Solid State Ionics*, 1998, **113**, 559–564.
[469] C. Tian and S.-W. Chan, *Solid State Ionics*, 2000, **134**, 89–102.
[470] N. Q. Minh, *J. Am. Ceram. Soc.*, 1993, **76**, 563–588.
[471] Y. Yamamura, S. Kawasaki and H. Sakai, *Solid State Ionics*, 1999, **126**, 181–189.
[472] P. P. Dholabhai, S. Anwar, J. B. Adams, P. Crozier and R. Sharma, *J. Solid State Chem.*, 2011, **184**, 811–817.
[473] O. Tripathy and P. P. Kumar, *J. Mater. Sci.*, 2017, **52**, 6542–6553.
[474] S. H. Jacobson, M. A. Ratner and A. Nitzan, *Phys. Rev. B*, 1981, **23**, 1580.
[475] P. P. Kumar and S. Yashonath, *J. Phys. Chem. B*, 2002, **106**, 7081–7089.
[476] K. Sau and P. P. Kumar, *J. Phys. Chem. C*, 2015, **119**, 18030–18037.
[477] X. Guo, W. Sigle and J. Maier, *J. Am. Ceram. Soc.*, 2003, **86**, 77–87.
[478] T. Zhang, J. Ma, H. Huang, P. Hing, Z. Xia, S. Chan and J. Kilner, *Solid State Sci.*, 2003, **5**, 1505–1511.
[479] S. C. Singhal, *Solid State Ionics*, 2000, **135**, 305–313.
[480] P. Singh and N. Q. Minh, *Int. J. Appl. Ceram. Technol.*, 2004, **1**, 5–15.
[481] D. J. Brett, A. Atkinson, N. P. Brandon and S. J. Skinner, *Chem. Soc. Rev.*, 2008, **37**, 1568–1578.
[482] S. M. Haile, *Acta Mater.*, 2003, **51**, 5981–6000.
[483] T. Elmer, M. Worall, S. Wu and S. B. Riffat, *Renew. Sust. Energ. Rev.*, 2015, **42**, 913–931.
[484] N. Sammes, G. Tompsett, H. Näfe and F. Aldinger, *J. Eur. Ceram. Soc.*, 1999, **19**, 1801–1826.
[485] A. Pimenov, J. Ullrich, P. Lunkenheimer, A. Loidl and C. Rüscher, *Solid State Ionics*, 1998, **109**, 111–118.
[486] J. C. M. Madrid, J. Matsuda, K. Leonard, H. Matsumoto and K. K. Ghuman, *J. Mater. Chem. A*, 2022, **10**, 2567–2579.
[487] H. Brinkman, W. J. Briels and H. Verweij, *Chem. Phys. Lett.*, 1995, **247**, 386–390.
[488] M. Kilo, C. Argirusis, G. Borchardt and R. A. Jackson, *Phys. Chem. Chem. Phys.*, 2003, **5**, 2219–2224.
[489] K. C. Lau and B. I. Dunlap, *J. Condens. Matter Phys.*, 2011, **23**, 035401.
[490] P. K. Schelling and S. R. Phillpot, *J. Am. Ceram. Soc.*, 2001, **84**, 2997–3007.
[491] X. Xie, R. Kumar, J. Sun and L. Henson, *J. Power Sources*.
[492] S. P. Miller, B. I. Dunlap and A. S. Fleischer, *Solid State Ionics*, 2013, **253**, 130–136.
[493] Y.-H. Chan, H.-Y. Lai *et al.*, *Comput. Mater. Sci.*, 2018, **147**, 1–6.
[494] S. Grieshammer, I. V. Belova and G. E. Murch, *Acta Mater.*, 2021, **210**, 116802.

[495] D.-J. Kim, S.-H. Hyun, S.-G. Kim and M. Yashima, *J. Am. Ceram. Soc.*, 1994, **77**, 597–599.
[496] G. Katz, *J. Am. Ceram. Soc*, 1971, **54**, 531–531.
[497] P. Duwez, F. H. Brown Jr and F. Odell, *J. Electrochem. Soc.*, 1951, **98**, 356.
[498] M. B. Pomfret, C. Stoltz, B. Varughese and R. A. Walker, *Anal. Chem.*, 2005, **77**, 1791–1795.
[499] Y.-M. Sung and D.-H. Kim, *J. Cryst. Growth.*, 2003, **254**, 411–417.
[500] T. P. Perumal, V. Sridhar, K. Murthy, K. Easwarakumar and S. Ramasamy, *Phys. A*, 2002, **309**, 35–44.
[501] R. Pornprasertsuk, P. Ramanarayanan, C. B. Musgrave and F. B. Prinz, *Int. J. Appl. Phys.*, 2005, **98**, 103513.
[502] X. Li and B. Hafskjold, *J. Condens. Matter Phys.*, 1995, **7**, 1255.
[503] J. de Dios Solier, M. A. Pérez-Jubindo, A. Dominguez-Rodriguez and A. H. Heuer, *J. Am. Ceram. Soc.*, 1989, **72**, 1500–1502.
[504] M. Filal, C. Petot, M. Mokchah, C. Chateau and J. Carpentier, *Solid State Ionics*, 1995, **80**, 27–35.
[505] I. R. Gibson and J. T. Irvine, *J. Mater. Chem.*, 1996, **6**, 895–898.
[506] M. Gerstl, G. Friedbacher, F. Kubel, H. Hutter and J. Fleig, *Phys. Chem. Chem. Phys.*, 2013, **15**, 1097–1107.
[507] R. Ramamoorthy, D. Sundararaman and S. Ramasamy, *Solid State Ionics*, 1999, **123**, 271–278.
[508] J. Jiang, X. Hu, W. Shen, C. Ni and J. L. Hertz, *Appl. Phys. Lett.*, 2013, **102**, 143901.
[509] L. Momenzadeh, I. V. Belova and G. E. Murch, *Comput. Condens. Matter*, 2021, **28**, e00583.
[510] S.-H. Guan, C. Shang and Z.-P. Liu, *J. Phys. Chem. C*, 2020, **124**, 15085–15093.
[511] V. V. Sizov, M. J. Lampinen and A. Laaksonen, *Solid State Ionics*, 2014, **266**, 29–35.
[512] P. Manning, J. Sirman, R. De Souza and J. Kilner, *Solid State Ionics*, 1997, **100**, 1–10.
[513] J. Sirman, P. Manning and J. Kilner, *Solid State Ionics*, 1997, **93**, 125–132.
[514] R. Krishnamurthy, D. Srolovitz, K. Kudin and R. Car, *J. Am. Ceram. Soc.*, 2005, **88**, 2143–2151.
[515] J.-P. Boilot, G. Collin and P. Colomban, *J. Solid State Chem.*, 1988, **73**, 160–171.
[516] J. Boilot, G. Collin and P. Colomban, *Materials research bulletin*, 1987, **22**, 669–676.
[517] K. Pramanik, K. Sau and P. P. Kumar, *J. Phys. Chem. C*, 2020, **124**, 4001–4009.
[518] S. C. Singhal, *Solid State Ionics*, 2002, **152**, 405–410.
[519] O. Posdziech, T. Geißler, K. Schwarze and R. Blumentritt, *ECS Trans.*, 2019, **91**, 2537.
[520] C.-C. Chao, Y. B. Kim and F. B. Prinz, *Nano letters*, 2009, **9**, 3626–3628.
[521] C.-C. Chao, J. S. Park, X. Tian, J. H. Shim, T. M. Gur and F. B. Prinz, *ACS nano*, 2013, **7**, 2186–2191.
[522] J. Y. Paek, I. Chang, J. H. Park, S. Ji and S. W. Cha, *Renewable energy*, 2014, **65**,

202–206.

[523] H. Hidalgo, E. Reguzina, E. Millon, A.-L. Thomann, J. Mathias, C. Boulmer-Leborgne, T. Sauvage and P. Brault, *Surface and Coatings Technology*, 2011, **205**, 4495–4499.

[524] M. Mosiałek, M. B. Hanif, T. Šalkus, A. Kežionis, E. Kazakevičius, A. F. Orliukas, R. P. Socha, W. Łasocha, M. Dziubaniuk, J. Wyrwa *et al.*, *Ceram. Int.*, 2023, **49**, 15276–15283.

[525] J. W. Shin, S. Lee, D. Go, B. C. Yang, T. Kim, S. E. Jo, P.-C. Su and J. An, *International Journal of Precision Engineering and Manufacturing-Green Technology*, 2023, **10**, 773–781.

[526] J. H. Shim, C.-C. Chao, H. Huang and F. B. Prinz, *Chem. Mater.*, 2007, **19**, 3850–3854.

[527] J. Kim, S. Im, S. H. Oh, J. Y. Lee, K. J. Yoon, J.-W. Son, S. Yang, B.-K. Kim, J.-H. Lee, H.-W. Lee *et al.*, *Science Advances*, 2021, **7**, eabj8590.

[528] H.-S. Noh, J.-W. Son, H. Lee, H.-S. Song, H.-W. Lee and J.-H. Lee, *J. Electrochem. Soc.*, 2009, **156**, B1484.

[529] H. Huang, J. Shim, C.-C. Chao, R. Pornprasertsuk, M. Sugawara, T. Gur and F. Prinz, *J. Electrochem. Soc.*, 2009, **156**, B392.

[530] H. J. Kim, M. Kim, K. C. Neoh, G. D. Han, K. Bae, J. M. Shin, G.-T. Kim and J. H. Shim, *J. Power Sources*, 2016, **327**, 401–407.

[531] G. Y. Cho, Y. H. Lee, W. Yu, J. An and S. W. Cha, *Energy*, 2019, **173**, 436–442.

[532] S. Azad, O. A. Marina, C. M. Wang, L. Saraf, V. Shutthanandan, D. E. McCready, A. El-Azab, J. E. Jaffe, M. H. Engelhard, C. H. Peden *et al.*, *Applied Physics Letters*, 2005, **86**, 13.

[533] D. Agarkov, M. Borik, S. Bredikhin, I. Burmistrov, G. Eliseeva, V. Kolotygin, A. Kulebyakin, I. Kuritsyna, E. Lomonova, F. Milovich *et al.*, *Journal of Materiomics*, 2019, **5**, 273–279.

[534] X. Huang, D. Wang, M. Lamontagne and C. Moreau, *Mater. Sci. Eng.: B*, 2008, **149**, 63–72.

[535] J. Rao, Y. Zhou and D. Li, *Journal of Materials Research*, 2001, **16**, 1806–1813.

[536] J. Goff, W. Hayes, S. Hull, M. Hutchings and K. N. r. Clausen, *Phys. Rev. B*, 1999, **59**, 14202.

[537] G. Stapper, M. Bernasconi, N. Nicoloso and M. Parrinello, *Phys. Rev. B*, 1999, **59**, 797.

[538] A. Kushima and B. Yildiz, *J. Mater. Chem.*, 2010, **20**, 4809–4819.

[539] K. Kawata, H. Maekawa, T. Nemoto and T. Yamamura, *Solid State Ionics*, 2006, **177**, 1687–1690.

[540] X. Xia, R. Oldman and R. Catlow, *Chem. Mater.*, 2009, **21**, 3576–3585.

[541] S. Madhual, K. Pramanik and P. P. Kumar, *Phys. Chem. Chem. Phys.*, 2022, **24**, 18281–18290.

[542] Y. Wang, F. Zahid, J. Wang and H. Guo, *Phys. Rev. B*, 2012, **85**, 224110.

List of Publications

1. **Sudeshna Madhual**, Krishnanjan Pramanik and P. Padma Kumar, *"Understanding Oxide Ion Transport In Yttria Stabilized Zirconia: Fresh Insights from Molecular Dynamics Simulations"*, Phys. Chem. Chem. Phys., **24**, 18281-18290 (2022).

2. **Sudeshna Madhual** and P. Padma Kumar, *"Insights on Oxide Ion Transport In Yttria Doped Ceria from Molecular Dynamics Simulation"*, J. Mater. Sci., **58**, 4499-4512 (2023).

3. **Sudeshna Madhual** and P. Padma Kumar, *"Understanding Oxide Ion Transport In Cationic Ordered Yttria Stabilized Zirconia"*, (To be submitted).

Schools/Workshops/Conferences attended

1. Attended *"THE INTERNATIONAL CONFERENCE ON BEYOND FOSSIL FUELS: The Future of Alternative Energy Technologies"*July 2022, Department of Ceramic Engineering IIT (BHU), Varanasi, India. [Oral presentation]
2. Attended *"Research and Industrial Conclave-Integration'23"* Indian Institute of Technology Guwahati, Guwahati, Assam. [Oral presentation]
3. Attended *"Materials Today Conference 2023"* by Elsevier in association with the Materials Today journals, Singapore Expo, Singapore. [Poster presentation]